To the Graduate Council:

I am submitting herewith a thesis written by Helen Marie Herring entitled "Damage Assessment of a Swirl Glass Mat Reinforced Polyurethane Composite Using Nondestructive Test Methods." I have examined the final copy of this thesis for form and content and recommend that it be accepted in partial fulfillment of the requirements for the degree of Master of Science, with a major in Polymer Engineering.

R.S. Benson, Major Professor

We have read this thesis
and recommend its acceptance:

Accepted for the Council:

Associate Vice Chancellor and
Dean of The Graduate School

DAMAGE ASSESSMENT OF A SWIRL GLASS MAT REINFORCED POLYURETHANE COMPOSITE USING NONDESTRUCTIVE TEST METHODS

A Thesis

Presented for the

Master of Science

Degree

The University of Tennessee, Knoxville

Helen Marie Herring

December 1997

To my parents,

Harvey W. and Elaine O. Herring

and to my brother,

Gary W. Herring

Because you believed in me, with love and thanks...

ACKNOWLEDGMENTS

I would like to express my appreciation to Dr. Roberto S. Benson for his encouragement and guidance during my time at the University of Tennessee. I would also like to express my gratitude to the other members of my committee, Dr. Peter K. Liaw and Dr. Randall R. Bresee, for their help. To Drs. David and Carolyn Joy for their excellent instruction and guidance in the methods of scanning electron microscopy, I would like to express my appreciation. Special gratitude is extended to Dr. James M. Corum and the Structural Mechanics Group at Oak Ridge National Laboratory, Rick L. Battiste, Dr. William A. Simpson, Dr. Herb E. McCoy, and Dr. Marina B. Ruggles for their support on this project. And, special thanks goes to Mr. Darnell C. Worley II for all his help and support and for answering all my many questions.

For their continuous technical assistance and support, I would like to thank the dedicated staff of the electronic and machine shops, Ms. Aileen Cagle, Mr. Frank Holloway, and Mr. Randy Stooksbury. I would also like to thank Ms. Sandy Maples and Ms. Carla Lawrence for always being there to lend a helping hand. Thanks are also due to my fellow graduate students for all their help.

To my family and friends for their love and support throughout my graduate experience, I would never have reached my goal without you.

This research was sponsored by Oak Ridge National Laboratory as part of the Department of Energy's Durability of Lightweight Composite Structures Project.

ABSTRACT

Continuous swirl glass mat (CSM) reinforced polyurethane composite samples were fatigue and creep tested either in a standard environment of air with 50% relative humidity or while immersed in distilled water or windshield washer fluid. Pre- and post-test samples were examined nondestructively, using C-scan ultrasonics and light-transmission microscopy (LTM). Additionally, selected samples that failed during the tests were further examined by scanning electron microscopy (SEM) to evaluate the extent of damage in the vicinity of the fracture surface. The pre- and post-test C-scan ultrasonic and LTM images were compared and analyzed to determine changes in the CSM composite, attributed to damage. Combining these analyses with SEM results, correlations were made between environmental exposure and changes in the creep and fatigue properties of the material. Changes in the mechanical properties corresponded to changes observed from the analyses and comparison of the nondestructive evaluation results.

It was found that exposure to distilled water and windshield washer fluid caused a decrease in the stiffness and in the fatigue life of the material. In the case of the windshield washer fluid, this decrease was discerned to be the result of plasticization of the matrix. The distilled water was found to have a more detrimental effect on the glass fiber reinforcement, attacking at the fiber/matrix interface. The plasticization of the CSM composite as a result of environmental exposure was considered a probability as the solubility parameters of the environments and the polyurethane matrix are of similar values.

TABLE OF CONTENTS

Chapter		Page
I.	Introduction	1
II.	Background	4
	2.1. Glass Fiber Reinforced Composites	4
	2.1.1. Continuous Swirl Mat Composites	7
	2.1.2. Damage Associated with Composites	8
	2.2. Influence of Environments	14
	2.2.1. Physically Active Environments	14
	2.2.2. Chemically Active Environments	15
	2.3. Methods of Nondestructive Evaluation	15
	2.3.1. C-Scan Ultrasonics	16
	2.3.2. Light-Transmission Microscopy	19
	2.3.3. Scanning Electron Microscopy	19
III.	Experimental	22
	3.1. Materials	22
	3.2. Environments	25
	3.3. Instrumentation	25
	3.4. Testing	29
IV.	Results	32
	4.1. Mechanical Properties	32
	4.1.1. Creep	32
	4.1.2. Fatigue	32

4.2. Damage Assessment 35
4.2.1. Creep 35
4.2.1.1. C-Scan Ultrasonics 35
4.2.1.2. Light-Transmission Microscopy 40
4.2.1.3. Scanning Electron Microscopy 45
4.2.2. Fatigue 48
4.2.2.1. C-Scan Ultrasonics 51
4.2.2.2. Light-Transmission Microscopy 57
4.2.2.3. Scanning Electron Microscopy 57
V. Discussion 70
5.1. Mechanical Properties 70
5.1.1. Creep 73
5.1.2. Fatigue 74
5.2. Damage Assessment 75
5.2.1. Creep 75
5.2.1.1. C-Scan Ultrasonics 75
5.2.1.2. Light-Transmission Microscopy 84
5.2.1.3. Scanning Electron Microscopy 92
5.2.2. Fatigue 93
5.2.2.1. C-Scan Ultrasonics 93
5.2.2.2. Light-Transmission Microscopy 100
5.2.2.3. Scanning Electron Microscopy 102
VI. Conclusions 111
VII. Recommendations 114
List of References 115

Appendix 120

A-1. Creep C-Scan Ultrasonic Data 121

A-2. Fatigue C-Scan Ultrasonic Data 129

A-3. Creep LTM Data 138

A-4. Fatigue LTM Data 146

Vita 155

LIST OF FIGURES

Figure		Page
2-1.	Three Types of Fiber Orientation Used in Composite Reinforcement	6
2-2.	Schematic of Brittle Fracture Bands	9
2-3.	Schematic of Fatigue Crack Propagation	9
2-4.	Glass Fiber Reinforced Polyester Composite, 110x Showing River Pattern	11
2-5.	Cotton Fiber Filled Phenol-Formaldehyde, 1200x Showing Brittle Fracture Bands	11
2-6.	Glass Fiber Reinforced Polyester, 65x Showing Fiber Breakage and Pull-Out	12
2-7.	Glass Fiber Reinforced Polycarbonate, 1050x Showing Fiber/Matrix Debonding and Fiber Pull-Out	12
2-8.	Glass Fiber Reinforced Polycarbonate, 1100x Showing Matrix Degradation and Interfacial Debonding	13
2-9.	Schematic of C-scan Ultrasonic Apparatus	17
3-1.	Flow Chart of Research Plan	23
3-2.	Swirl Glass Mat Reinforcement	24
3-3.	Reference Schematic of Test Specimen Orientation	24
3-4.	Schematic of a CSM Composite Sample Showing Pre-Test Light Imaging Pattern	27

3-5. Schematic of a CSM Composite Sample
Showing Post-Test Light Imaging Pattern 28
4-1. C-Scan Images of P21-0-3 (Air, 50% RH) 36
4-2. C-Scan Images of P21-0-10 (Distilled Water) 37
4-3. C-Scan Images of P21-0-9 (Windshield Washer Fluid) 38
4-4. LTM Image of P21-0-27 (Air, 50% RH)
Pre-Test Image #16 42
4-5. LTM Image of P21-0-27 (Air, 50% RH)
Post-Test Image #16 (No Fracture) 42
4-6. LTM Image of P21-0-22 (Distilled Water)
Pre-Test Image #16 43
4-7. LTM Image of P21-0-22 (Distilled Water)
Post-Test Image #16 (Approx. 2.0 cm From Fracture) 43
4-8. LTM Image of P21-0-7 (Windshield Washer Fluid)
Pre-Test Image #10 44
4-9. LTM Image of P21-0-7 (Windshield Washer Fluid)
Post-Test Image #10 (Approx. 9.0 cm From Fracture) 44
4-10. SEM Image of P21-0-3 (Air, 50% RH) at 20 KeV, 450x
Showing Microcracks, Perpendicular to Load Axis,
on Specimen Side 46
4-11. SEM Image of P21-0-3 (Air, 50% RH) at 20 KeV, 250x
Showing Microcracks, Perpendicular to Load Axis,
on Specimen Side 46
4-12. SEM Image of P21-0-10 (Distilled Water) at 20 KeV, 90x
Showing Several River Patterns 47

4-13. SEM Image of P21-0-10 (Distilled Water) at 20 KeV, 180x Showing River Pattern Originating at Fiber Bundle With Air Voids 47
4-14. SEM Image of P21-0-10 (Distilled Water) at 20 KeV, 200x Showing Brittle Fracture Bands 48
4-15. SEM Image of P21-0-7 (Windshield Washer Fluid) at 20 KeV, 250x Showing Matrix Still Bonded to Fibers 49
4-16. SEM Image of P21-0-7 (Windshield Washer Fluid) at 20 KeV, 250x Showing Voids in Matrix 49
4-17. SEM Image of P21-0-7 (Windshield Washer Fluid) at 20 KeV, 250x Showing Smooth Matrix Surrounding Fiber Bundles 50
4-18. SEM Image of P21-0-7 (Windshield Washer Fluid) at 20 KeV, 200x Showing Smooth Matrix Surrounding Fiber Bundles and Voids ... 50
4-19. C-Scan Images of P21-0-11 (Air, 50% RH) 52
4-20. C-Scan Images of P21-0-26 (Distilled Water) 53
4-21. C-Scan Images of P21-0-18 (Windshield Washer Fluid) 54
4-22. LTM Image of P21-0-11 (Air, 50% RH) Pre-Test Image #16 58
4-23. LTM Image of P21-0-11 (Air, 50% RH) Post-Test Image #16 (Approx. 0.6 cm From Fracture) 58
4-24. LTM Image of P21-0-25 (Distilled Water) Pre-Test Image #8 59
4-25. LTM Image of P21-0-25 (Distilled Water) Post-Test Image #8 (Fracture) 59

4-26. LTM Image of P21-0-18 (Windshield Washer Fluid)
Pre-Test Image #12 60
4-27. LTM Image of P21-0-18 (Windshield Washer Fluid)
Post-Test Image #12 (Approx. 0.2 cm From Fracture) 60
4-28. SEM Image of P21-0-11 (Air, 50% RH) at 20 KeV, 120x
Showing River Patterns Extending From Fiber Bundles 62
4-29. SEM Image of P21-0-11 (Air, 50% RH) at 20 KeV, 200x
Showing River Patterns and Matrix Clinging to Fibers 62
4-30. SEM Image of P21-0-25 (Distilled Water) at 20 KeV, 200x
Showing Brittle Fracture Bands 63
4-31. SEM Image of P21-0-25 (Distilled Water) at 20 KeV, 250x
Showing River Patterns Extending From Area of Fiber
Pull-Out 63
4-32. SEM Image of P1-0-25 (Distilled Water) at 20 KeV, 200x
Showing River Pattern Extending From Fiber Bundles 64
4-33. SEM Image of P21-0-25 (Distilled Water) at 20 KeV, 250x
Showing River Patterns and Clean Fibers 64
4-34. SEM Image of P21-0-17 (Windshield Washer Fluid) at 20 KeV, 500x
Showing Matrix Still Bonded to Fibers 65
4-35. SEM Image of P21-0-17 (Windshield Washer Fluid) at 20 KeV, 250x
Showing Smooth Matrix Area With Void 65
4-36. SEM Image of P21-0-17 (Windshield Washer Fluid) at 20 KeV, 200x
Showing Smooth Matrix Surrounding Fibers and Area of
Debonding 66

4-37. SEM Image of P21-0-17 (Windshield Washer Fluid) at 20 KeV, 250x Showing Smooth Matrix Scattered With Debris 66

4-38. SEM Image of P21-0-25 (Distilled Water) at 1.5 KeV, 70x Showing Propagation of Fracture Along Fiber Bundles 67

4-39. SEM Image of P21-0-25 (Distilled Water) at 1.5 KeV, 70x Showing Propagation of Fracture Along Fiber Bundles 67

4-40. SEM Image of P21-0-25 (Distilled Water) at 1.5 KeV, 200x Showing Crack Propagation at the Edge of the Fracture Surface ... 68

4-41. SEM Image of P21-0-25 (Distilled Water) at 1.5 KeV, 200x Showing Brittle Fracture Bands on the Fracture Surface 69

5-1. Weight Gain per Hour for CSMC Samples Exposed for 11,160 hrs. .. 72

5-2. Weight Loss per Hour for CSMC Samples Exposed for 11,160 hrs. .. 72

5-3. Average Creep Strain, %, per Environment 73

5-4. Average Cycles-to-Failure, N_f, per Environment 75

5-5. C-Scan Mean Graylevel Measurements for Creep Sample P21-0-3 (Air, 50% RH) (No Fracture) 77

5-6. C-Scan % Coefficient of Variation for Creep Sample P21-0-3 (Air, 50% RH) (No Fracture) 78

5-7. C-Scan Mean Graylevel Measurements for Creep Sample P21-0-22 (Distilled Water) (Post-Test Image #4 Taken Near Fracture) 79

5-8. C-Scan % Coefficient of Variation for Creep Sample P21-0-22 (Distilled Water) (Post-Test Image #4 Taken Near Fracture) 80

5-9. C-Scan Mean Graylevel Measurements for Creep Sample P21-0-9 (Windshield Washer Fluid) (Post-Test Image #1 Taken Near Fracture) 81

5-10. C-Scan % Coefficient of Variation for Creep Sample P21-0-9 (Windshield Washer Fluid) (Post-Test Image #1 Taken Near Fracture) 82

5-11. Average Change in Mean Graylevel per Environment for Creep Samples 84

5-12. LTM Mean Graylevel vs. Centerline Position for Creep Sample P21-0-27 (Air, 50% RH) (No Fracture) 86

5-13. LTM % Coefficient of Variation vs. Centerline Position for Creep Sample P21-0-27 (Air, 50% RH) (No Fracture) 87

5-14. LTM Mean Graylevel vs. Centerline Position for Creep Sample P21-0-10 (Distilled Water) (Fractured 10.1 cm From Reference Point) 88

5-15. LTM % Coefficient of Variation vs. Centerline Position for Creep Sample P21-0-10 (Distilled Water) (Fractured 10.1 cm From Reference Point)..... 89

5-16. LTM Mean Graylevel vs. Centerline Position for Creep Sample P21-0-7 (Windshield Washer Fluid) (Fractured 10.8 cm From Reference Point) 90

5-17. LTM % Coefficient of Variation vs. Centerline Position for Creep Sample P21-0-7 (Windshield Washer Fluid) (Fractured 10.8 cm From Reference Point) 91

5-18. C-Scan Mean Graylevel Measurements for
Fatigue Sample P21-0-11 (Air, 50% RH)
(Post-Test Image #5 Taken Near Fracture) 94
5-19. C-Scan % Coefficient of Variation for
Fatigue Sample P21-0-11 (Air, 50% RH)
(Post-Test Image #5 Taken Near Fracture) 95
5-20. C-Scan Mean Graylevel Measurements for
Fatigue Sample P21-0-19 (Distilled Water)
(Post-Test Image #5 Taken Near Fracture) 96
5-21. C-Scan % Coefficient of Variation for
Fatigue Sample P21-0-19 (Distilled Water)
(Post-Test Image #5 Taken Near Fracture) 97
5-22. C-Scan Mean Graylevel Measurements for
Fatigue Sample P21-0-18 (Windshield Washer Fluid)
(Post-Test Image #6 Taken Near Fracture) 98
5-23. C-Scan % Coefficient of Variation for
Fatigue Sample P21-0-18 (Windshield Washer Fluid)
(Post-Test Image #6 Taken Near Fracture) 99
5-24. Average Change in Mean Graylevel
per Environment for Fatigue Samples 101
5-25. LTM Mean Graylevel vs. Centerline Position
for Fatigue Sample P21-0-11 (Air, 50% RH)
(Fractured 3.6 cm From Reference Point) 103

5-26. LTM % Coefficient of Variation vs. Centerline Position for Fatigue Sample P21-0-11 (Air, 50% RH) (Fractured 3.6 cm From Reference Point) 104

5-27. LTM Mean Graylevel vs. Centerline Position for Fatigue Sample P21-0-26 (Distilled Water) (Fractured 4.2 cm From Reference Point) 105

5-28. LTM % Coefficient of Variation vs. Centerline Position for Fatigue Sample P21-0-26 (Distilled Water) (Fractured 4.2 cm From Reference Point) 106

5-29. LTM Mean Graylevel vs. Centerline Position for Fatigue Sample P21-0-17 (Windshield Washer Fluid) (Fractured 1.7 cm From Reference Point) 107

5-30. LTM % Coefficient of Variation vs. Centerline Position for Fatigue Sample P21-0-17 (Windshield Washer Fluid) (Fractured 1.7 cm From Reference Point) 108

5-31. Schematic of Proposed Mechanism of Failure for the CSM Composite 110

LIST OF TABLES

Table		Page
3-1.	Summary of Mechanical Properties for Selected Samples of Plaque P21	30
3-2.	Conditions for CSM Composite Mechanical Tests	31
4-1.	Mechanical Data for Creep Samples	33
4-2.	Mechanical Data for Fatigue Samples	34
4-3.	Mean Graylevel (MG) Measurements for Entire Pre- and Post-Test Creep Sample C-Scans	39
4-4.	Coefficient of Variation (%) in Mean Graylevel for Entire Pre- and Post-Test Creep Sample C-Scans	41
4-5.	Mean Graylevel (MG) Measurements for Entire Pre- and Post-Test Fatigue Sample C-Scans	55
4-6.	Coefficient of Variation (%) in Mean Graylevel for Entire Pre- and Post-Test Fatigue Sample C-Scans	56
5-1.	Solubility Parameters for Polyurethane and Some Common Liquids	71
A-1.	C-Scan Data for P21-0-3 (Air, 50% RH)	121
A-2.	C-Scan Data for P21-0-27 (Air, 50% RH)	122
A-3.	C-Scan Data for P21-0-5 (Distilled Water)	123
A-4.	C-Scan Data for P21-0-10 (Distilled Water)	124
A-5.	C-Scan Data for P21-0-22 (Distilled Water)	125
A-6.	C-Scan Data for P21-0-7 (Windshield Washer Fluid)	126

A-7. C-Scan Data for P21-0-8 (Windshield Washer Fluid) 127
A-8. C-Scan Data for P21-0-9 (Windshield Washer Fluid) 128
A-9. C-Scan Data for P21-0-11 (Air, 50% RH) 129
A-10. C-Scan Data for P21-0-12 (Air, 50% RH) 130
A-11. C-Scan Data for P21-0-21 (Air, 50% RH) 131
A-12. C-Scan Data for P21-0-19 (Distilled Water) 132
A-13. C-Scan Data for P21-0-25 (Distilled Water) 133
A-14. C-Scan Data for P21-0-26 (Distilled Water) 134
A-15. C-Scan Data for P21-0-16 (Windshield Washer Fluid) 135
A-16. C-Scan Data for P21-0-17 (Windshield Washer Fluid) 136
A-17. C-Scan Data for P21-0-18 (Windshield Washer Fluid) 137
A-18. LTM Data for P21-0-3 (Air, 50% RH) 138
A-19. LTM Data for P21-0-27 (Air, 50% RH) 139
A-20. LTM Data for P21-0-5 (Distilled Water) 140
A-21. LTM Data for P21-0-10 (Distilled Water) 141
A-22. LTM Data for P21-0-22 (Distilled Water) 142
A-23. LTM Data for P21-0-7 (Windshield Washer Fluid) 143
A-24. LTM Data for P21-0-8 (Windshield Washer Fluid) 144
A-25. LTM Data for P21-0-9 (Windshield Washer Fluid) 145
A-26. LTM Data for P21-0-11 (Air, 50% RH) 146
A-27. LTM Data for P21-0-12 (Air, 50% RH) 147
A-28. LTM Data for P21-0-21 (Air, 50% RH) 148
A-29. LTM Data for P21-0-19 (Distilled Water) 149
A-30. LTM Data for P21-0-25 (Distilled Water) 150
A-31. LTM Data for P21-0-26 (Distilled Water) 151

A-32. LTM Data for P21-0-16 (Windshield Washer Fluid) 152

A-33. LTM Data for P21-0-17 (Windshield Washer Fluid) 153

A-34. LTM Data for P21-0-18 (Windshield Washer Fluid) 154

I. INTRODUCTION

Glass fiber reinforced polyurethanes already have an established place among composite materials used for automobile applications, including front bumpers and exterior body panels. The automobile industry has employed these composites because of their desirable processing qualities and physical properties. Mechanical properties, as well, have been greatly enhanced with the addition of the glass fiber reinforcements which also increase the ease of processing already valued in polyurethanes.(1,2,3) Generally, these reinforcements have been short fibers, but recently the development of swirl glass mats has expanded the field of reinforced composites and the mechanical properties that can be attained.

By definition, swirl glass mat reinforced composites are randomly dispersed continuous glass fibers in a polymer matrix. The objective of the swirl mat reinforcement is to improve the isotropic loading behavior of the composite material.(4) The advantages of these composites includes a reduction in manufacturing time and cost over laminates by means of the Reaction Injection Molding (RIM) process. The automotive industry's use of the reinforced RIM (RRIM) process ensures that the demand to produce composite structures at low cost and high volume will be satisfied.(5) Swirl glass mats are now being incorporated to increase the overall strength of the polyurethane matrix and generally improve the mechanical properties of the composite for such applications as primary automobile structural members. Additionally, these swirl mat polyurethanes are being tested under conditions that the average automobile structural member might see in its expected lifespan to demonstrate durability and different modes of failure.

The durability of the continuous swirl mat (CSM) composite material is of the

utmost importance to the automotive industry. The conditions under which the swirl glass mat composites are tested to failure are just as important as the test methods and can have an influence on the damage sustained. Such conditions that would degrade the in-service performance of the CSM composite generally involve cyclic loadings, sustained loadings, low-energy impacts, and environmental exposure. The Department of Energy (DOE) has established the Durability of Lightweight Composite Structures for Automotive Applications Project at Oak Ridge National Laboratory (ORNL) to provide the automotive industry with the needed information on the durability of the CSM composite.(5) The research described herein is a part of this project, allocated to the Damage Assessment Group, Department of Materials Science and Engineering, at the University of Tennessee, Knoxville.

The objective of this work is to postulate, demonstrate, and verify the damage sustained by the CSM composite material during creep and fatigue loading while exposed to two distinct environments. Some of the more harsh environments that would affect the performance of these composites are distilled water and methanol-based windshield washer fluids. From prolonged exposure to these fluids, the swirl mat polyurethanes may undergo some changes at the surface and the bulk, possibly facilitating failure during mechanical loading. Indeed, organic environments have been shown to increase the failure of polymer materials by aiding crack propagation.(6, 7) Equally important is the choice of nondestructive test methods to determine the damage in the CSM composite, whether mechanical, environmental, or both.

To facilitate this research, the characteristics of glass fiber reinforced composites with special attention paid to CSM composites, the nature of damage, and the influence of environments are described in detail. The nondestructive test methods employed for this

study, C-scan ultrasonics, light-transmission microscopy (LTM), and scanning electron microscopy (SEM), are also explained. Descriptions of the materials, specific environments, instrumentation, test apparatus and conditions comprise the experimental section. The results of the creep and fatigue tests in the chosen environments are then presented and discussed, in separate categories of mechanical properties and damage assessment.

II. BACKGROUND

2.1. Glass Fiber Reinforced Composites:

In the continuing effort to achieve lighter weight while maintaining high strength in composites, one of the foremost composite types is that of inorganic fiber reinforcement in an organic matrix, commonly glass fibers in a polymer matrix. There are four basic principles to consider when using such a composite formulation. They are glass fiber content and arrangement, resin, manufacturing process, and performance and cost. The first two principles influence the physical properties of the composite, whereas the last two principles are themselves influenced by the selection of materials, design, and processes to be used in the fabrication of the composite.(8)

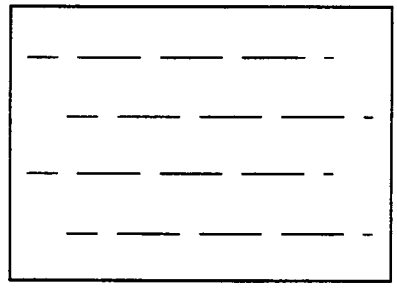
The amount of glass fiber and its arrangement combine to affect the mechanical properties of the composite. It is known that as the amount of glass fiber in a composite increases by volume, the tensile strength of the composite increases as well. Tensile strength will also be influenced by how the fibers are arranged in the composite. If all the fibers are placed parallel to each other, tensile strength and modulus are greatest in the direction of the filaments. If half the fibers are arranged perpendicular to the other half, then the tensile strength is now highest in each direction of the fiber orientation. In this case, however, the tensile strength is considered less than for a unidirectional orientation. If the fibers take on a three-dimensional, or random, arrangement, then the tensile strength and modulus of the composite is now isotropic. The composite with such a random fiber orientation is reinforced in the three dimensions, but the reinforcement value is only a third of that for the unidirectional orientation. In other words, the mechanical properties in any direction decrease as the fiber orientation becomes more random. In the case of an

isotropic composite (i.e., three-dimensional fiber orientation), the strength and stiffness in any direction must be in excess of the largest requirement the material must endure in application. Figure 2-1 illustrates the three types of fiber orientation used as composite reinforcement.(8)

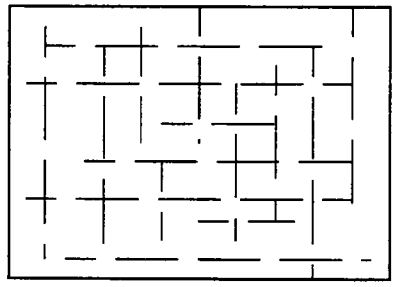
The matrix serves two distinct purposes: (a) locking the fiber reinforcement in place and (b) deforming and transmitting applied stresses to the reinforcement. For composites used in structural applications, the matrix material must display a greater elongation at break than the fiber reinforcement and the ability to change shape in such a way as to only place a tensile load on the fibers. The polymer resin, used for the matrix, influences the chemical, electrical, and thermal properties of the composite. The resistance of the composite to aggressive environments and heat are governed by the selection of the appropriate polymer resin.(8)

The manufacturing process varies depending on the selection and amounts of raw materials used to make a composite. The performance requirements of the composite must also be taken into consideration. Different combinations of materials for different applications decrease the choice of processes. Ultimately, though, economics dictate what materials and processes are used. Judicious selection of materials and processes and adoption of efficient design criteria will ensure that economic and performance requirements are met.

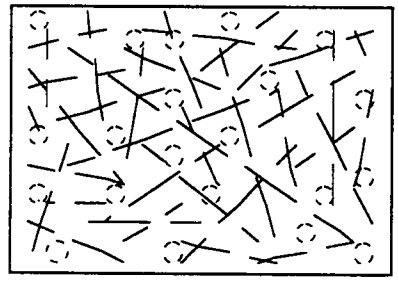
The capacity of the fiber reinforcement and the matrix to redistribute stresses through complimentary interaction enables a composite to endure higher loads than its individual components. However, the composite can only perform this important function if fiber reinforcement and matrix are effectively bonded at the interface. For some composites, this bonding may be achieved simply through contact of the matrix and the fibers, but other composites require coupling agents to create the most effective adhesion



One-Dimensional (Parallel) Orientation



Two-Dimensional (Perpendicular) Orientation



Three-Dimensional (Random) Orientation

Figure 2-1. Three Types of Fiber Orientation Used in Composite Reinforcement (8)

between the two constituents. The coupling agent is usually in the form of a treatment, existing on the fiber surface, that strengthens the interfacial bonding between matrix and reinforcement. Additionally, in the case of glass fibers which are known to degrade when subjected to water, regardless of type, there is the added advantage of protecting the fiber/matrix interface from exposure to moist environments.(8)

With the proper adhesion between fiber and matrix, the interfacial bonding is considered strong and shear-resistant. When a tensile load is applied to the composite, stresses are redistributed to the reinforcement by way of the strong interfacial bonds. The shear strength of the fiber/matrix interfacial bonding limits the strength of the composite, regardless of the individual tensile strengths of the fiber or the matrix. The presence of voids in the matrix or the lack of good interfacial adhesion will severely decrease the efficiency of the reinforcement by impeding proper distribution of the stresses within the composite. Insufficient interfacial bonding will cause instabilities around the fibers, creating the opportunity for discontinuities to form and failure to initiate.

2.1.1. Continuous Swirl Mat Composites:

Continuous swirl glass mat composites consist of glass fibers or fiber bundles in a random orientation in a polymer matrix. There are many reasons for choosing a continuous swirl mat for the reinforcement of a composite, namely the isotropic loading behavior of the resulting material and the ease of molding complicated shapes. The nearly isotropic loading characteristic of the CSM allows it to be used in any number of applications where the stress on the composite may be three-dimensional at any given time. The ability to mold the CSM to more complex parts makes it a more desirable reinforcement where conformability is required.(8) Currently, CSM composites are used to manufacture safety helmets, luggage, electrical parts, machine housings, and especially automotive parts.

Previously, a few independent studies have been performed to determine the mechanical behavior of composites, using CSM reinforcement with Reaction Injection Molded (RIM) thermoplastic matrices, such as polypropylenes and polyamides.(4, 9, 10, 11) In these studies, the focus has largely been on the static and dynamic loading of notched samples, using fracture mechanics. However, some nondestructive test methods, such as acoustic emission and infrared thermography, have been used to observe failure events and damage zone development in these CSM reinforced composites.(4, 12, 13) Recently, new composites, employing the CSM reinforcement, have been developed that incorporate cross-linked polyurethanes and polyureas for specific automobile structural parts, providing desired strength and weight-savings. For the last three years, the Durability of Lightweight Composite Structures for Automotive Applications Project, undertaken at ORNL, has set about to characterize such a CSM composite material. This project has involved the study of the mechanical behavior under tensile, fatigue, creep, and low-energy impact of a swirl E-glass mat reinforced cross-linked polyurethane composite. Additionally, the assessment of sustained damage and the influence of environments has also been thoroughly addressed.(5, 14)

2.1.2. Damage Associated with Composites:

The mechanical damage, associated with composite failures, can be categorized as four mechanisms, usually occurring simultaneously. These are generally described as matrix cracking, fiber breakage, fiber/matrix interfacial debonding, and fiber pull-out. Prolonged exposure to harsh environments can produce its own characteristic damage and/or accelerate one of the known damage mechanisms.

The primary mechanism for matrix damage is cracking and other distortions, such as "river patterns", appearing internally or on the fracture surface. Figures 2-2 and 2-3 are

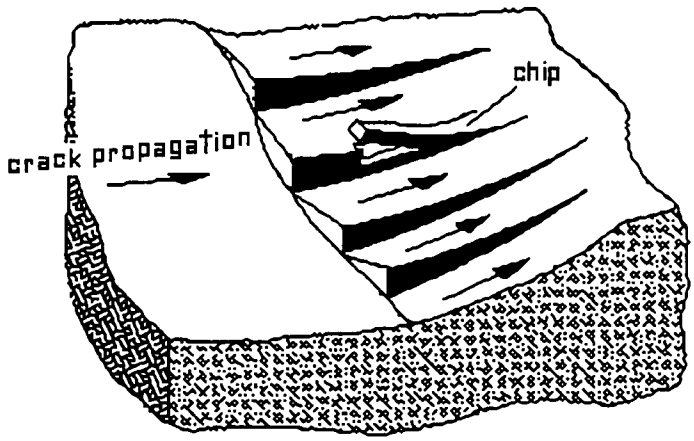


Figure 2-2. Schematic of Brittle Fracture Bands (15)

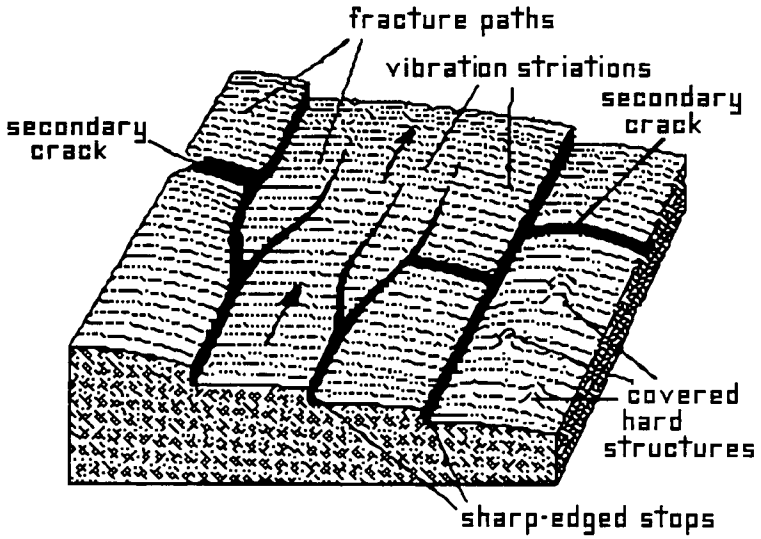


Figure 2-3. Schematic of Fatigue Crack Propagation (15)

schematic representations of polymer fracture surfaces, showing brittle fracture bands and fatigue crack propagation, respectively. Figure 2-4 is an SEM image of a glass fiber reinforced polyester composite, displaying a river pattern as the fan-shaped matrix distortion on the right edge. Figure 2-5 is an SEM image of a cotton fiber filled phenol-formaldehyde sample, showing matrix distortion as step-like formations which are brittle fracture bands. The brittle fracture bands and river patterns can be used to find the origin of the failure. The fracture spreads out from the point of origin much like the spreading open of a fan, hence the fan-like structure of the distortion.

Fiber breakage, evident over an entire fracture surface and possibly internally, is discernible by the distinct snapping of fiber bundles and monofilaments. Fiber/matrix interfacial debonding occurs within the material and on the fracture surface, distinguishable by areas where fiber bundles were apparently lying at a time prior to failure. Fiber/matrix debonding is connected to the last characteristic of damage, fiber pull-out. Pull-out of fibers results when, under mechanical loading, the fiber debonds from the matrix material and breaks. An obvious consequence of fiber debonding, breakage and pull-out is that the composite loses its ability to properly transfer stresses from the matrix to the reinforcement. Therefore, the mechanical properties of the composite, such as strength and stiffness, are greatly reduced, and the material cannot perform the functions for which it was designed. Figure 2-6 is a SEM image of a glass fiber reinforced polyester composite that displays breakage and pull-out of the glass fiber bundles. Figure 2-7 is a SEM image showing the fracture surface of glass fiber reinforced polycarbonate where evidence of fiber/matrix debonding and fiber pull-out can be seen. The arrow in Figure 2-7 indicates the place where a fiber was lying prior to failure but debonded and pulled away from the surface during fracture.

The damage usually associated with exposure to harsh environments can be

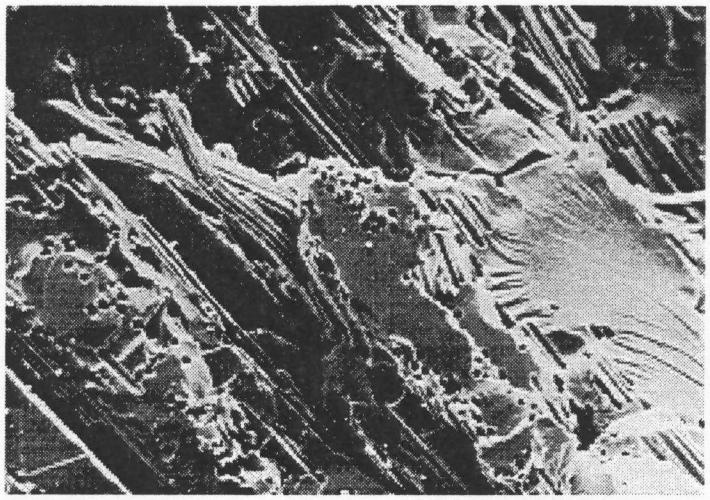


Figure 2-4. Glass Fiber Reinforced Polyester Composite, 110x

Showing River Pattern (15)

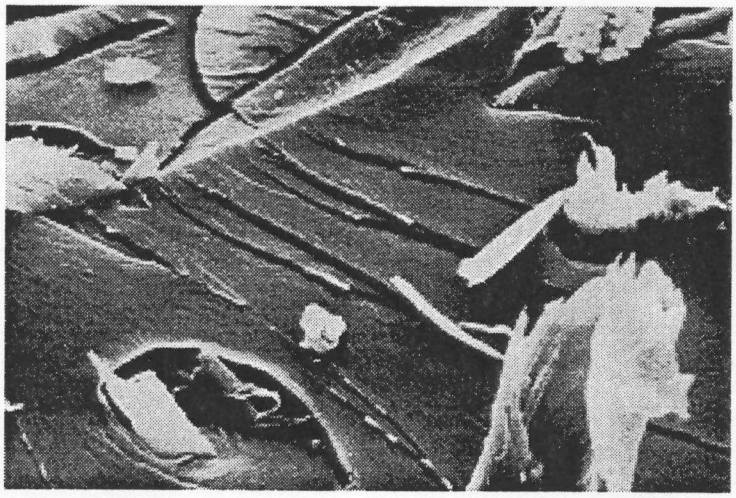


Figure 2-5. Cotton Fiber Filled Phenol-Formaldehyde, 1200x

Showing Brittle Fracture Bands (15)

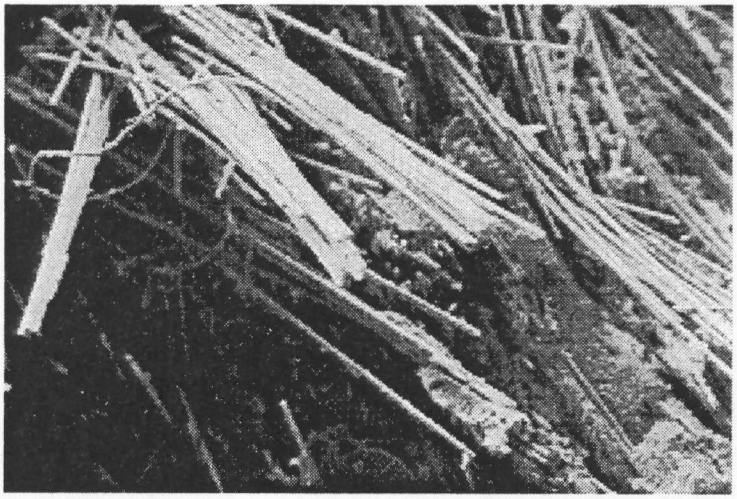


Figure 2-6. Glass Fiber Reinforced Polyester, 65x

Showing Fiber Breakage and Pull-Out (15)

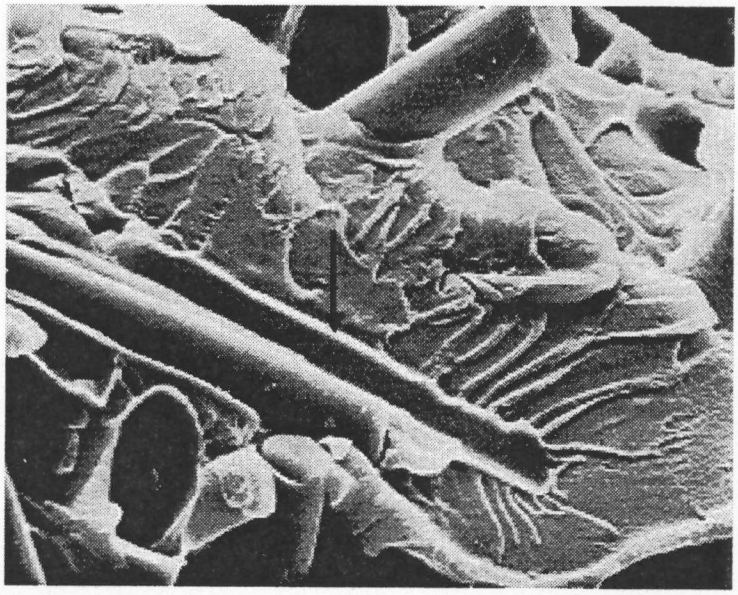


Figure 2-7. Glass Fiber Reinforced Polycarbonate, 1050x

Showing Fiber/Matrix Debonding and Fiber Pull-Out (15)

characterized as degradation of the matrix material, environmental attack on the fiber reinforcement, and a degradation of the fiber/matrix interface. Disruption of the transfer of stresses from the matrix to the fiber reinforcement, similar to that resulting from mechanical damage, can occur as a result of environmental exposure. Hence, environmental damage can also seriously impair the mechanical performance of the composite material. Figure 2-8 is a SEM micrograph of glass fiber reinforced polycarbonate that was exposed to carbon tetrachloride while under stress. The matrix shows some degradation in the form of feathery structures on the matrix fracture surfaces. The fibers appear to be clean on the surface, indicating that they easily debonded from the matrix and pulled out during failure.

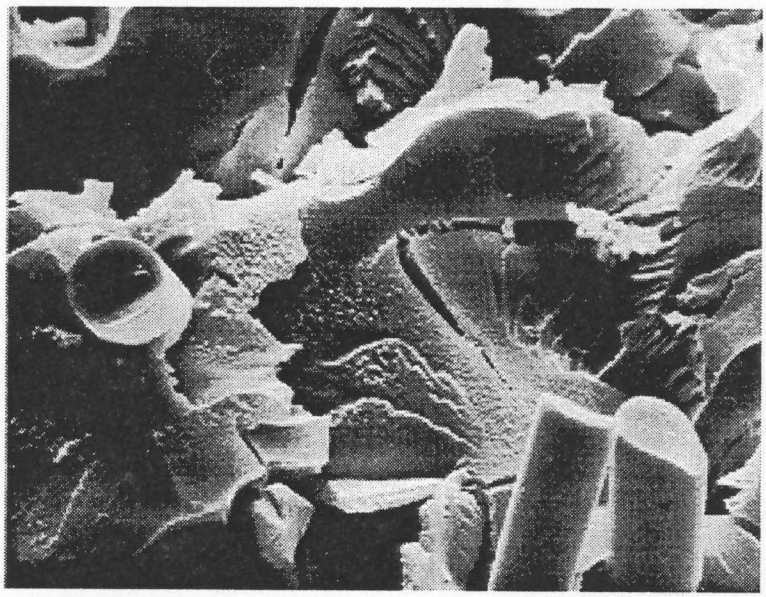


Figure 2-8. Glass Fiber Reinforced Polycarbonate, 1100x
Showing Matrix Degradation and Interfacial Debonding (15)

2.2. Influence of Environments:

Typically, composites for automobile applications are designed to take into account the average ranges of temperature and humidity, experienced on a day-to-day basis. However, it must also be assumed that these materials could just as easily be subjected to more severe environments in the lifetime of use. Because the mechanical properties of a polymer or polymer-based composite dictate the performance of the material in use, the effects on these properties of potentially aggressive enviroments must be understood. The influence of potentially aggressive environments on a polymer material will be determined by their classification as either physically or chemically active.

2.2.1. Physically Active Environments:

Environments that are classified as physically active are those that can be either adsorbed on the surface or can diffuse into the bulk of a material. The adsorption of physically active environments on the surface involves the reduction of the surface free energy at the polymer/environment interface. Any surface defects, such as micropores or microcracks, are filled by the environment. This adsorption effect has been known to cause a reduction in the strength of polymers. Diffusion of a physically active environment into the bulk of a polymer usually results in swelling. This may manifest itself as a more uniform distribution of stress and an increase in the flexibility of the polymer molecules.(16)

For polymers and polymer matrix composites subjected to creep loading in a physically active environment, increasingly accessible areas of the polymer are penetrated and filled by the environment. Subsequently, those areas that are saturated with the environment will undergo deformation. If the same polymer materials are fatigued in the same environment, penetration of accessible areas is dependent on the amount of loading.

At high loads, the rate of crack development in the material is greater than that of surface diffusion of the environment, and therefore, the matrix is not readily diffused by the environment. Conversely, at low loads the rate of crack development is less than the rate of surface diffusion, and the environment will diffuse and usually swell the matrix.(16)

2.2.2. Chemically Active Environments:

Chemically active environments generally cause degradation of the polymer or polymer-based composite which, in turn, results in a reduction in the strength of the material. Experimentally determined reductions in the tensile strength of polymer materials in the presence of chemically active environments have been attributed to the destruction of load-bearing bonds. If the environment is adsorbed on the surface of the polymer only, the reduction in tensile strength is proportional to the change in the cross section at the point of scission. If the environment diffuses into the bulk polymer, then the degradation of the material becomes more random.(16)

The presence of a chemically active environment, during creep loading, will increase the degradation of the polymer because accessible areas, such as microcracks, are allowed to remain open. The effect of chemically active environments on polymer materials that are fatigue loaded is the same as that for the physically active environments, as described above. At low loads, if the rate of surface diffusion is more than the cracks development rate, then the environment will diffuse and degrade the polymer. However, at high loads, the environment will not diffuse into the bulk polymer as the rate of surface diffusion is much lower than that of crack development.(16)

2.3. Methods of Nondestructive Evaluation:

As the application of the CSM composites in the automotive industry increases,

better methods of characterizing damage and failure in the material are being developed to ensure efficient quality control. Nondestructive test methods commonly used to qualify and determine damage in metallic materials are not necessarily useful when dealing with nonmetallics. Therefore, while some methods can be modified, new methods must be developed. Whether microscopic or macroscopic, visual inspection of the composite remains the best technique for detecting surface damage. Internal damage, however, must be found using techniques that transmit energy forms through the composite. The transmission of energy in the form of sound waves to detect internal flaws constitutes the technique known as ultrasonic inspection. For non-opaque materials, the transmitted energy can take the form of light, and imaging of the internal structure and any damage therein can be made. Environmental degradation on the composite surface is discernible using scanning electron microscopy techniques now currently available.

2.3.1. C-Scan Ultrasonics:

To describe ultrasonics physically, the sample is bombarded by an energy form, carried by compression waves in a particular medium. This energy form is ultrasound, inaudible to the human ear due to the high frequency of the waves. In order to determine the wavelength of the ultrasound, the velocity of the propagating wave must be divided by its frequency. This is important for the detection of internal flaws in a particular material because the detection limit for a flaw is on the order of one wavelength. If the wavelength is larger than an internal flaw, that flaw cannot scatter the ultrasonic pulse and therefore, will elude detection. Additionally, ultrasound velocity differs from one material to another. The wavelength of the ultrasonic pulse is longer in those materials which allow faster propagation of the ultrasound.(17)

C-scan ultrasonics is a nondestructive test method that has evolved as a tool for

composite evaluation with the development of increasingly more powerful computers. Specifically, the C-scan method involves the mapping of ultrasonic echoes that are reflected back from a flat or nearly flat sample. Figure 2-9 represents a schematic of a typical C-scan ultrasonic apparatus.(17)

In Figure 2-9, the probe emits the ultrasound waves which propagate through a coupling medium, usually water, in a scanning tank to the specimen. Echo #1 is known as the front-side echo. This is the ultrasound wave reflected from the front surface of the specimen back to the probe in twice the travel time as the initial wave. It has a lesser amplitude due to attenuation of the wave in the coupling medium, wave spreading, and transmittance of some incident sound into the sample. Echo #2 is the back-side echo or that which the back suface reflects toward the probe. This echo arrives later and with lesser

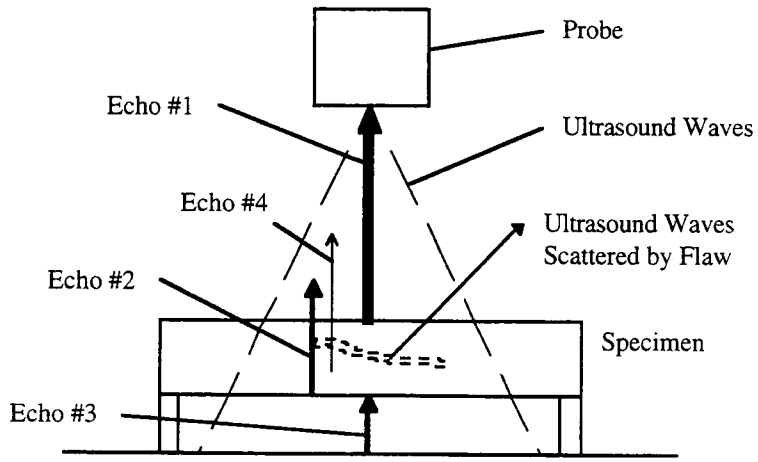


Fig. 2-9. Schematic of C-scan Ultrasonic Apparatus (Fronts of scattered ultrasound waves at equivalent travel times are represented by arrows.) (17)

amplitude than Echo #1 because only some of the wave travels back through the sample and the water before reaching the probe. Some bounces back from the front surface to remain inside the sample, and some of the wave is transmitted completely through the sample. Tank-bottom echo is that which is reflected back from the bottom of the tank after traveling through the couplant and sample twice and is represented by Echo #3. This echo will arrive much later than the first two echoes and be only a fraction of the original ultrasound wave. More of it will remain in the specimen, having encountered the front and back surfaces again on the return path back to the probe.(17)

Should the ultrasound wave encounter any flaws within the sample, the probe may pick up reflections of the wave as Echo #4. This echo will only represent that part of the wave that is reflected from flaws approximately perpendicular to the incident wave. Any flaws or sections of flaws which are not more or less perpendicular to the incident wave will only serve to scatter the wave in directions that will remain undetected. All of the echos detected by the probe make up the pulse echo profile, and there exists such a profile for each sampling point, encountered during scanning of the specimen. In more advanced C-scan ultrasonic systems, there exists the ability to set an arbitrary number of gates after the experiment. This, in turn, allows the generation of arbitrary echo time slices from which the corresponding maximum amplitudes can be obtained. Maps of the amplitudes of echos arriving from various depths within a sample are generated. Assembled three-dimensionally, these maps specify the location and other information about discontinuities, which represent echo-generating interfaces, throughout the sample.(17)

Detection and measurement of flaws depends on their attenuation of the transmitted sound waves. The images gathered, using the C-scan ultrasonic method, are a map of the specimen that displays, usually in grayscale, its internal features. Flaws in the specimen generally appear as dark areas, which represent a greater attenuation of the transmitted

sound waves. By comparing the pre- and post-test C-scan images of a sample, sustained damage will appear as darkening of certain areas in the post-test image.(17)

2.3.2. Light-Transmission Microscopy:

Light-Transmission Microscopy (LTM) is another test method, used on polymer-based composites, of which the nondestructive benefits are currently being realized. This technique is very simple in operation, yet it can reveal many internal details about a material that can have a direct influence over its service life. In LTM, a high intensity light source is placed on one side of a relatively translucent polymer composite sample, such that the light is transmitted directly through the specimen. Lenses of varying magnification and fitted with a camera are situated on the side of the composite sample opposite the transmitted light. From this set-up it is then possible to detect internal features, such as void spaces, fiber orientation, and any defects due to processing or that form as a result of mechanical testing or service.(18) Highly advanced computer systems and specialized acquisition software have been developed that enable the examination of polymer composite samples before and after mechanical testing. A comparison of pre- and post-test images provides for the determination of damage sustained on a subsurface level. Depending on the objective of using this technique, possible limitations of LTM arise mostly in relating image resolution to depth-of-focus. Generally, some image resolution is sacrificed in order to focus deeper into the specimen's interior. This problem can sometimes be alleviated by the utilization of lenses with greater magnifying capability.

2.3.3. Scanning Electron Microscopy:

The use of Scanning Electron Microscopy (SEM) to examine polymer-based

composite materials has certain advantages. At low operating voltages, namely around 1 to 1.5 KeV, polymers and polymer-matrix composites may be viewed without the addition of conductive coatings, which can decrease the amount of detectable surface detail. This is significant when searching for defects or damage on a fractured sample. On the other hand, the lack of a conductive coating on the polymer specimen can lead to the disadvantage of increased charging on the specimen surface. This charging results when there is a build-up on the specimen surface of an excess current that cannot bleed off in the case of a non-conductive sample. If SEM operating conditions are adjusted such that the secondary and backscattered electron emissions balance the incident beam current, then the occurrence of charging is kept to a minimum. There is an incident beam energy at which this condition holds true, known as E_2, which is a function of the electron beam energy, E_0, and the atomic number, Z, of the specimen examined. Since polymers are generally of lower atomic numbers than metallic materials, the E_2 is also lower. Further, charging may then be categorized two ways:

1. If $E_2 < E_0$, then the specimen is experiencing negative charging, characterized by an extremely bright image; there are too many secondary electrons being detected as they are repulsed by the specimen surface.
2. If $E_2 > E_0$, then the specimen is experiencing positive charging, characterized by a very dark image; there are too few secondary electrons being detected as they migrate back to the specimen surface and eventually balance the charge on the surface.(19)

Another effective means of eliminating specimen charging is to operate the SEM in the backscattered electron rather than secondary electron mode. In the backscattered electron mode, the incident beam penetrates the specimen surface more deeply than in the secondary electron mode, and approximately half the incident beam energy is reflected back as backscattered electrons into the same hemisphere as the original beam. A detector specifically designed to impede and collect backscattered electrons is used, and the specimen chamber is purged with a gas, usually nitrogen, during scanning. The incident electrons may ionize the gas molecules after which the positive ions are attracted to the negatively charged specimen surface, neutralizing charging effects. Additionally, as the gas pressure is increased, the incident beam current can be increased to values that would normally be too great for use on non-conductive materials, usually around 20 KeV. This advantage enables the operator to achieve greater resolution while imaging the specimen surface.(20)

III. EXPERIMENTAL

Qualifying the chosen nondestructive test methods for the purpose of damage assessment in the CSM composite was best achieved by a comparison of the pre- and post-test data. The research was structured so as to allow such a comparison. An overview of the research plan is presented by the flow chart shown in Figure 3-1. This flow chart shows how the samples were ultrasonically C-scanned and imaged by LTM both before and after environmental exposure and mechanical testing. The data acquired from these examinations was compared, and SEM data was also evaluated. The creep tests were performed by Dr. H. E. McCoy, the fatigue tests by R. L. Battiste, and the C-scan ultrasonic acquistions by Dr. W. A. Simpson at Oak Ridge National Laboratory (ORNL), and the other evaluations were performed at the University of Tennessee, Knoxville (UTK).

3.1. Materials:

The composite was based on a cross-linked, amorphous polyurethane matrix, and the mat was continuous E-glass fiber bundles in a swirl formation. The specific resin and reinforcement used were DOW MM 364 and Certainteed/Vetrotex Unifilo U750, respectively. Figure 3-2 is an image of the swirl glass mat used as the reinforcement of this particular composite. The 63.5 cm x 63.5 cm x 0.32 cm-thick (25 in x 25 in x 0.125 in) flat panels were produced by structural reaction injection molding (SRIM), and all samples, used in this study, were cut from the same panel, designated as plaque P21. Figure 3-3 shows a schematic of the test sample as used in all examinations.

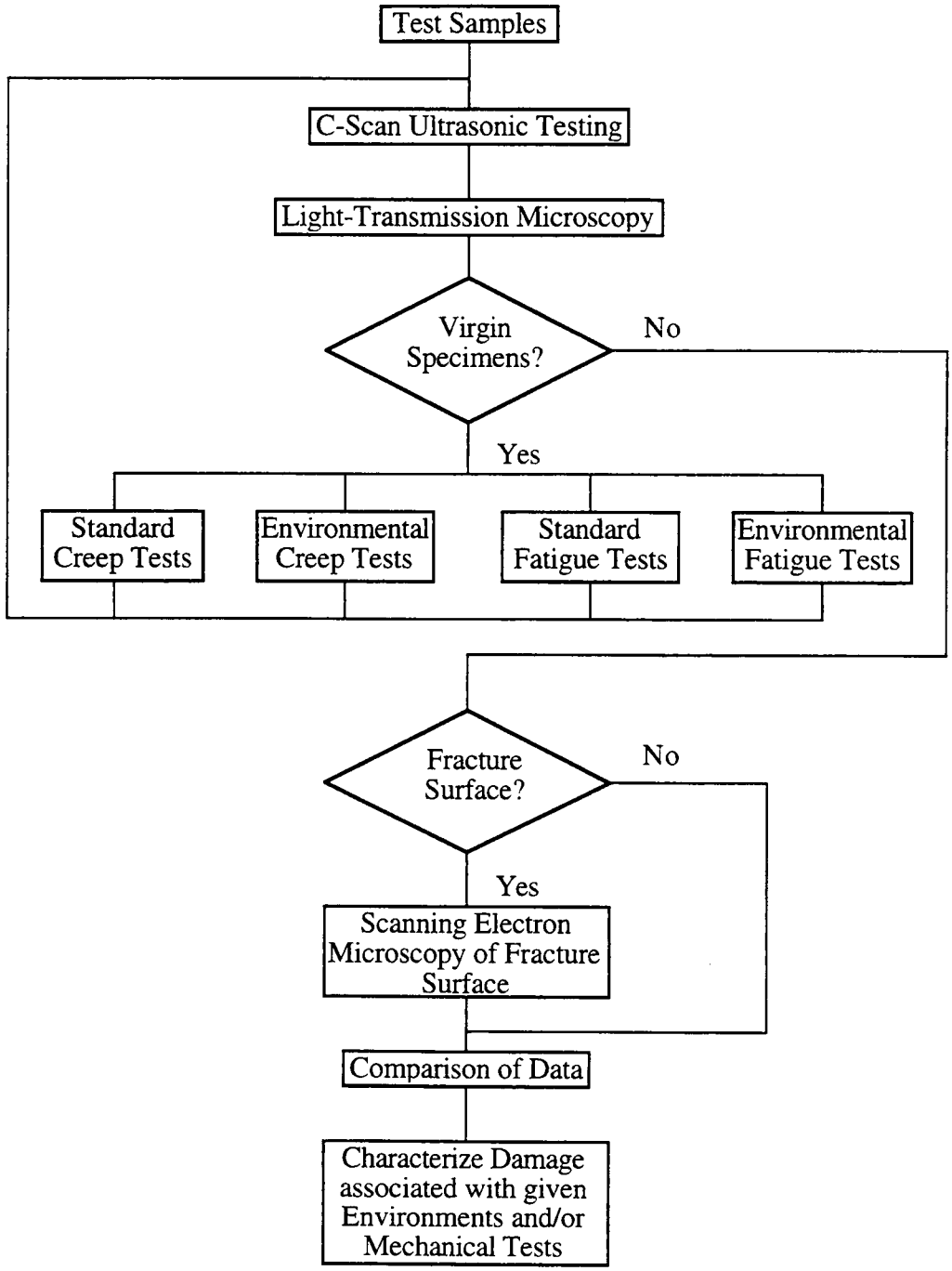


Figure 3-1. Flow Chart of Research Plan

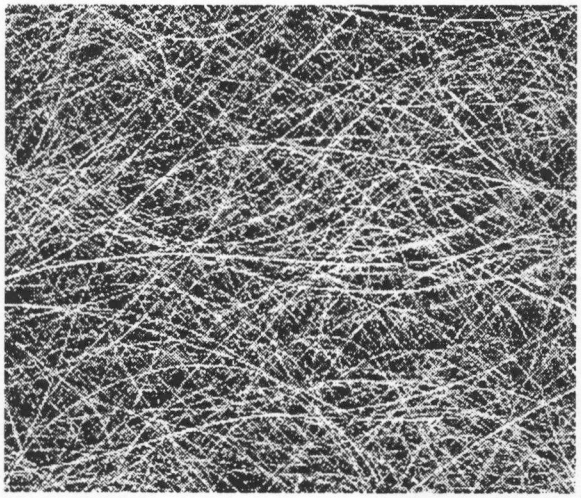


Figure 3-2. Swirl Glass Mat Reinforcement

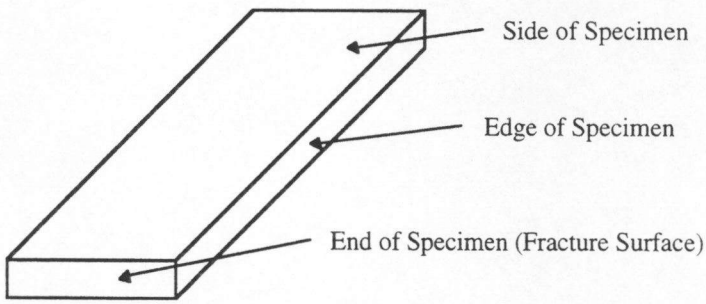


Fig. 3-3. Reference Schematic of Test Specimen Orientation

3.2. Environments:

The samples were divided into two groups, one group to be exposed to specific environments and one group to be tested in air and 50% relative humidity to serve as standards. The environments chosen for this research were distilled water and windshield washer fluid (~90% methanol). Specimens were exposed to either the distilled water or the windshield washer fluid and then mechanically tested. Samples, designated for environmental fatigue tests, were presaturated in the fluids for 100 hours prior to testing and then tested while in the chosen environments. Samples, intended for environmental creep tests, were tested in the chosen environments without presaturation. Since creep tests generally involve a greater amount of time, presaturation was considered unnecessary.

3.3. Instrumentation:

The ultrasonic C-scans were obtained using a Sonix FlexScan-C system with a Panametrics scanning tank, modified to work with the Sonix apparatus. The ultrasonic pulser/receiver was a Panametrics 5052P/R, and the digitizer was a Sonix STR*8100, a real-time 100 MHz, 8-bit flash converter. On repetitive waveforms, the digitizer can be used at rates as high as 3200 MHz. The C-scans, used for this research were acquired with the digitizer set at 200 MHz. All C-scans were collected on a Dell 310 computer, using Sonix C-SCAN™ acquisition and C-VUE™ image display softwares.(21) Subsequent mean graylevel measurement of the C-scan images was performed using Adobe Photoshop™ imaging software.

The apparatus used for acquiring LTM images consisted of a Bausch & Lomb optical microscope, fitted with an Olympus objective lens and a Pulnix 9700 CCD camera.

This camera provides 640 x 480 pixel spatial resolution and 8 bit (256 graylevels) graylevel resolution. Illumination was provided by an Olympus objective microscope light source. The acquisition software, WebPro version 2.1 (©1991-96 X. C. Huang, R. R. Bresee, and Z. Yan), was developed at the University of Tennessee as imaging software to characterize web structures.(18) Of the many advantages of WebPro 2.1, the ability to provide information about bright and dark areas as possible defects was the most important for this research.

All LTM images were taken on the side of the specimens at approximately the mid-point of the gage length. To ensure that failure would occur somewhere in the imaged region during the fatigue tests, the gage length was milled into an hourglass shape prior to mechanical testing. This was not done for the creep samples, however. For the pre-test specimens, a series of 18 light images with a 1.5 x 2.1 mm field-of-view along the 3.4 cm (1.34 in) center line were collected as follows:

1. A point of reference was established on each sample where the tab and gage area met on the opposite end but same side as the sample identification numbers.
2. After an initial light image was made at the reference point, the sample was moved approximately 0.2 cm (0.08 in), traveling away from the tab along the sample's center line. The next light image was then taken and so on in this fashion.
3. 18 light images were made for each sample, covering a center-line length of approximately 3.4 cm (1.34 in). (Please see Figure 3-4)

All previously marked areas were examined on the post-test samples by light microscopy as described above, but images were taken only at intervals. In this case, an

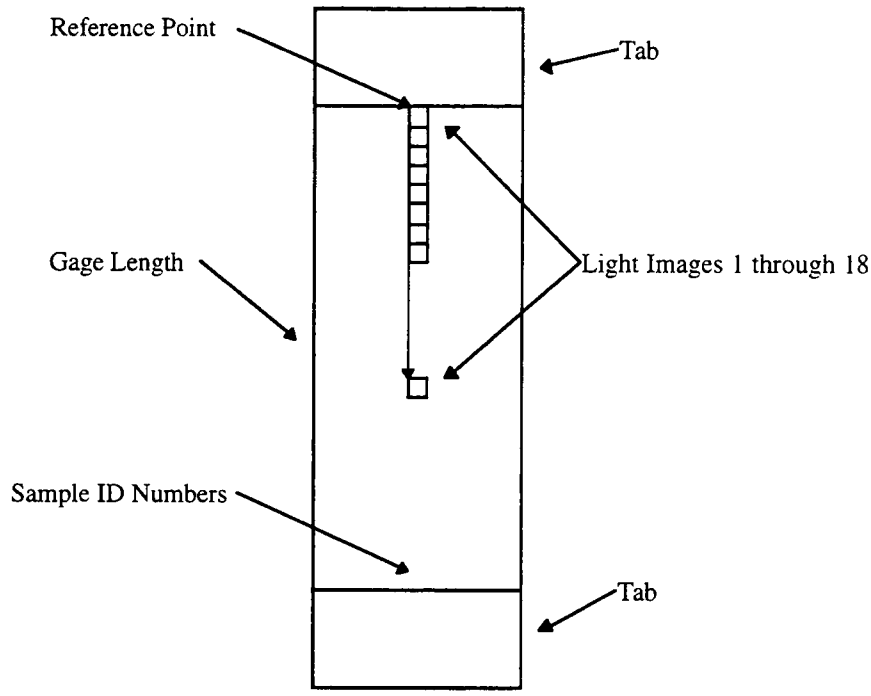


Figure 3-4. Schematic of a CSM Composite Sample Showing Pre-Test Light Imaging Pattern

image was made at the original reference point, then every third image was taken until the fracture surface (if the sample failed) was reached. If the sample fractured, an image of the fracture was taken as was that of the area just preceding the fracture. These post-test images were then compared to the corresponding pre-test images. Figure 3-5 represents the light imaging pattern for the post-test samples. Mean graylevel measurements of the LTM images were performed using Adobe Photoshop™ imaging software in the same fashion as for the C-scan images.

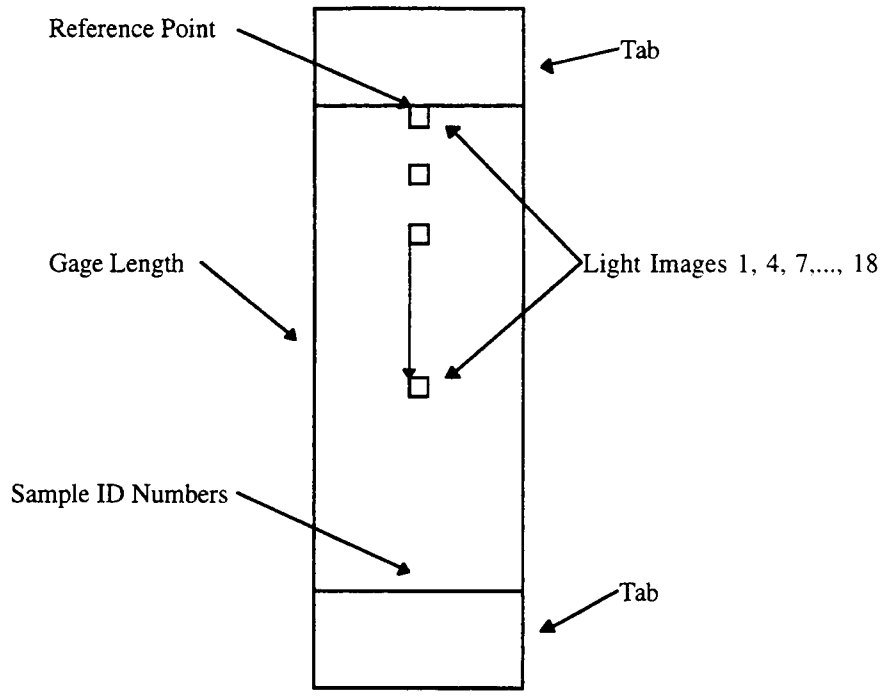


Figure 3-5. Schematic of a CSM Composite Sample

Showing Post-Test Light Imaging Pattern

The samples, designated for fatigue, were tested using special servo-controlled fatigue testing machines. These machines have a maximum load and cyclic frequency of 44.5 kN (10kips) and 10 Hz, respectively. The test machines were equipped with MTS 407 digital controllers to be used for these tests. The specimens, selected for creep, were tested using creep test machines that were lever-armed to create a mechanical advantage of 12 to 1. The creep tests were performed under a 8.9 kN (2000 lb) force. To achieve environmental exposure while mechanically testing the samples, the testing machines were outfitted with pipe chambers made from polyvinyl chloride (PVC). This enabled the specimens to be tested while completely saturated by fluid.(21, 22)

SEM examination was employed to document mechanical damage and the existence of any particular trends, regarding occurrence, that could be attributed to environmental damage. The fractured specimens were examined, using a Hitachi S-3200N scanning electron microscope at beam energies of 1.5 to 1.7 KeV in the secondary electron mode or 20 KeV with a compressed gas purge in the backscatter mode.

3.4. Testing:

Selected samples were taken from plaque P21 for mechanical characterization under tensile load at ORNL by Dr. M. B. Ruggles.(14) The stiffness, ultimate tensile strength (UTS), and failure strain for the selected samples and their respective averages are summarized in Table 3-1.

Prior to environmental exposure and mechanical testing, the virgin specimens were ultrasonically C-scanned and examined by LTM. They were then either fatigue or creep tested with or without environmental exposure, in most cases to failure. Afterwards, they were again C-scanned, LTM imaged and further examined by SEM for damage. Table 3-2 is a summary of the conditions under which the mechanical tests were performed. The fatigue tests were tension fatigue with R = 0.1.

Table 3-1. Summary of Mechanical Properties

for Selected Samples of Plaque P21 (14)

	Specimen No.	Stiffness, Msi	UTS, ksi	Failure Strain, %
	P21-0-49	1.424	24.42	2.42
	P21-0-50	1.431	21.95	2.13
	P21-0-51	1.459	24.15	2.38
	P21-0-52	1.421	24.19	2.47
	P21-0-53	1.432	22.33	2.19
	P21-0-54	1.465	24.79	2.29
	P21-0-55	1.378	25.40	2.50
	P21-0-56	1.377	22.31	2.06
Average		1.424	23.69	2.31
Standard Deviation		0.032	1.31	0.16

Table 3-2. Conditions for CSM Composite Mechanical Tests

Test	Environment	Load
Standard Creep	Air, 50% Relative Humidity	65% UTS
Environmental Creep	Distilled Water	65% UTS
Environmental Creep	Windshield Washer Fluid	65% UTS
Standard Fatigue	Air, 50% Relative Humidity	40% UTS
Environmental Fatigue	Distilled Water	40% UTS
Environmental Fatigue	Windshield Washer Fluid	40% UTS

IV. RESULTS

4.1. Mechanical Properties:

4.1.1. Creep:

The specimens, chosen for creep, were tested at ORNL using lever-armed creep test machines. Special PVC pipes were used to encase those samples that were tested in liquid environments. The mechanical data gathered from the creep samples appears in Table 4-1. Particular attention was paid to the effect of the specific environments on creep strain. Except for an ambiguous creep strain value for windshield washer fluid sample, P21-0-8, the majority of the creep strains were relatively similar within their respective environments. Average creep strains for both the distilled water and the windshield washer fluid specimens were slightly higher than that of the air, 50% relative humidity samples. It is important to note that the samples that were tested in air, 50% relative humidity were discontinued at the times specified under Rupture Life, due to time constraints.

4.1.2. Fatigue:

The fatigue samples were tested at ORNL in servo-controlled fatigue testing machines. These machines were outfitted with special canisters for the purpose of testing samples in their respective liquid environments. Table 4-2 represents the mechanical data for all fatigue tested samples. The effect of the specific environments on the fatigue life, given by the cycles-to-failure for each sample, showed interesting trends. The average cycles-to-failure for the both the distilled water and windshield washer fluid samples were significantly lower than that of the air, 50% relative humidity samples.

Table 4-1. Mechanical Data for Creep Samples

Specimen No.	Test Environ.	Stress, ksi	Rupture Life, hrs	Creep Strain, %
P21-0-3	Air, 50% RH	15.187	502D	0.13
P21-0-27	Air, 50% RH	15.187	739D	0.25
P21-0-5	D. Water	15.187	320	0.36
P21-0-10	D. Water	15.187	46	0.31
P21-0-22	D. Water	15.187	133	0.29
P21-0-7	W. W. Fluid	15.187	724	0.34
P21-0-8	W. W. Fluid	15.187	367	0.99
P21-0-9	W. W. Fluid	15.187	263	0.33

Table 4-2. Mechanical Data for Fatigue Samples

Specimen No.	Test Environ.	Stress, ksi	Cycles to Failure, N_f
P21-0-11	Air, 50% RH	8.021	4,238,700
P21-0-12	Air, 50% RH	7.753	2,312,080
P21-0-21	Air, 50% RH	7.534	1,561,280
P21-0-19	D. Water	7.713	369,162
P21-0-24	D. Water	7.209	207,493
P21-0-25	D. Water	7.612	268,239
P21-0-26	D. Water	7.763	842,304
P21-0-28	D. Water	7.602	208,293
P21-0-16	W. W. Fluid	7.761	1,304,978
P21-0-17	W. W. Fluid	7.288	770,689
P21-0-18	W. W. Fluid	7.288	284,265

4.2. Damage Assessment:

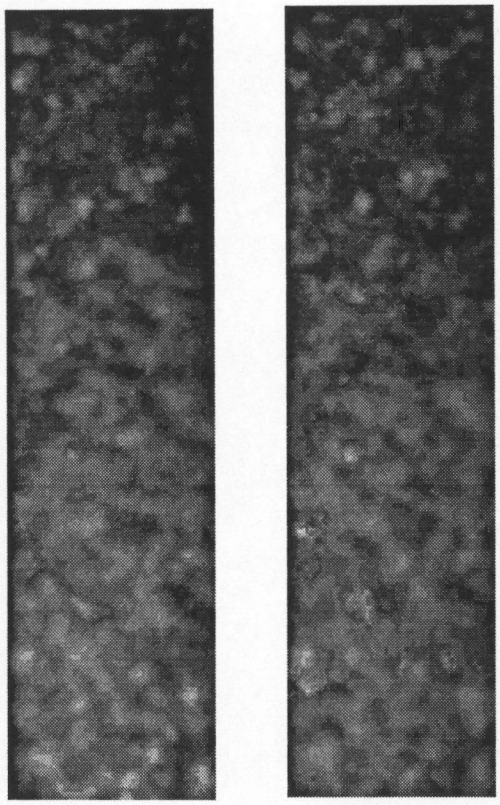
4.2.1. Creep:

The creep specimens were ultrasonically C-scanned at ORNL and brought to UTK for LTM imaging and SEM examination of fracture surfaces. Software image analysis was performed on the pre- and post-test C-scan and LTM images to determine any changes that were incurred during testing that might be attributed to damage. Documentation was made of damage characteristics on the fracture surfaces of selected samples, using SEM. The resulting images and analyses are presented in the following sections.

4.2.1.1. C-Scan Ultrasonics:

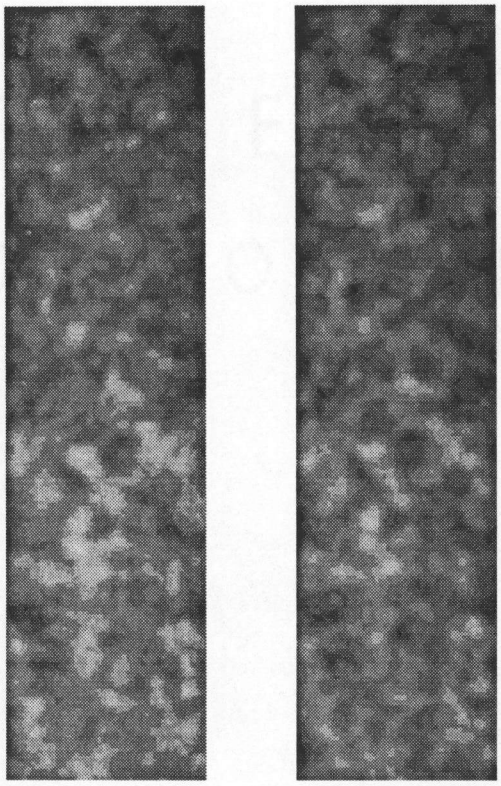
The pre- and post-test C-scan images for each sample were taken and compared to detect any changes. A tendency for the post-test image for each sample to be darker in overall appearance when compared to its respective pre-test image was consistently observed. Pre- and post-test C-scan images for selected samples are shown in Figures 4-1 through 4-3. Figure 4-1 shows the pre- and post-test images for sample P21-0-3, tested in air and 50% relative humidity. Figure 4-2 displays the pre- and post-test images for P21-0-10 which was tested in distilled water, and the pre- and post-test images for P21-0-9, tested in windshield washer fluid, appear in Figure 4-3.

Using the histogram function in Adobe Photoshop™ imaging software, the mean graylevel (MG) over an entire image was measured for both the pre- and post-test C-scans for each sample. The numerical data, gathered from these measurements, appears in Table 4-3. The lower the MG of the post-test image over that of the pre-test image indicates that the post-test image is darker in appearance. This darkening of the post-test image is



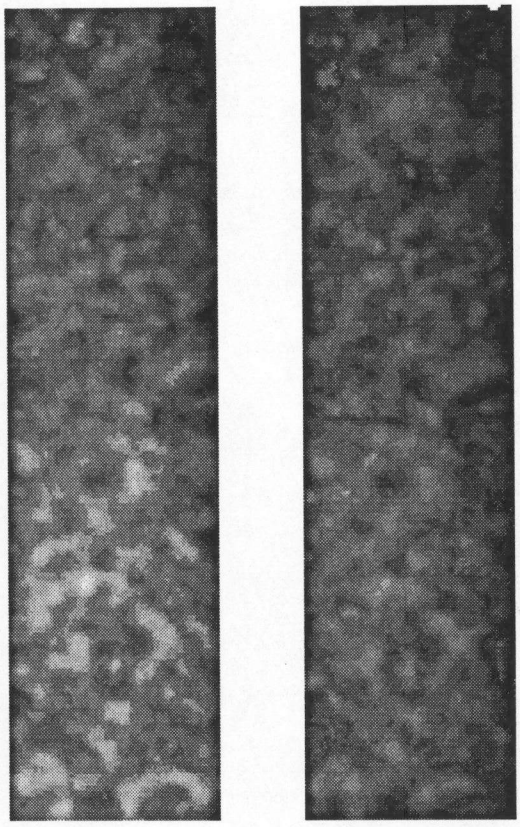
Pre-Test Post-Test

Figure 4-1. C-Scan Images of P21-0-3 (Air, 50% RH)



Pre-Test Post-Test

Figure 4-2. C-Scan Images of P21-0-10 (Distilled Water)



Pre-Test Post-Test

Figure 4-3. C-Scan Images of P21-0-9 (Windshield Washer Fluid)

Table 4-3. Mean Graylevel (MG) Measurements for Entire Pre- and Post-Test Creep Sample C-Scans

Specimen No.	Test Environ.	Pre-Test MG	Post-Test MG	Pre-Test Std. Dev.	Post-Test Std. Dev.
P21-0-3	Air, 50% R H	74.63	66.32	27.71	22.52
P21-0-27	Air, 50% R H	191.93	149.57	33.44	29.82
P21-0-5	D. Water	91.60	67.81	26.62	19.51
P21-0-10	D. Water	115.33	98.50	28.57	25.52
P21-0-22	D. Water	80.65	66.67	20.09	25.76
P21-0-7	W. W. Fluid	104.24	67.33	29.76	21.20
P21-0-8	W. W. Fluid	110.21	79.92	30.49	28.20
P21-0-9	W. W. Fluid	109.40	76.01	30.08	19.90

attributable to an increase in the scattering of transmitted sound waves within the samples due to damage. The % coefficient of variation (%CV) for each image was also calculated by dividing the standard deviation for each image by the MG value and multiplying by 100. This data appears in Table 4-4. Additionally, corresponding 256 pixel-square sections of each pre- and post-test C-scan image were randomly selected and measured for the MG and %CV values. From these sections, it was seen that the post-test MG values dropped and the %CV increased significantly when the section was close to the fracture surface. This data appears in the Appendix.

4.2.1.2. Light-Transmission Microscopy:

The pre- and post-test LTM images for each sample were taken as described in section 3.3. As stated previously, all pre- and post-test areas were visually examined but only selected images were taken for measurement. Comparison of the pre- and post-test images taken showed that while some post-test images were darker in appearance than their pre-test counterparts, others remained unchanged. The pre- and post-test LTM images for selected samples are shown in Figures 4-4 through 4-9. Figures 4-4 and 4-5 show the pre- and post-test states for image #16 for sample P21-0-27, tested in air and 50% relative humidity. The post-test image shows an area where individual fibers are now more visually distinct than in the pre-test image. Figures 4-6 and 4-7 display the pre- and post-test states for image #16 for P21-0-22 which was tested in distilled water, and the pre- and post-test states for image #10 for P21-0-7, tested in windshield washer fluid, appear in Figures 4-8 and 4-9. Arrows in each of the LTM images indicate areas having experienced interfacial debonding during creep testing. For both the selected distilled water and windshield washer fluid samples, the post-test images are slightly darker in appearance than their respective pre-test images.

Table 4-4. Coefficient of Variation (%) in Mean Graylevel for Entire Pre- and Post-Test Creep Sample C-Scans

Specimen No.	Pre-Test CV, %	Post-Test CV, %
P21-0-3	37.13	33.96
P21-0-27	17.42	19.94
P21-0-5	29.06	28.77
P21-0-10	24.77	25.91
P21-0-22	24.91	38.64
P21-0-7	28.55	31.49
P21-0-8	27.67	35.29
P21-0-9	27.50	26.18

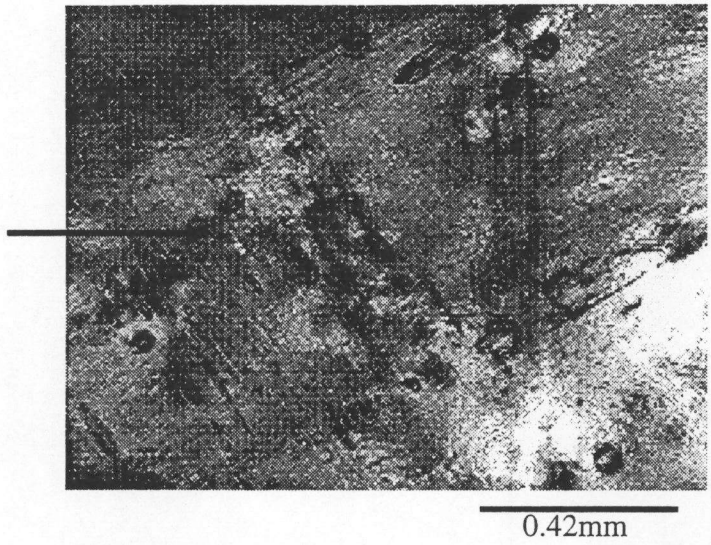


Figure 4-4. LTM Image of P21-0-27 (Air, 50% RH)

Pre-Test Image #16

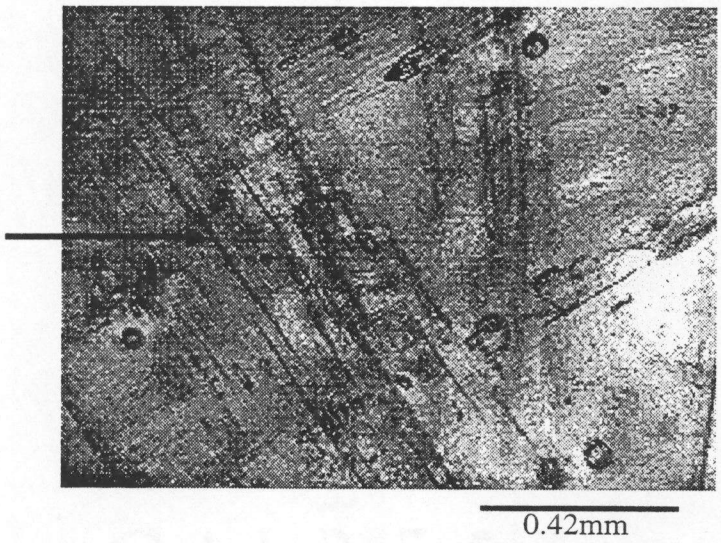


Figure 4-5. LTM Image of P21-0-27 (Air, 50% RH)

Post-Test Image #16 (No Fracture)

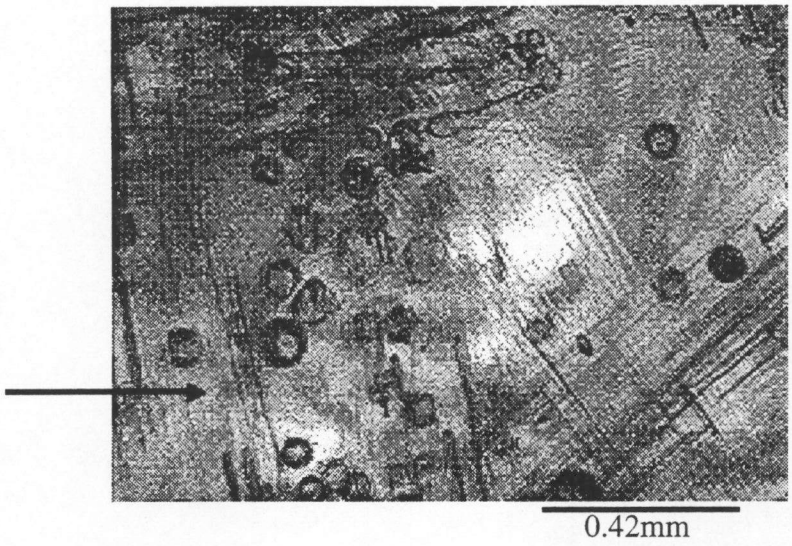


Figure 4-6. LTM Image of P21-0-22 (Distilled Water)

Pre-Test Image #16

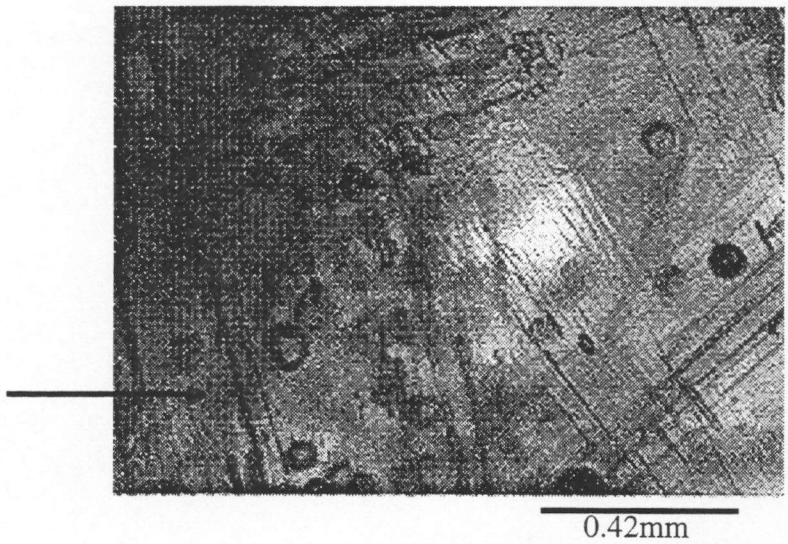


Figure 4-7. LTM Image of P21-0-22 (Distilled Water)

Post-Test Image #16 (Approx. 2.0 cm From Fracture)

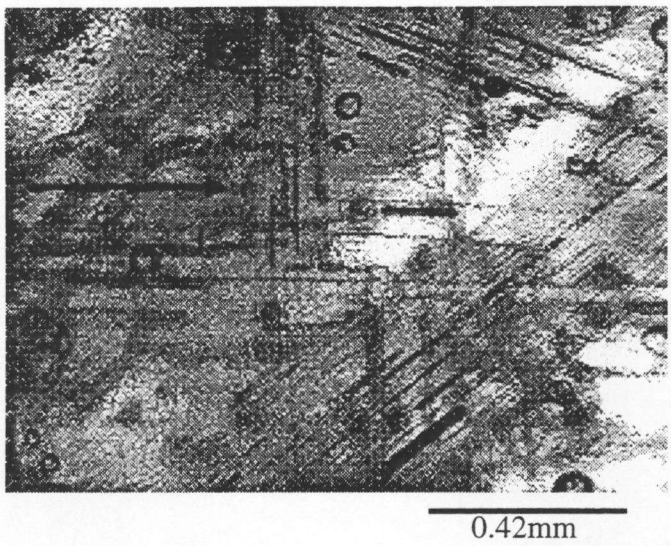


Figure 4-8. LTM Image of P21-0-7 (Windshield Washer Fluid)

Pre-Test Image #10

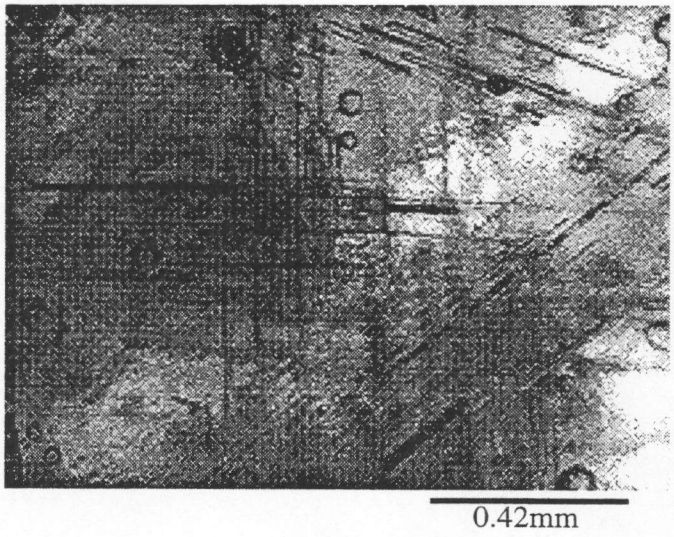


Figure 4-9. LTM Image of P21-0-7 (Windshield Washer Fluid)

Post-Test Image #10 (Approx. 9.0 cm From Fracture)

As in the case of the C-scan images, the mean graylevel for each pre- and post-test image was determined, using the histogram function in Adobe Photoshop™. Likewise, the % coefficient of variation for each image was also calculated. The numerical data, gathered from these measurements, appears in the Appendix. The trends in the MG and %CV for the pre- and post-test LTM images were not as obvious as in the case of the C-scan images. Generally, however, when the sample failed within the 18 image range, those post-test images close to the fracture surface did show a decrease in MG and an increase in %CV.

4.2.1.3. Scanning Electron Microscopy:

The fracture surfaces of selected creep tested samples were examined using SEM to document damage and compare the effect of the different environments. Unfortunately, the samples creep tested in air and 50% relative humidity were discontinued due to time constraints and, therefore, did not fracture. However, images were taken on the side of the samples to determine any evidence of damage. The samples, tested in distilled water and windshield washer fluid, were investigated for comparison. Images were made using the backscattered electron mode at 20 KeV to minimize specimen charging effects with a 20 Pa compressed air purge to achieve high resolution. Figures 4-10 and 4-11 are SEM images of the side of P21-0-3 which was creep tested in air, 50% relative humidity. Both images clearly show microcracks in the side of the sample, lying perpendicular to the axis of load. From this evidence, it is believed these samples were close to failure. Figures 4-12 through 4-14 are SEM images of P21-0-10 which was creep loaded in distilled water. Figure 4-12 specifically shows the proliferation of river patterns, commomly associated with brittle fracture, over a single area of matrix. These river patterns were found to be widely distributed over much of the fracture surface. Figure 4-13 shows also an individual

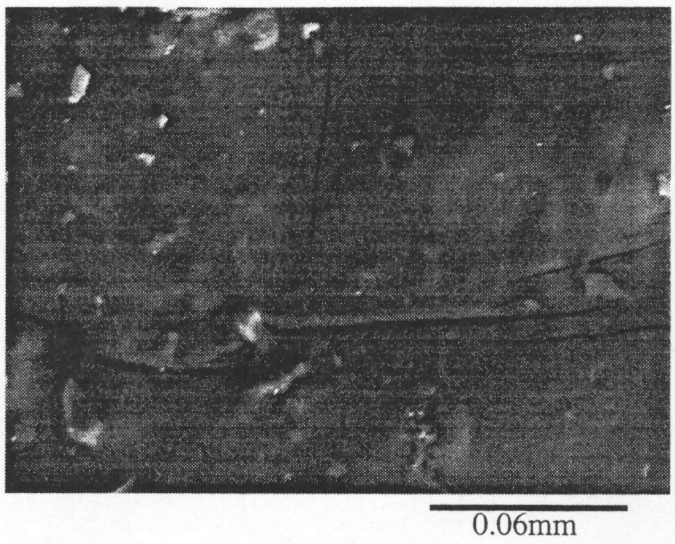


Figure 4-10. SEM Image of P21-0-3 (Air, 50% RH) at 20 KeV, 450x Showing Microcracks, Perpendicular to Load Axis, on Specimen Side

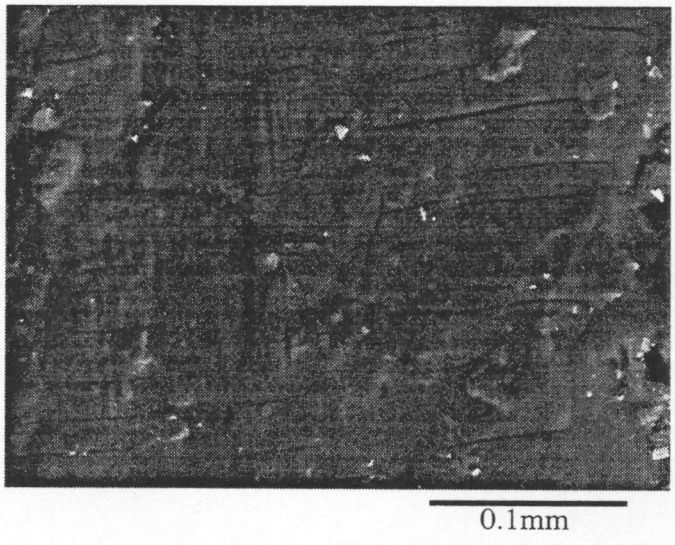


Figure 4-11. SEM Image of P21-0-3 (Air, 50% RH) at 20 KeV, 250x Showing Microcracks, Perpendicular to Load Axis, on Specimen Side

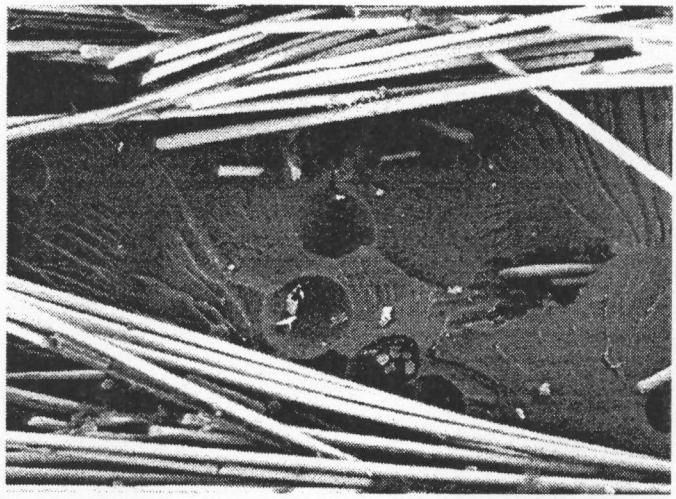


Figure 4-12. SEM Image of P21-0-10 (Distilled Water) at 20 KeV, 90x Showing Several River Patterns

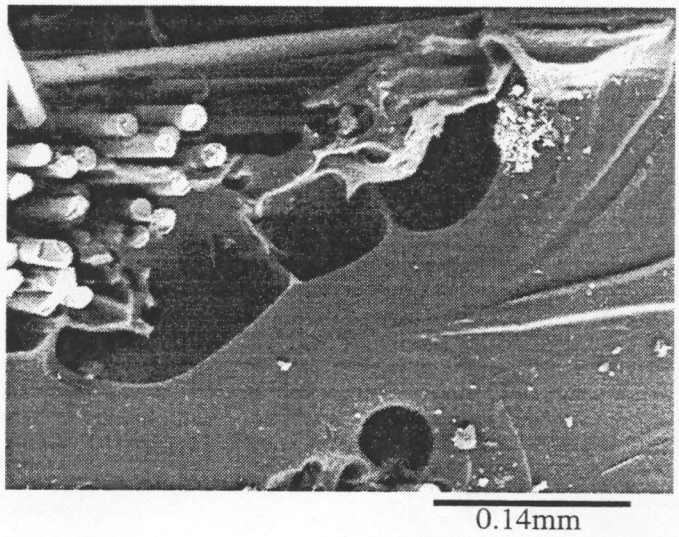


Figure 4-13. SEM Image of P21-0-10 (Distilled Water) at 20 KeV, 180x Showing River Pattern Originating at Fiber Bundle With Air Voids

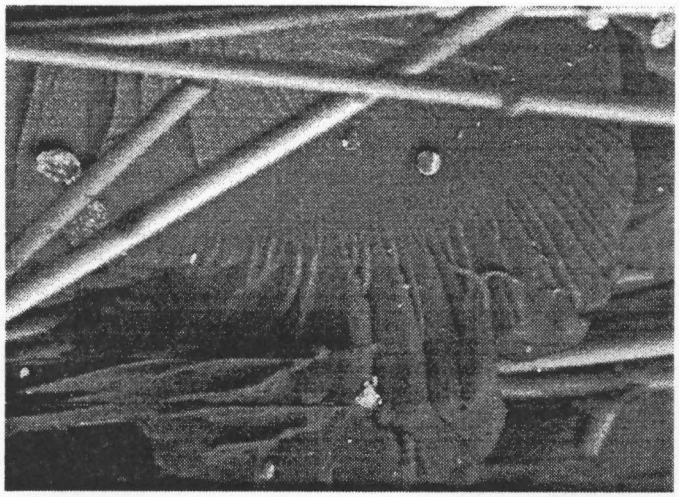


Figure 4-14. SEM Image of P21-0-10 (Distilled Water) at 20 KeV, 200x
Showing Brittle Fracture Bands

river pattern that fans outward from a bundle of fibers that are surrounded by air bubbles. Brittle fracture bands are distinctively displayed in Figure 4-14, as the step-like formations are unmistakeable.

Figures 4-15 through 4-18 are SEM images of P21-0-7 which was creep tested in windshield washer fluid. As Figure 4-15 clearly shows, good fiber/matrix interfacial bonding was evident, as matrix material was exhibited still clinging to the glass fibers after failure. Figure 4-16 through 4-18 show areas of matrix, surrounding fiber bundles and air voids, that were relatively free of the river patterns and brittle fracture bands, typical of brittle fracture. Such areas were widely distributed over most of the fracture surface.

4.2.2. Fatigue:

As was done for the creep specimens, the fatigue samples were also ultrasonically C-scanned at ORNL and brought to UTK for LTM imaging and SEM

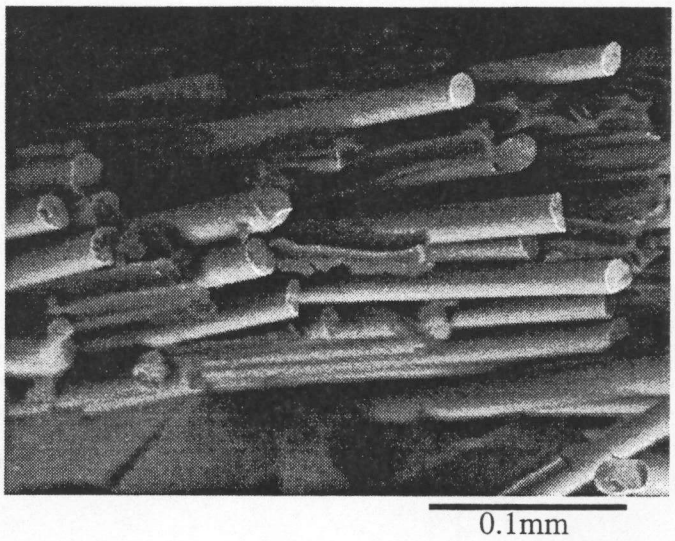


Figure 4-15. SEM Image of P21-0-7 (Windshield Washer Fluid) at 20 KeV, 250x Showing Matrix Still Bonded to Fibers

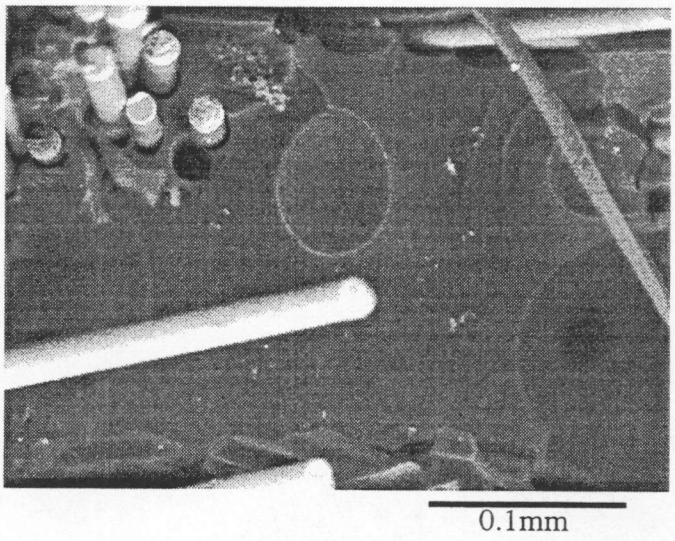


Figure 4-16. SEM Image of P21-0-7 (Windshield Washer Fluid) at 20 KeV, 250x Showing Voids in Matrix

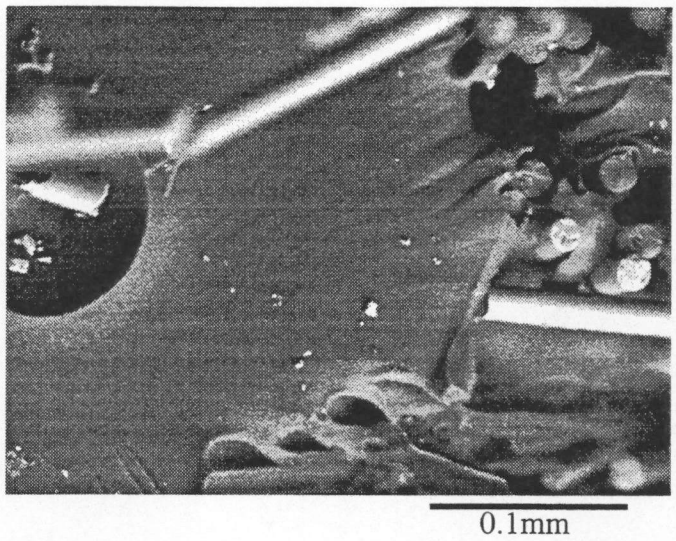


Figure 4-17. SEM Image of P21-0-7 (Windshield Washer Fluid) at 20 KeV, 250x Showing Smooth Matrix Surrounding Fiber Bundles

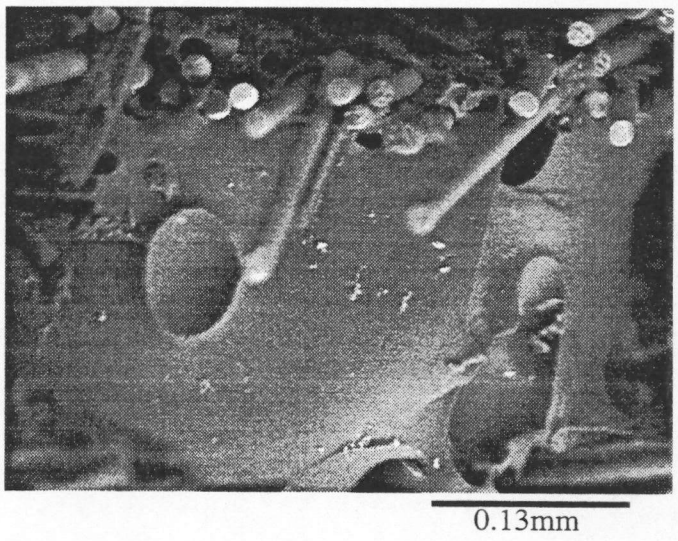


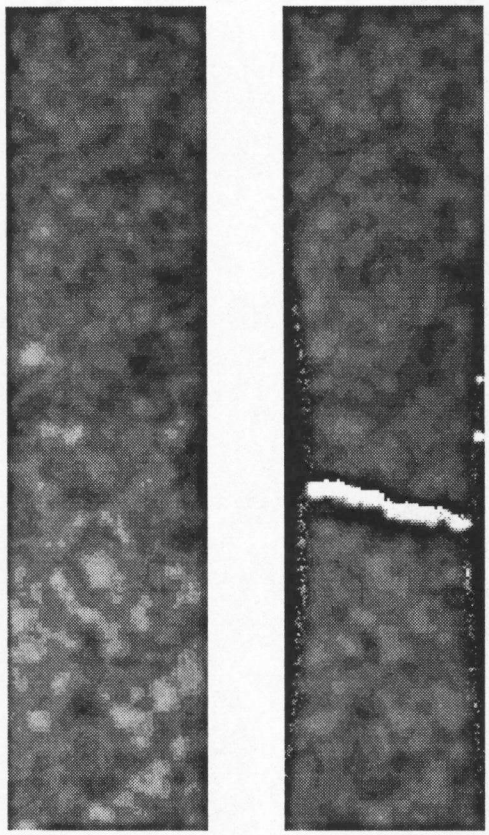
Figure 4-18. SEM Image of P21-0-7 (Windshield Washer Fluid) at 20 KeV, 200x Showing Smooth Matrix Surrounding Fiber Bundles and Voids

examination. Any changes in the pre- and post-test C-scan and LTM images that might have been indicative of damage, sustained during testing, were assessed through software image analysis. SEM was used to chronicle any damage characteristics on the fracture surfaces of selected samples. The following sections give the resulting images and measurements.

4.2.2.1. C-Scan Ultrasonics:

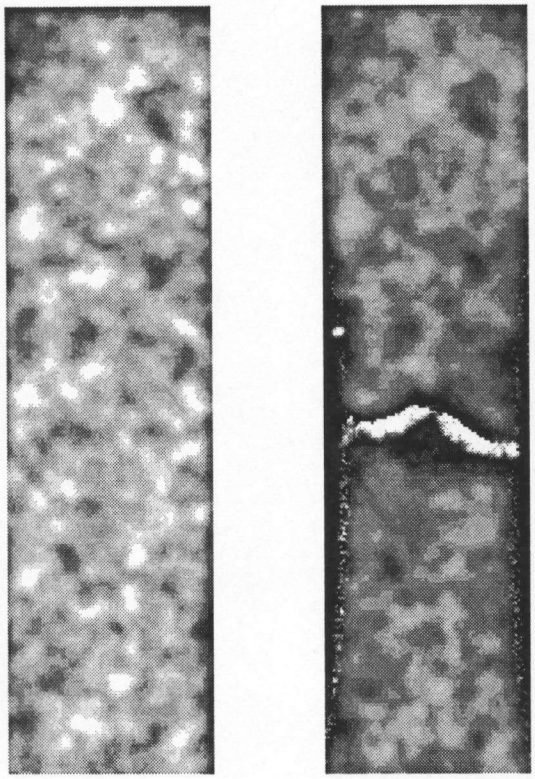
As was previously done for the C-scans for the creep tested samples, the pre- and post-test images for each fatigue sample were compared to discern any changes. The same tendency for the post-test image of each sample to be darker in overall appearance than the pre-test image was again distinguished. Pre- and post-test C-scan images for selected samples are shown in Figure 4-19 through 4-21. The pre- and post-test images for sample P21-0-11, tested in air and 50% relative humidity, are shown in Figure 4-19. Pre- and post-test images for P21-0-26, tested in distilled water, are presented in Figure 4-20, and Figure 4-21 shows the pre- and post-test images for P21-0-18, tested in windshield washer fluid.

Likewise, the mean graylevel (MG) was determined for these C-scans, using the histogram function in Adobe Photoshop™ as was described earlier for the creep samples. Table 4-5 displays the mean graylevel values for the pre- and post-test images for each sample. Also, the % coefficient of variation (%CV) was calculated for the fatigue samples as was described earlier in Section 4.2.1.1. These values appear in Table 4-6. Again, corresponding 256 pixel-square sections were randomly selected on the pre- and post-test images, and the MG and %CV measured. As for the creep samples, this data appears in the Appendix. This data displayed the same general trends as the creep samples, but the



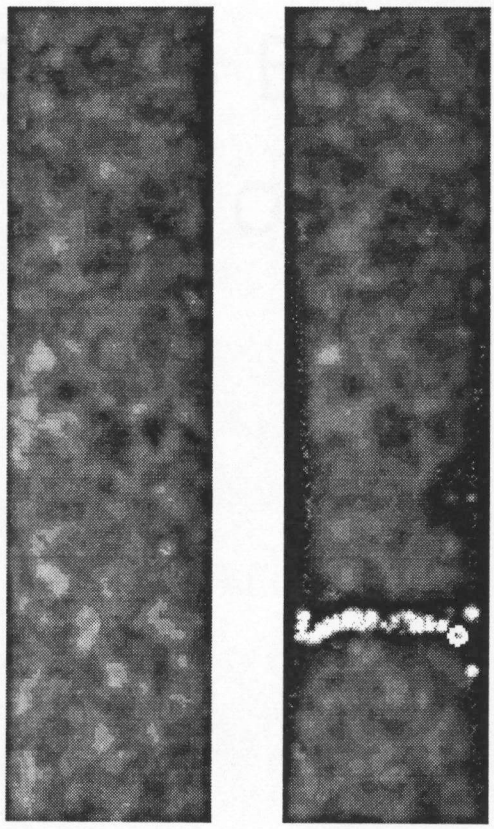
Pre-Test Post-Test

Figure 4-19. C-Scan Images of P21-0-11 (Air, 50% RH)



Pre-Test Post-Test

Figure 4-20. C-Scan Images of P21-0-26 (Distilled Water)



Pre-Test Post-Test

Figure 4-21. C-Scan Images of P21-0-18 (Windshield Washer Fluid)

Table 4-5. Mean Graylevel (MG) Measurements for

Entire Pre- and Post-Test Fatigue Sample C-Scans

Specimen No.	Test Environ.	Pre-Test MG	Post-Test MG	Pre-Test Std. Dev.	Post-Test Std. Dev.
P21-0-11	Air, 50% R H	103.95	79.94	27.41	33.54
P21-0-12	Air, 50% R H	91.27	71.10	24.58	27.09
P21-0-21	Air, 50% R H	58.50	59.49	18.98	52.64
P21-0-19	D. Water	87.64	69.79	21.05	38.89
P21-0-25	D. Water	154.56	101.38	37.24	41.19
P21-0-26	D. Water	189.82	124.27	36.34	50.80
P21-0-16	W. W. Fluid	98.84	70.49	22.87	33.37
P21-0-17	W. W. Fluid	100.45	72.21	25.78	40.04
P21-0-18	W. W. Fluid	99.44	72.53	26.06	35.96

Table 4-6. Coefficient of Variation (%) in Mean Graylevel for Entire Pre- and Post-Test Fatigue Sample C-Scans

Specimen No.	Pre-Test CV, %	Post-Test CV, %
P21-0-11	26.37	41.96
P21-0-12	26.93	38.10
P21-0-21	32.44	88.49
P21-0-19	24.02	55.72
P21-0-25	24.09	40.63
P21-0-26	19.14	40.88
P21-0-16	23.14	47.34
P21-0-17	25.66	55.45
P21-0-18	26.21	49.58

changes for fatigue were significantly greater than for creep.

4.2.2.2. Light-Transmission Microscopy:

As was seen with the LTM images for the creep samples, some of the fatigue post-test images displayed no change when compared to their respective pre-test images, and yet others appeared darker. Figures 4-22 through 4-27 show the pre- and post-test LTM images for selected samples. Pre- and post-test states for image #16 for sample P21-0-11, which was tested in air and 50% relative humidity, are represented in Figures 4-22 and 4-23. Figures 4-24 and 4-25 show the pre- and post-test states for image #8 for P21-0-25, tested in distilled water. Likewise, Figures 4-26 and 4-27 display the pre- and post-test states for image #12 for P21-0-18, which was tested in windshield washer fluid. For each of the selected samples shown, the post-test images appear darker than their respective pre-test images. Also, there are areas in each post-test image where individual fibers are more discernible than in the pre-test image. Areas of interest for having undergone interfacial debonding during fatigue testing are indicated in each LTM image by an arrow.

Adobe Photoshop™ was again employed to determine the mean graylevel over the entirety of each pre- and post-test image, and the % coefficient of variation for each image was calculated. The data for the MG measurements, acquired for these samples, appears in the Appendix. As mentioned previously, when the sample failed within the 18 image range, there was a decrease in MG and an increase in %CV values for those post-test LTM images near the fracture surface.

4.2.2.3. Scanning Electron Microscopy:

As was done for the creep samples, SEM was used to examine the fracture surfaces

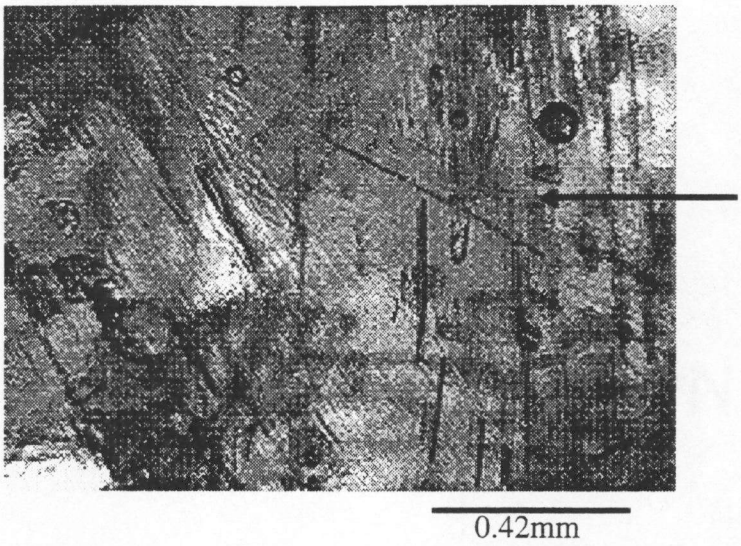


Figure 4-22. LTM Image of P21-0-11 (Air, 50% RH)

Pre-Test Image #16

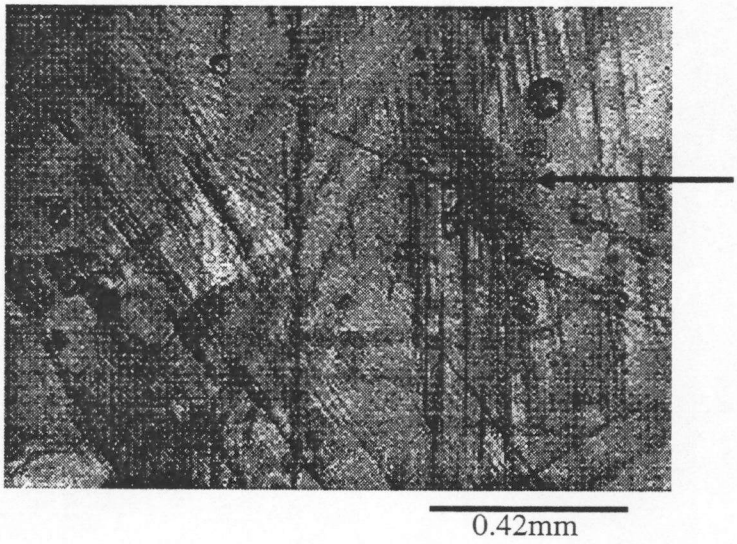


Figure 4-23. LTM Image of P21-0-11 (Air, 50% RH)

Post-Test Image #16 (Approx. 0.6 cm From Fracture)

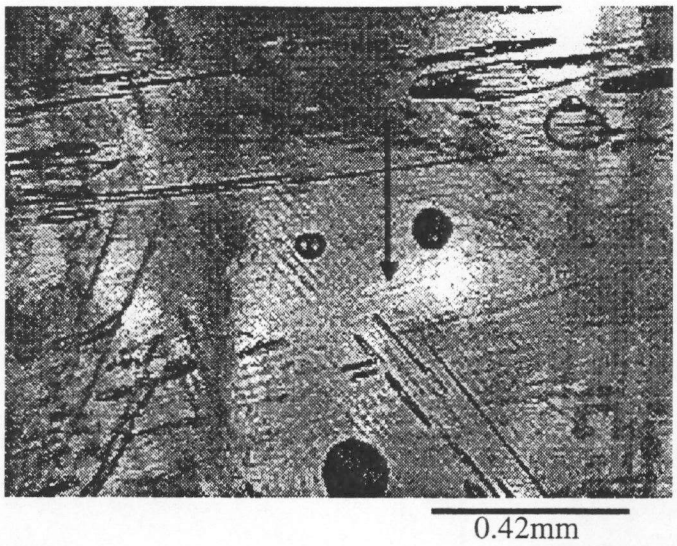


Figure 4-24. LTM Image of P21-0-25 (Distilled Water)

Pre-Test Image #8

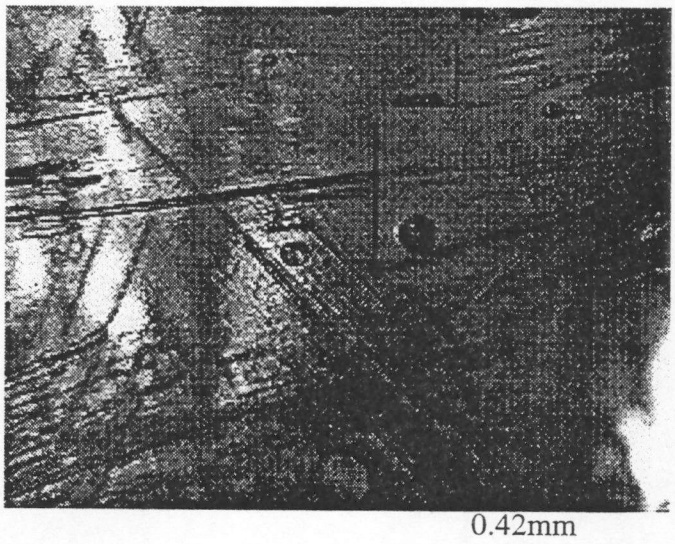


Figure 4-25. LTM Image of P21-0-25 (Distilled Water)

Post-Test Image #8 (Fracture)

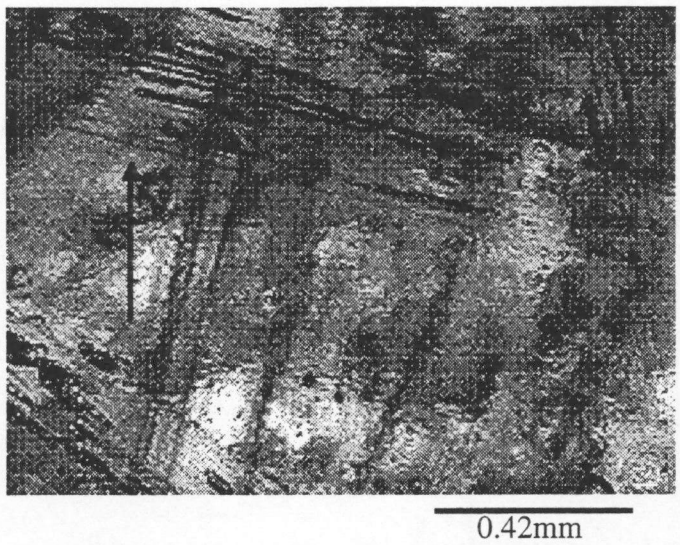


Figure 4-26. LTM Image of P21-0-18 (Windshield Washer Fluid)

Pre-Test Image #12

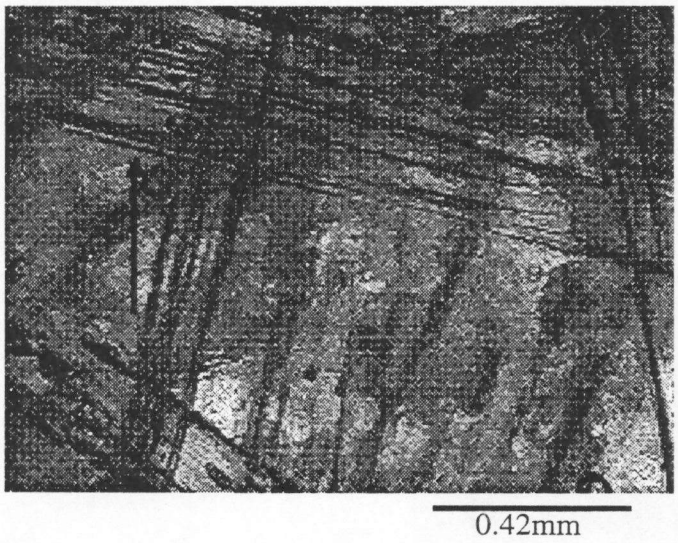


Figure 4-27. LTM Image of P21-0-18 (Windshield Washer Fluid)

Post-Test Image #12 (Approx. 0.2 cm From Fracture)

of fatigue loaded samples. Samples were selected from each of the environments for inspection to determine damage and environmental effects. As stated previously for the creep specimens, the fatigued samples were imaged in the backscattered electron mode at 20 KeV with a 20 Pa compressed air purge to achieve high resolution and minimize specimen charging effects. Figures 4-28 and 4-29 are SEM images of P21-0-11 which was fatigue tested in air, 50% relative humidity. Both Figures 4-28 and 4-29 show areas of matrix that are covered with river patterns, extending from fiber bundles. Figure 4-29 also shows bits of matrix debris clinging to individual fibers, usually evidence of good adhesion at the interface. Figures 4-30 through 4-33 are SEM images of P21-0-25 which was fatigued in distilled water. Figure 4-30 shows brittle fracture bands while Figures 4-31 through 4-33 show more river patterns, usually extending from fiber bundles or from where fibers once existed prior to failure. This proliferation of brittle fracture characteristics was confirmed over the majority of the fracture surface. Also, Figures 4-32 and 4-33 showed some evidence of clean fibers, indicating poor fiber/matrix interfacial bonding. Figures 4-34 through 4-37 are SEM images of P21-0-17 which was fatigued in windshield washer fluid. Good adhesion between the fiber and the matrix was documented as shown in Figure 4-34 by the matrix material still bonded to the fibers after fracture. Figures 4-35 through 4-37 showed areas of smooth matrix, surrounding fiber bundles or places of fiber debonding and pull-out. These areas,which were noticeably free of river patterns and brittle fracture bands, were located over much of the fracture surface.

In addition to the backscatter images of the selected samples, secondary electron images were made of a sample, chosen at random, in an effort to document crack propagation during failure. Figures 4-38 and 4-39 are SEM images of the side of distilled water sample P21-0-25, taken at 1.5 KeV. Figure 4-39 is a continuation of the area shown at the right in Figure 4-38. From these images, it appeared that cracks tended to propagate

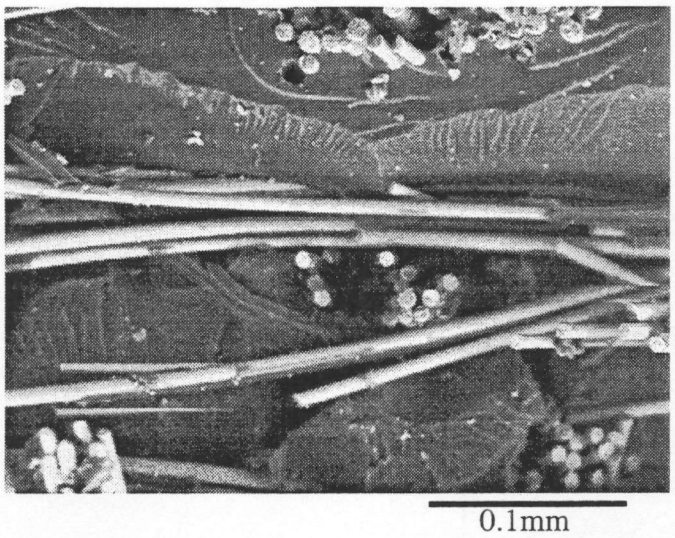


Figure 4-28. SEM Image of P21-0-11 (Air, 50% RH) at 20 KeV, 120x

Showing River Patterns Extending From Fiber Bundles

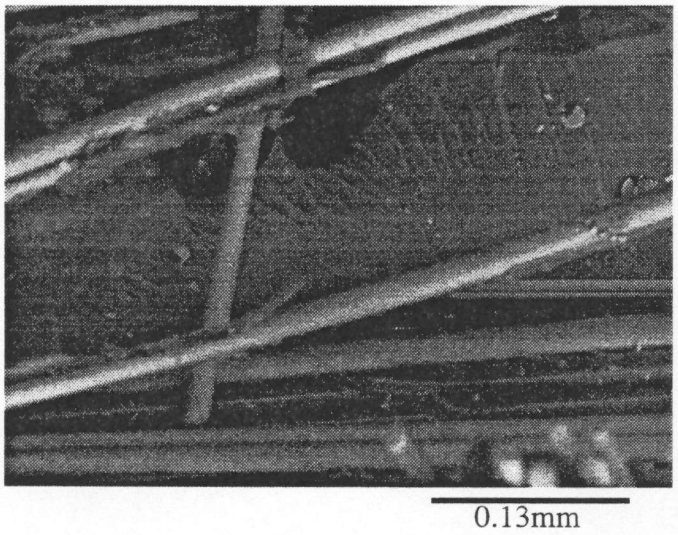


Figure 4-29. SEM Image of P21-0-11 (Air, 50% RH) at 20 KeV, 200x

Showing River Patterns and Matrix Clinging to Fibers

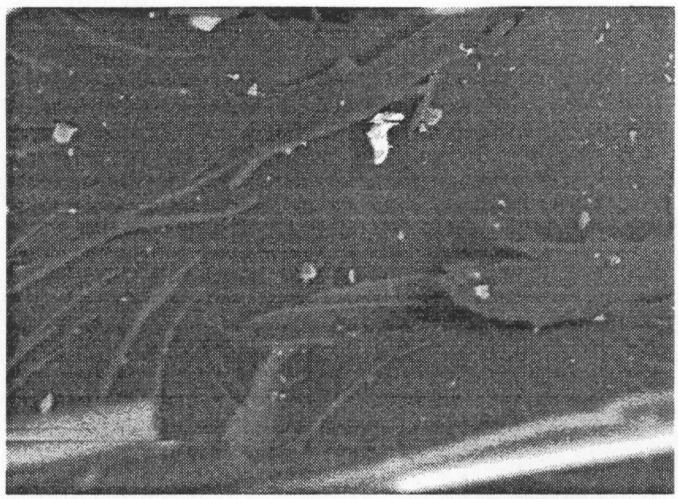


Figure 4-30. SEM Image of P21-0-25 (Distilled Water) at 20 KeV, 200x Showing Brittle Fracture Bands

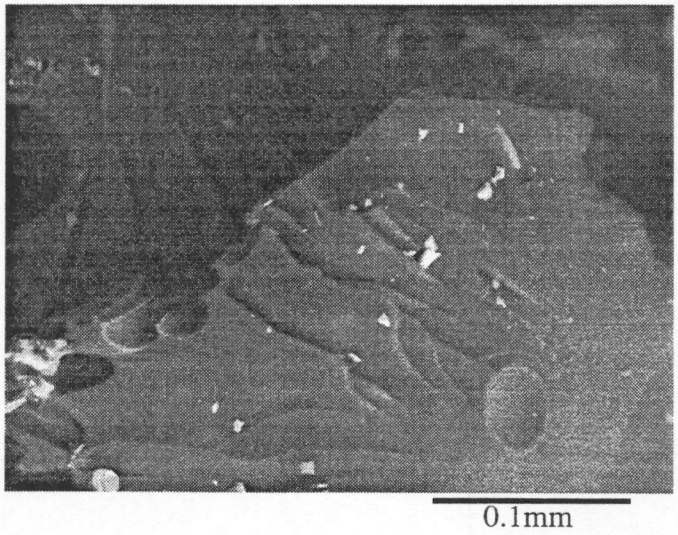


Figure 4-31. SEM Image of P21-0-25 (Distilled Water) at 20 KeV, 250x Showing River Patterns Extending From Area of Fiber Pull-Out



Figure 4-32. SEM Image of P1-0-25 (Distilled Water) at 20 KeV, 200x

Showing River Pattern Extending From Fiber Bundles

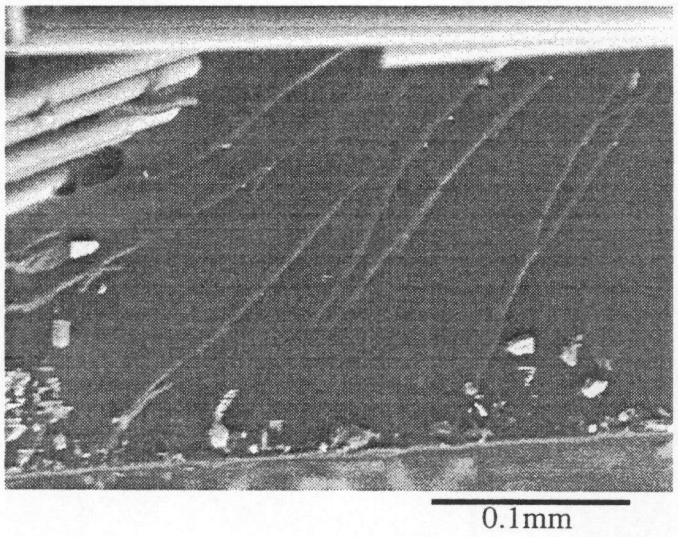


Figure 4-33. SEM Image of P21-0-25 (Distilled Water) at 20 KeV, 250x

Showing River Patterns and Clean Fibers

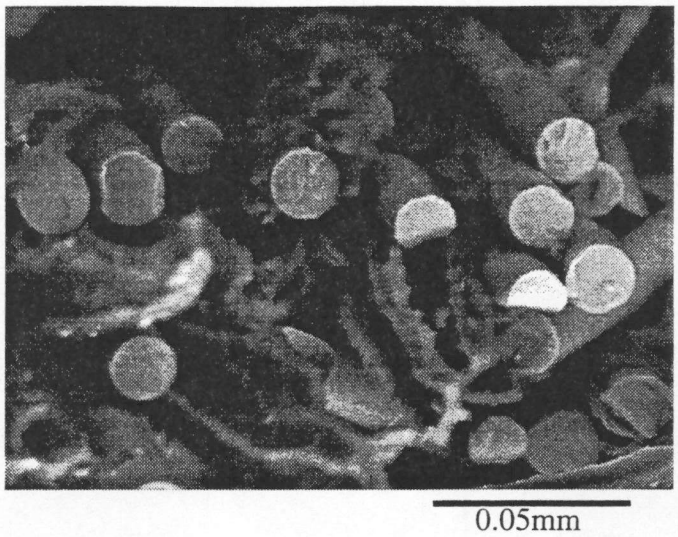


Figure 4-34. SEM Image of P21-0-17 (Windshield Washer Fluid) at 20 KeV, 500x Showing Matrix Still Bonded to Fibers

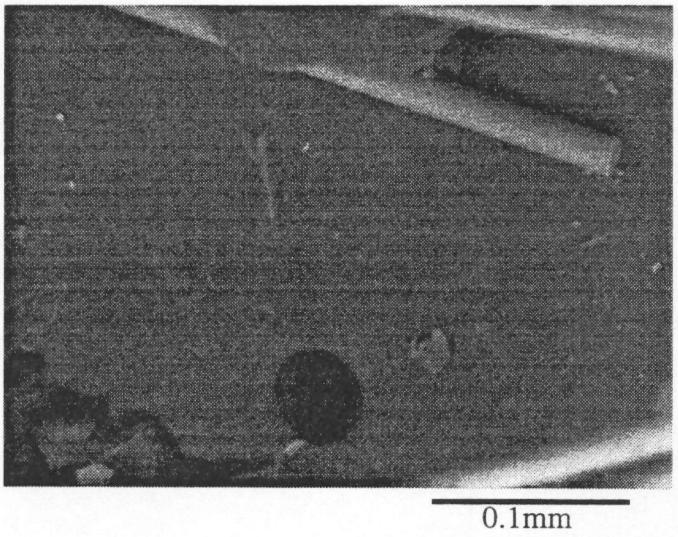


Figure 4-35. SEM Image of P21-0-17 (Windshield Washer Fluid) at 20 KeV, 250x Showing Smooth Matrix Area With Void

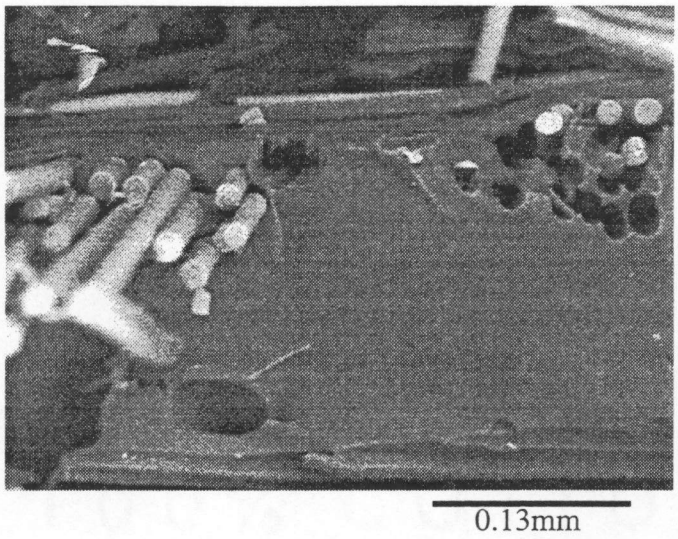


Figure 4-36. SEM Image of P21-0-17 (Windshield Washer Fluid) at 20 KeV, 200x Showing Smooth Matrix Surrounding Fibers and Area of Debonding

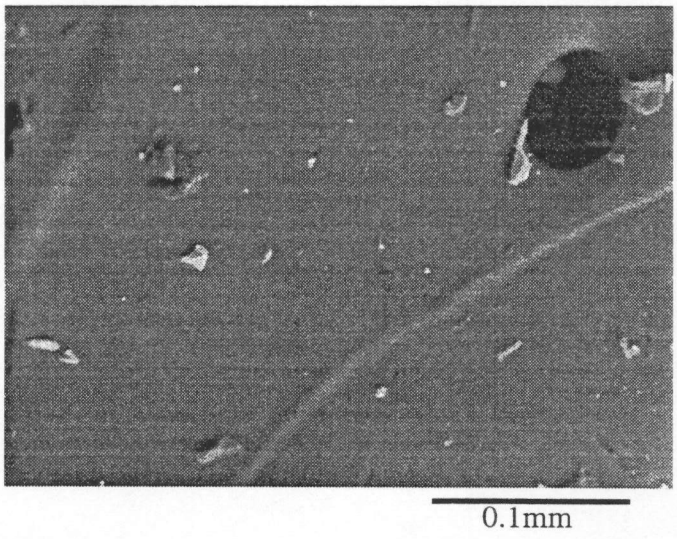


Figure 4-37. SEM Image of P21-0-17 (Windshield Washer Fluid) at 20 KeV, 250x Showing Smooth Matrix Scattered With Debris

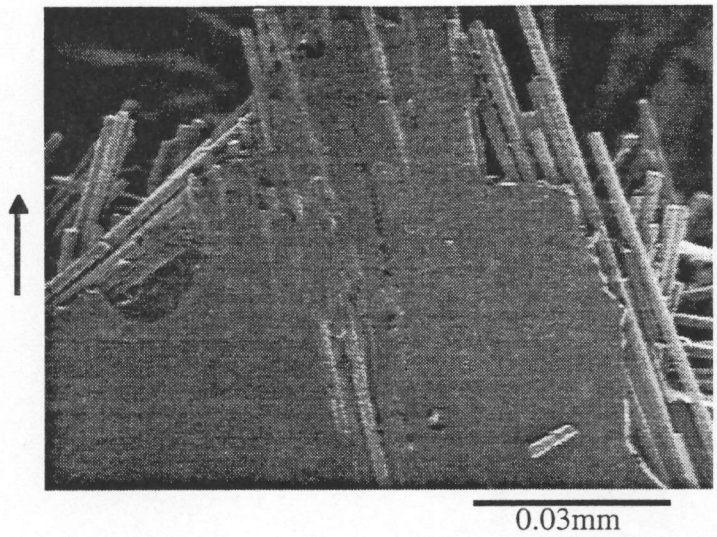


Figure 4-38. SEM Image of P21-0-25 (Distilled Water) at 1.5 KeV, 70x Showing Propagation of Fracture Along Fiber Bundles

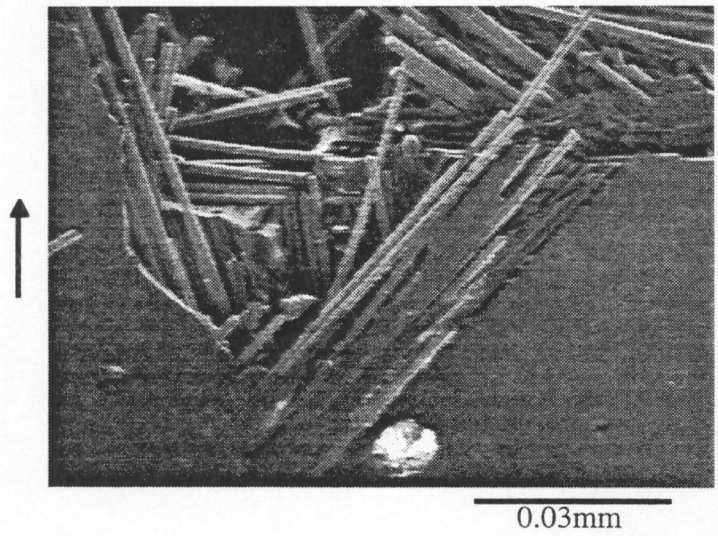


Figure 4-39. SEM Image of P21-0-25 (Distilled Water) at 1.5 KeV, 70x Showing Propagation of Fracture Along Fiber Bundles

along fiber bundles, apparently jumping from one fiber bundle to the next or from bundle to air void to bundle, etc. Figures 4-40 and 4-41 are SEM images of the edge of the fracture surface of P21-0-25 taken from a side angle at 1.5 KeV. In Figure 4-40, the cracking of the matrix is shown to have followed along a fiber bundle that is lying nearly perpendicular to the axis of load. In Figure 4-41, propagation of fracture is again shown to follow fiber bundles. This is further confirmed by the brittle fracture bands shown originating from the fiber bundle in the background of the image, lying perpendicular to the load direction. Arrows beside the photos indicate the axis of load.

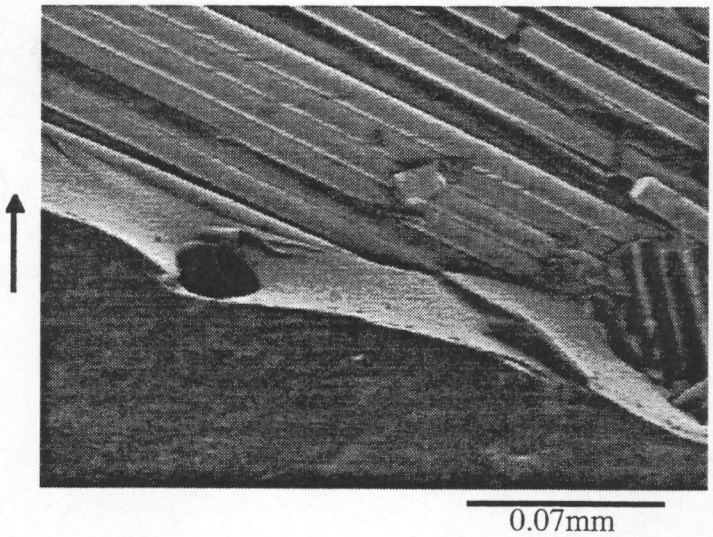


Figure 4-40. SEM Image of P21-0-25 (Distilled Water) at 1.5 KeV, 200x Showing Crack Propagation at the Edge of the Fracture Surface

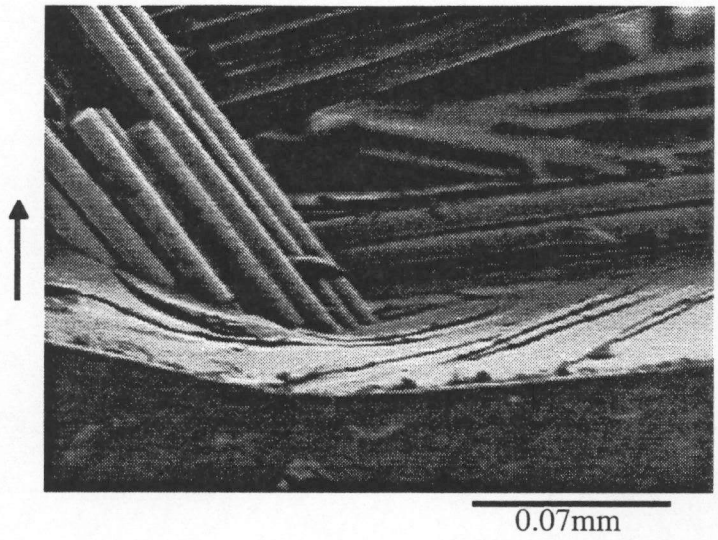


Figure 4-41. SEM Image of P21-0-25 (Distilled Water) at 1.5 KeV, 200x Showing Brittle Fracture Bands on the Fracture Surface

V. DISCUSSION

5.1. Mechanical Properties:

As stated previously, it was necessary to test the CSM composite in environmental conditions that it may experience in application in order to understand the material's behavior while in use. To determine what effects the chemical environments have on the CSM composite, investigation of the solubility parameters of the solvents and composite materials was essential. The diffusion of certain liquid environments into a polymer material are known to affect the mechanical properties by plasticizing the polymer. In previous independent studies, it has been shown that the difference in the solubility parameters between a polymer and a possible liquid solvent can be considered a measure of plasticization efficiency. As the difference in the solubility parameters for the polymer and the liquid approaches zero, the ability for the liquid to plasticize the polymer increases.(6) This effect is usually manifested as a shifting of the glass transition temperature, T_g, of the polymer or polymer matrix, depending on the amount of plasticizer that diffuses the material. An increase in plasticizer generally means there is a lowering of the T_g, meaning a decrease in the stiffness of the polymer material as it becomes more flexible or pliable. Table 5-1 gives the solubility parameters for polyurethane and and common fluids. Distilled water and methanol were used as solvents in this research.

Previously, weight gain and weight loss studies were performed at ORNL on samples of the subject CSM composite that were exposed to distilled water and windshield washer fluid for 11,160 hrs and then allowed to dry in air for 1000 hrs.(14) Figures 5-1 and 5-2 are graphical representations of the weight gain and weight loss data for those samples. As can be seen in Figure 5-1, the windshield washer fluid samples experienced a

Table 5-1. Solubility Parameters for Polyurethane and Some Common Liquids (23)

Material	Solubility Parameter, $MPa^{1/2}$	H-Bonding Index
Polyurethane	26.0	-
Water	47.8	39.0
Methanol	29.6	18.7
Isopropyl Alcohol	23.4	18.7

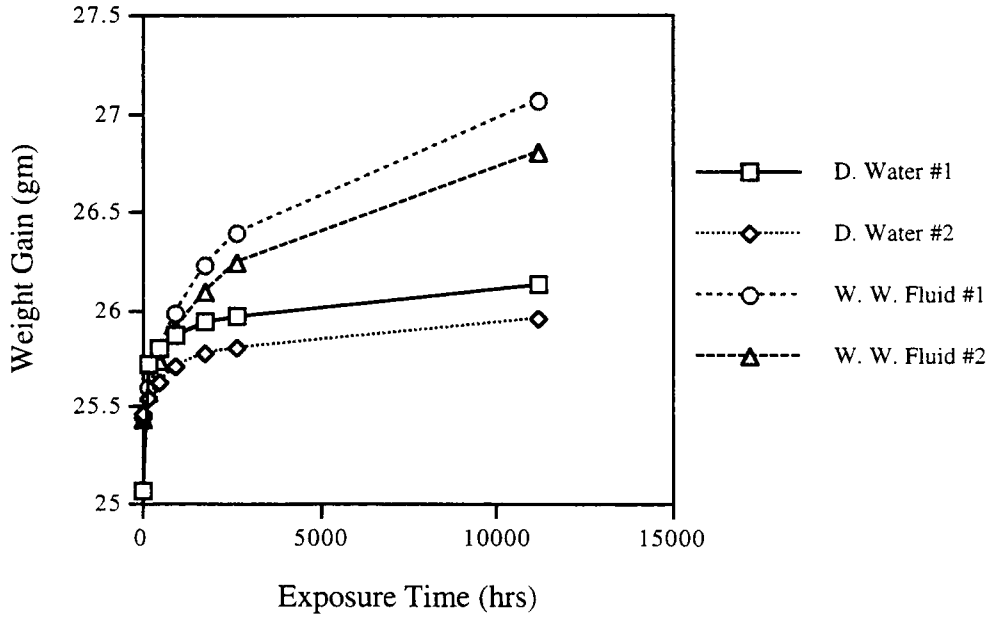


Figure 5-1. Weight Gain per Hour for CSMC Samples Exposed for 11,160 hrs.

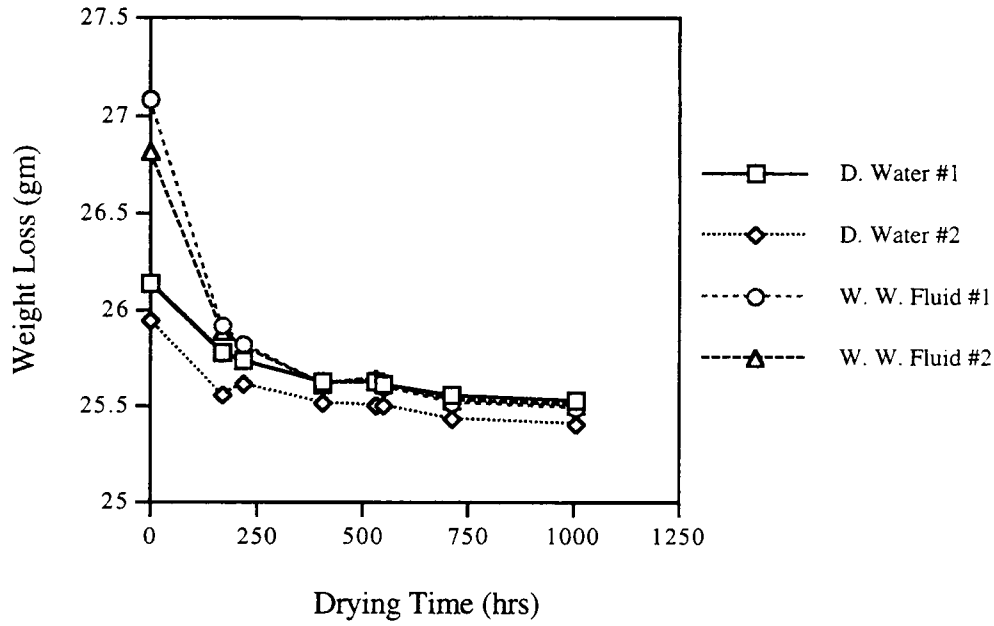


Figure 5-2. Weight Loss per Hour for CSMC Samples Exposed for 11,160 hrs.

greater uptake of fluid than the distilled water samples. From Figure 5-2, it is shown that after drying in air, most of the samples nearly returned to their respective weights prior to exposure.

The diffusion of liquid environments into the composite while under load depends on the type of loading. The nature of creep loading allows any cracks or interfacial debonds in the composite to open and remain so, permitting liquid environments the time to diffuse and plasticize the matrix and/or attack at the interface. In the case of fatigue, the nature of the loading is dynamic, which means that any cracks or interfacial debonds are opening and closing repeatedly. This type of loading behavior may not allow the liquid environments the same opportunities to diffuse into and plasticize the matrix or attack the interface as does creep. However, from prolonged exposure, it is conceivable that some plasticization and/or interfacial attack will occur.

5.1.1. Creep:

For the creep samples, comparison was made of the average creep strain per environment as shown in Figure 5-3. As can be seen, the windshield washer fluid affected the CSM composite material by increasing the average creep strain 76% over the air, 50% RH samples, and the effect of the distilled water was an increase of 68%. Independent studies have shown that % creep strain of the CSM composite is 0.35% at a load of 14 ksi, respectively, when exposed to distilled water.(21) Moreover, since this was a polyurethane matrix composite, the windshield washer fluid was expected to decrease the stiffness of the composite because the solubility parameter of the methanol in windshield washer fluid is relatively close to that of polyurethane. This closeness in the solubility parameters leads to plasticization which causes the matrix to become more flexible on a

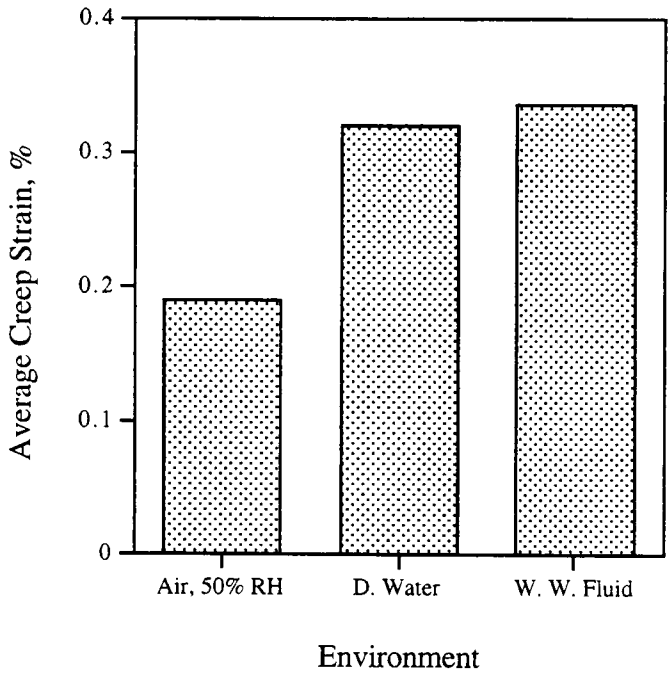


Figure 5-3. Average Creep Strain, %, per Environment

microscopic scale, allowing for a greater plastic deformation of the matrix without incurring noticeable amounts of damage during static loading. When looking at the solubility parameters of the matrix material and the windshield washer fluid environment in Table 5-1, the similarities in the values indicate that plasticization of the matrix may have occurred and was the cause for these observed increases. Because the solubility parameter of distilled water is not close in value to that of polyurethane, it was not expected to swell the matrix but instead attack the glass fiber reinforcement at the interface as the creep loading allows debonded interfaces to remain open. Indeed, it has already been shown in independent studies of swelling in fluids, undertaken by ORNL, that greater dimensional changes are evident in windshield washer fluid samples but not as significantly with distilled water. The windshield washer fluid was shown to increase the sample thickness by nearly 5% whereas distilled water only increased the thickness by approximately 1.25%.(5)

5.1.2. Fatigue:

For the fatigue samples, comparison was made of the average cycles-to-failure per environment as shown in Figure 5-4. As can be seen, the distilled water affected the CSM composite material by decreasing the average cycles-to-failure 82% from that of the air, 50% RH samples, and the effect of the windshield washer fluid was a decrease of 71%. During fatigue, the opening and closing of cracks and interfacial debonds decreases the opportunities for the liquid environments to diffuse into and plasticize the matrix material but does not eliminate them altogether. However, the fiber/matrix interfacial debonding is steadily increasing as the dynamic loading increases. Since the distilled water attacks the glass fiber reinforcement at the interface, the distilled water environment had the effect of severely decreasing the fatigue life of the CSM composite. The windshield washer fluid

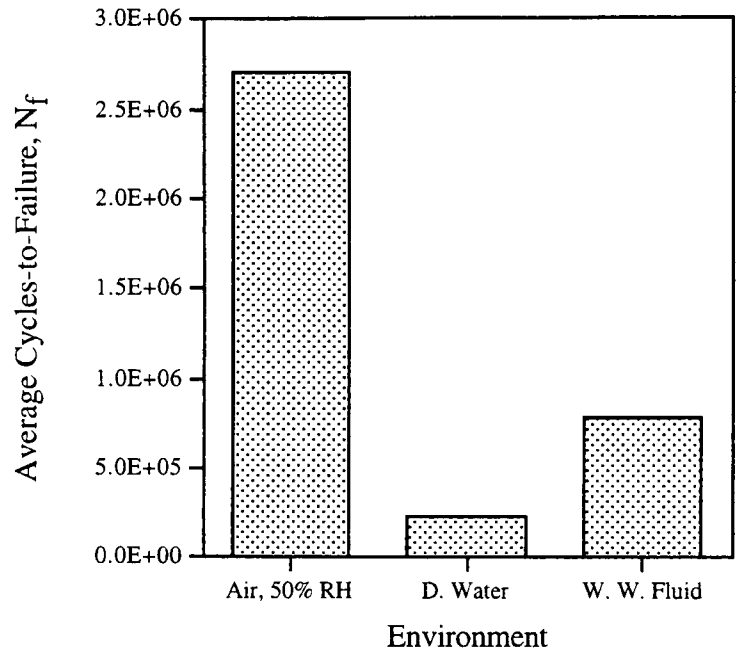


Figure 5-4. Average Cycles-to-Failure, N_f, per Environment

did not have an adverse effect on the glass fibers but managed to decrease the fatigue life of the composite as well. With the minimal opportunities allowed by the fatigue loading to diffuse the composite, plasticization of the matrix by the windshield washer fluid was determined to be the cause.

5.2. Damage Assessment:

5.2.1. Creep:

5.2.1.1. C-Scan Ultrasonics:

As previously mentioned, simple visual comparisons of the pre- and post-test

images showed that the post-test images are slightly darker in appearance. The darkening of the post-test image appeared to be due to an increased attenuation in transmitted sound waves caused by damage sustained during testing. Damage, taking the forms of interfacial debonding and matrix cracking for example, increased surface area, scattering sound waves within the sample. Therefore, the amount of sound that returned to the ultrasonic probe was reduced.

It must be understood, however, that a visual comparison of the pre- and post-test C-scan images is strictly a qualitative evaluation. Additionally, from these visual examinations, damage cannot be directly attributed to either mechanical or environmental causes. Further investigation of the images was required to quantify the damage and identify its probable cause. In order to accomplish this task, mean graylevel measurements with Adobe Photoshop™ were performed on each C-scan image. The mean graylevel for both the pre- and post-test images for each sample was then compared, and the % coefficient of variation was calculated.

As the data in Table 4-3 clearly show, the MG for the samples' entire post-test C-scans was lower than that of the pre-test samples, again implying a greater attenuation in the transmitted sound waves. The increased attenuation is caused by the scattering of the sound waves as they encounter flaws within the material. This supports the visual examination results that the post-test images appear darker than the pre-test images because the lower the graylevel means less sound is being transmitted and received. Likewise, the data in Tables A-1 through A-8 for the selected areas on each sample displayed the same trend. The %CV for these areas showed that the variation in graylevels in the post-test images increased over that of the pre-test images as the area approached the fracture. Figures 5-5 through 5-10 are representations of the pre- and post-test MG and

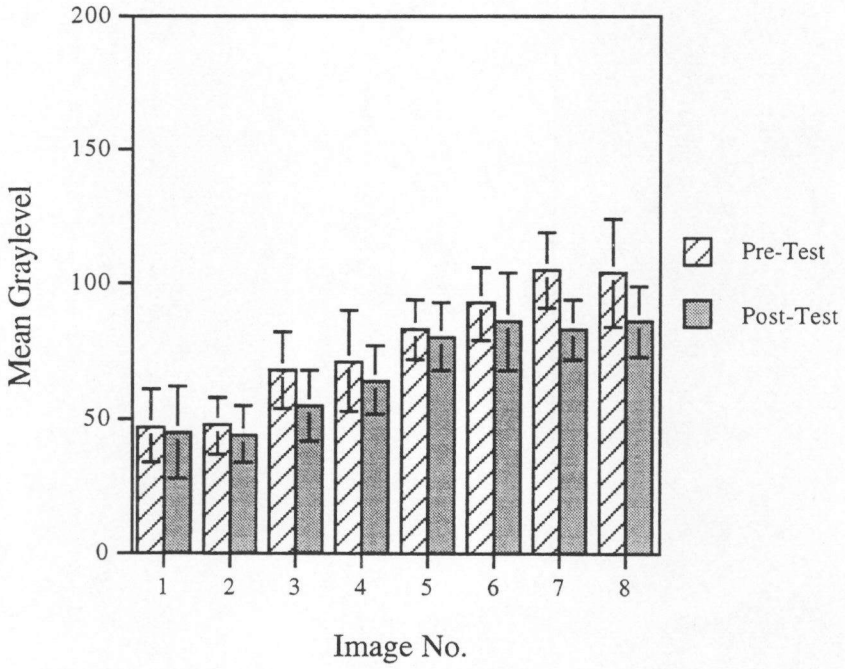


Figure 5-5. C-Scan Mean Graylevel Measurements for Creep Sample P21-0-3 (Air, 50% RH) (No Fracture)

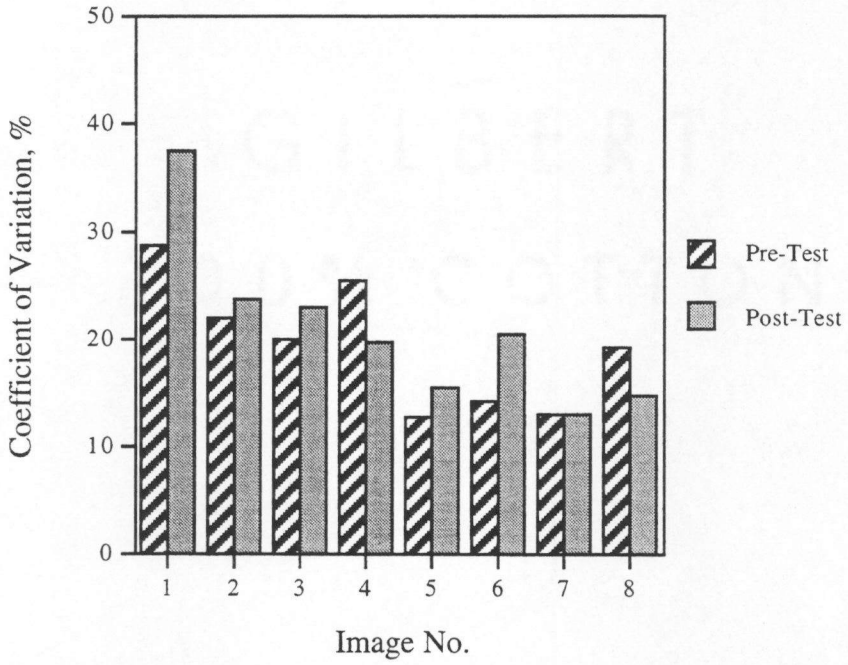


Figure 5-6. C-Scan % Coefficient of Variation for Creep Sample P21-0-3 (Air, 50% RH) (No Fracture)

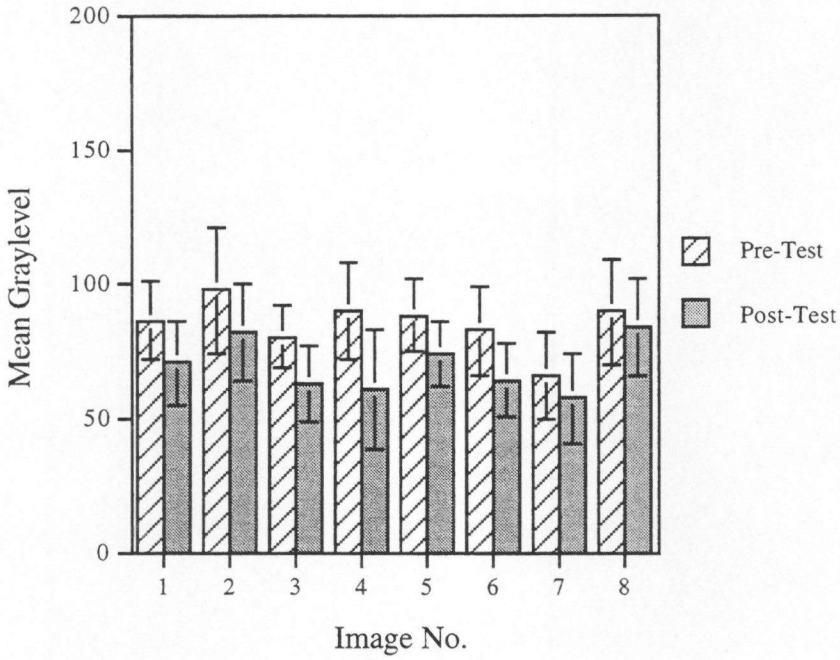


Figure 5-7. C-Scan Mean Graylevel Measurements for

Creep Sample P21-0-22 (Distilled Water)

(Post-Test Image #4 Taken Near Fracture)

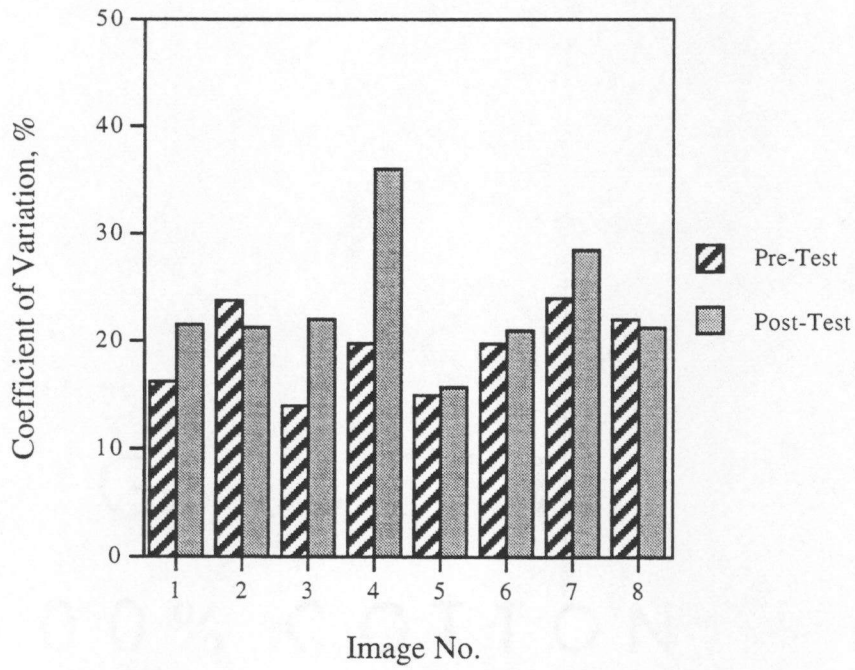


Figure 5-8. C-Scan % Coefficient of Variation for

Creep Sample P21-0-22 (Distilled Water)

(Post-Test Image #4 Taken Near Fracture)

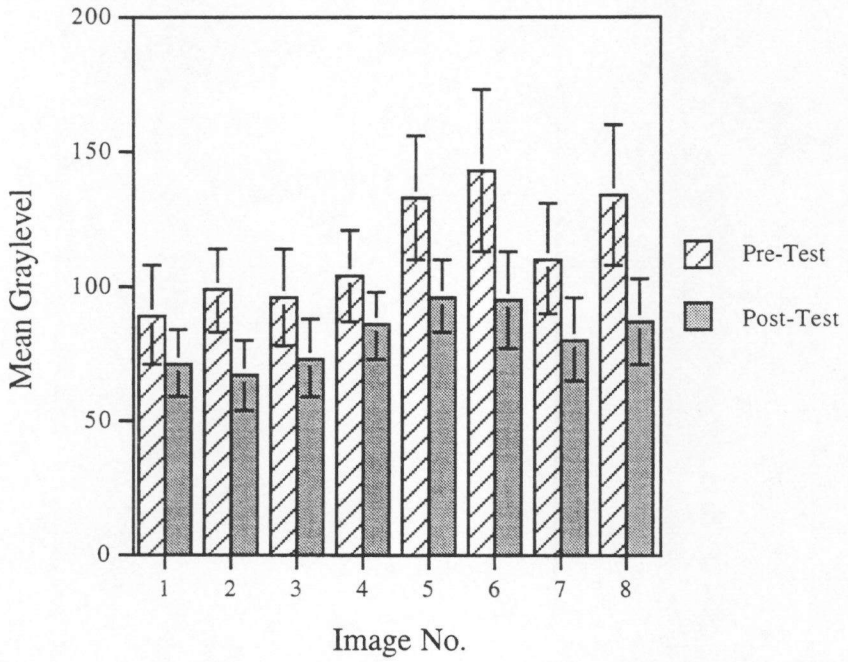


Figure 5-9. C-Scan Mean Graylevel Measurements for Creep Sample P21-0-9 (Windshield Washer Fluid) (Post-Test Image #1 Taken Near Fracture)

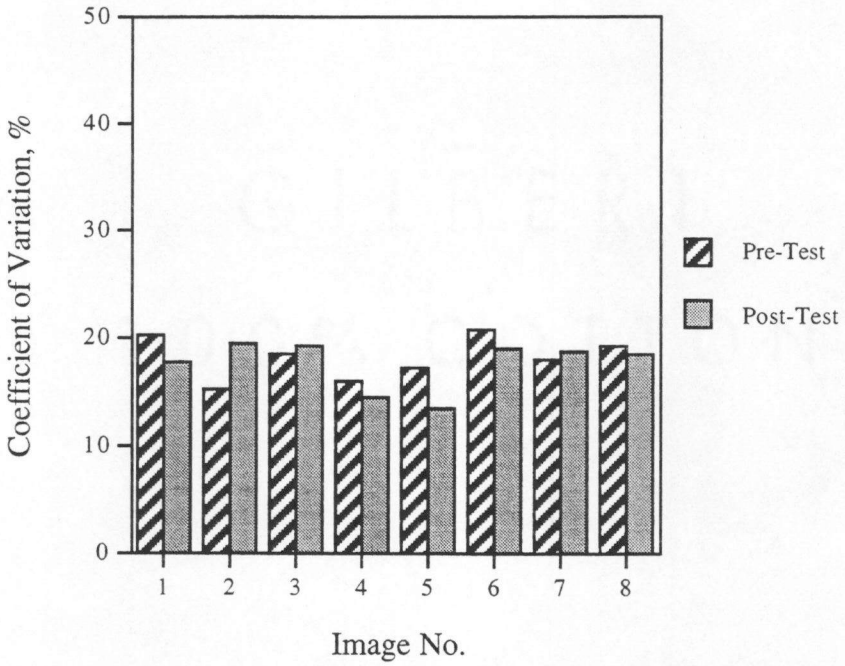


Figure 5-10. C-Scan % Coefficient of Variation for Creep Sample P21-0-9 (Windshield Washer Fluid) (Post-Test Image #1 Taken Near Fracture)

%CV values for selected areas of samples chosen from each environment. Figures 5-5 and 5-6 are the MG and %CV graphs for sample P21-0-3 which was creep tested in air, 50% relative humidity. Figures 5-7 and 5-8 are the MG and %CV graphs for creep sample P21-0-22, tested in distilled water, and Figures 5-9 and 5-10 are those graphs for P21-0-9, tested in windshield washer fluid. These figures graphically illustrate the trend of the MG and %CV values of the post-test images to be lower and greater, respectively, for the creep samples.

Another interesting result of this analysis came from comparing the average change in the MG for each of the environments. Figure 5-11 is a graphical representation of the average change in MG between entire pre- and post-test C-scan images per test environment. Comparison of the different environments showed that windshield washer fluid had the greatest average change in MG. The average change in MG for distilled water, however, appears to be much lower. The average change in MG for those samples tested in air and 50% relative humidity was between the distilled water and windshield washer fluid averages. While it should be noted that none of the samples creep tested in air, 50% relative humidity failed under load, it was shown in Figures 4-10 and 4-11 that microcracks formed on the side of the specimens perpendicular to the load axis. It is proposed that the samples possessed a large amount of such surface microcracks and possibly internal defects that appeared as much darker areas in the post-test C-scan images.

The windshield washer fluid plasticized the polyurethane matrix because the solubilities parameters of the fluid and the polymer are very similar. Therefore, it was also expected that the windshield washer fluid samples would withstand longer creep testing before showing significant changes, which was the observed trend. However, distilled water was anticipated to inflict damage mostly on the E-glass reinforcement at the fiber/matrix interface.(24) The damage incurred in the bulk matrix was more easily

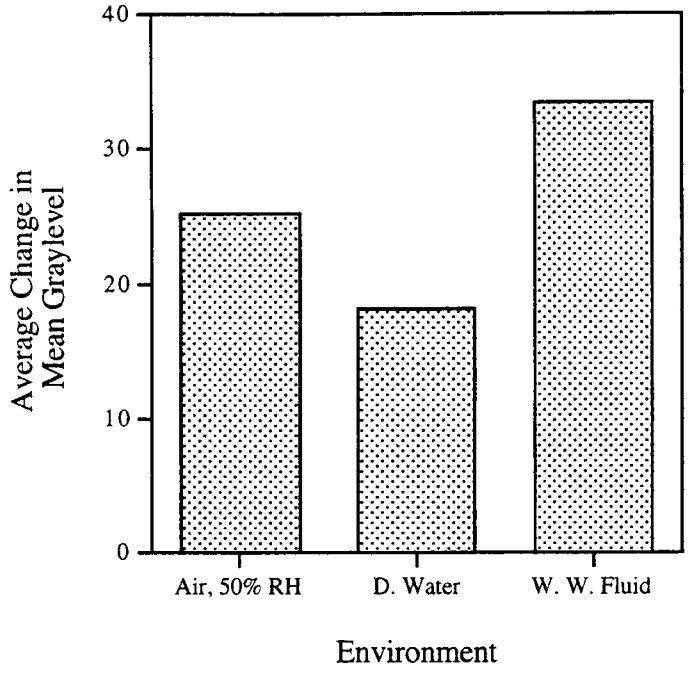


Figure 5-11. Average Change in Mean Graylevel per Environment for Creep Samples

detectable than that which occurs at the fiber/matrix interface, which is illustrated by the average changes in MG per environment.

5.2.1.2. Light-Transmission Microscopy:

The darkening of certain areas in some of the post-test LTM images, as seen in Figures 4-4 through 4-9, was believed to be the result of mechanical damage in the form of fiber/matrix interfacial debonding and possibly some matrix deformation. This was evident by the noticeable distinction in the post-test images of individual fibers where in the pre-test images these same areas had been translucent. Specific areas of interfacial debonding are

marked in these figures with arrows to show the darkening of fiber bundles and individual fiber edges in the post-test images. As the fibers and matrix debond, scattering increases as the surface area that is not directly perpendicular to the transmitted light also increases. Therefore, a greater attenuation of transmitted light occurs, making the post-test image appear darker. This is similar to the attenuation of transmitted sound waves in C-scan ultrasonics, caused by sustained damage. Unfortunately, not every post-test image displayed the same trend of being darker in appearance from the pre-test image. The fact that illumination was not kept constant and that this was a spot analysis on an inhomogeneous composite material were defined as the primary causes. This is not to say that damage did not occur within the CSM material, but that the randomly chosen areas that were examined did not show any damage while other areas that were not examined most likely would have. It must also be stated that some damage, in the form of cracks and interfacial debonds, did not remain open after the applied load was removed. During LTM examination, this type of damage would not necessarily be detectable. Only those cracks or debonds that remained open after loading are identifiable using LTM.

The mean graylevel for each pre- and post-test image was plotted to determine any changes. While some of the plots corroborated the increase in attenuation of transmitted light, already determined by visual examination, some showed no changes or were inconclusive due to inhomogeneity of the CSM composite. Figures 5-12 through 5-17 are selected plots of the MG versus the position of the pre- and post-test images along the centerline down the gage length of each sample (from the Reference Point shown in Figures 3-4 and 3-5) and the corresponding % coefficient of variation. Figures 5-12 and 5-13 are the plots for P21-0-27 which was tested in air and 50% relative humidity. Figure 5-12 showed that there was relatively no change in the MG for the entire sample while Figure 5-13 displayed that the %CV for the post-test images was slightly lower than for the

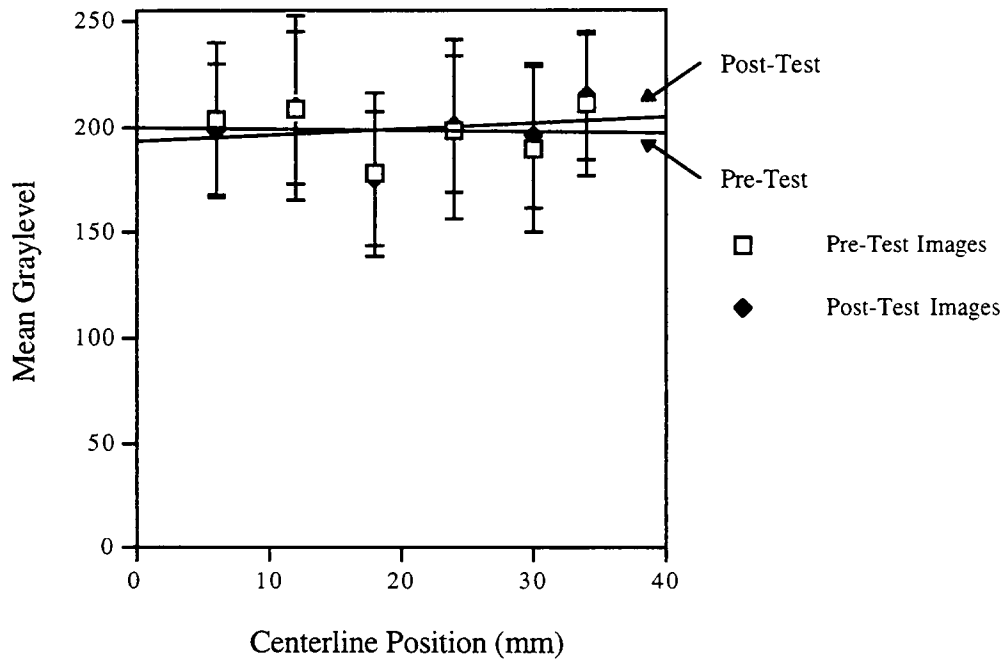


Figure 5-12. LTM Mean Graylevel vs. Centerline Position for Creep Sample P21-0-27 (Air, 50% RH) (No Fracture)

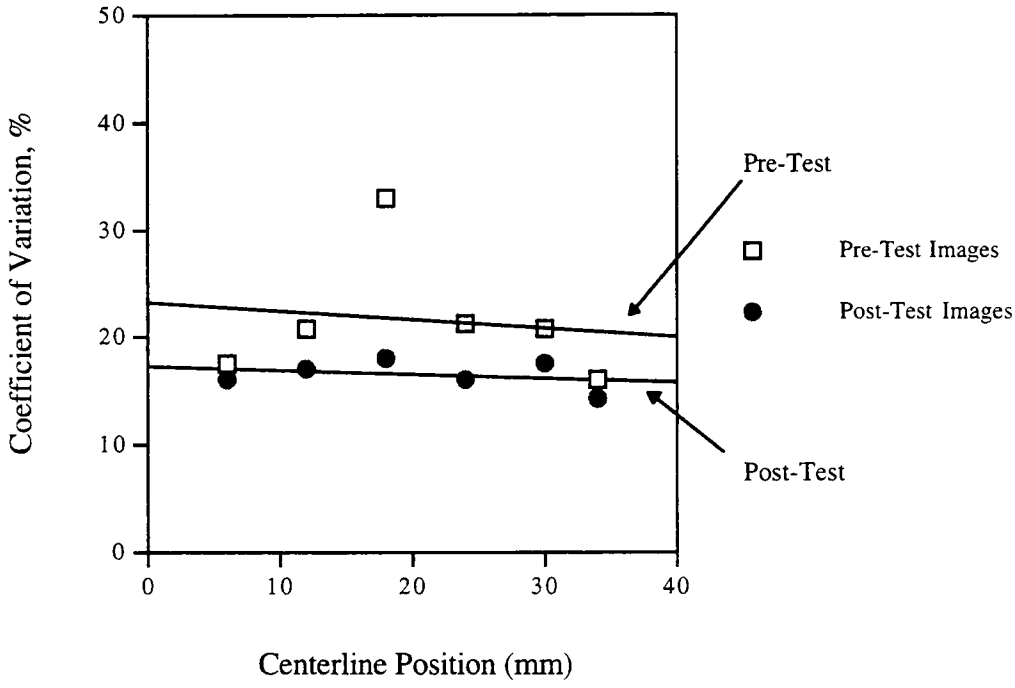


Figure 5-13. LTM % Coefficient of Variation vs. Centerline Position for Creep Sample P21-0-27 (Air, 50% RH) (No Fracture)

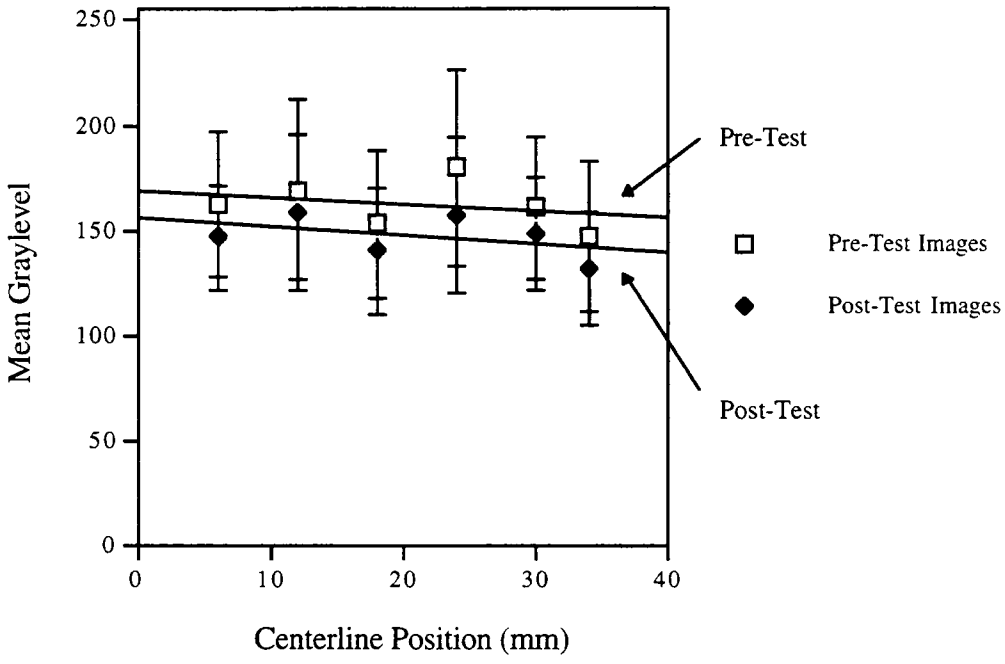


Figure 5-14. LTM Mean Graylevel vs. Centerline Position
for Creep Sample P21-0-10 (Distilled Water)
(Fractured 10.1 cm From Reference Point)

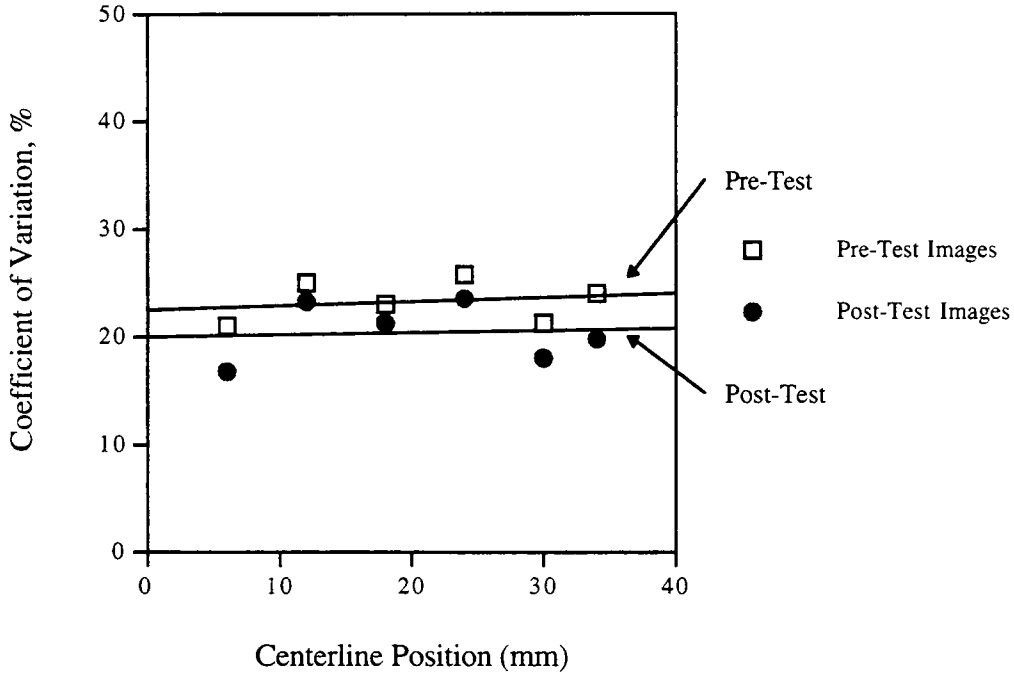


Figure 5-15. LTM % Coefficient of Variation vs. Centerline Position for Creep Sample P21-0-10 (Distilled Water) (Fractured 10.1 cm From Reference Point)

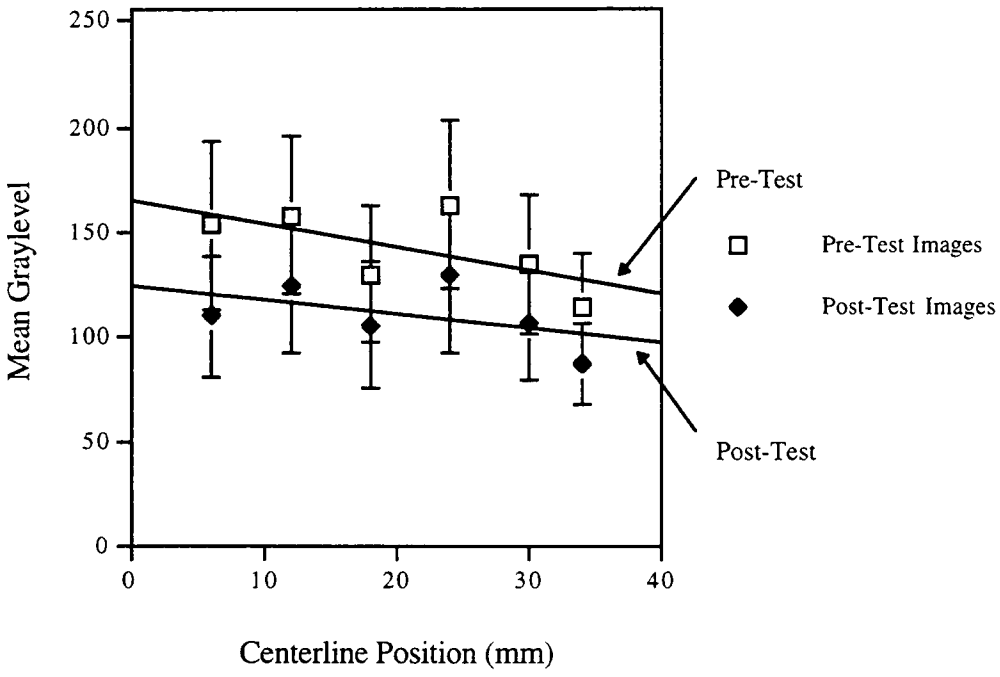


Figure 5-16. LTM Mean Graylevel vs. Centerline Position
for Creep Sample P21-0-7 (Windshield Washer Fluid)
(Fractured 10.8 cm From Reference Point)

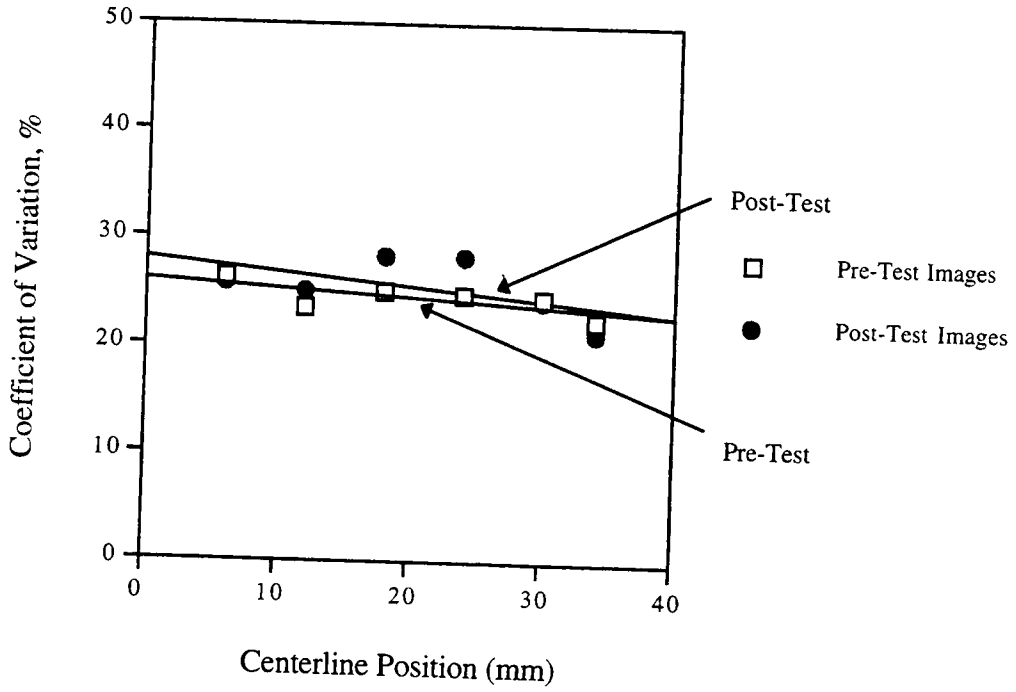


Figure 5-17. LTM % Coefficient of Variation vs. Centerline Position for Creep Sample P21-0-7 (Windshield Washer Fluid) (Fractured 10.8 cm From Reference Point)

pre-test images. Again, inconsistent illumination and spot analysis were determined to be the causes for this. Figures 5-14 and 5-15, the MG and %CV plots for P21-0-10 which was tested in distilled water, demonstrated small changes over the entire sample but not to any significant degree. The plots for P21-0-7, tested in windshield washer fluid, appear in Figures 5-16 and 5-17. They showed slightly more change than in the previous two figures but still not significantly so.

5.2.1.3. Scanning Electron Microscopy:

Visual comparison of the SEM images for the distilled water and windshield washer fluid creep samples revealed some interesting trends. As shown in Figures 4-12 through 4-14 and 4-16 through 4-18, the samples that were exposed to distilled water showed a greater frequency in the appearance of river patterns and brittle fracture bands when compared to the windshield washer fluid samples. Because distilled water inflicts damage mostly on the E-glass at the fiber/matrix interface and does not generally affect the bulk matrix, the distilled water samples were expected to show typical brittle fracture characteristics. The windshield washer fluid samples did indeed display brittle fracture characteristics as well because the CSM samples are still brittle material. However, the lesser commonality of these characteristics indicates that the windshield washer fluid plasticized the matrix, making the matrix more flexible. The plasticizing effect of the windshield washer fluid may have caused certain spots in the bulk matrix to behave in a more homogeneous manner than heterogeneous, thus reducing the appearance of river patterns. Moreover, as shown in Figure 4-12, the exposed fibers on the distilled water samples' fracture surfaces were clean while bits of matrix material still clung to those on the fracture surfaces of the windshield washer fluid specimens, as seen in Figure 4-15. Again, distilled water's attack at the interface was determined to be the cause. Since windshield

washer fluid does not affect the fiber/matrix interface, the clinging of matrix to the fibers is evidence of good interfacial adhesion.

5.2.2. Fatigue:

5.2.2.1. C-Scan Ultrasonics:

As noted earlier, visual comparison of the pre- and post-test images demonstrated a slight darkening in the post-test images. Likewise, increased attenuation in transmitted sound waves, caused by damage sustained during testing, was decided to be the cause of the darkening. As in the case of the creep samples, increased surface area within the samples, due mostly to fiber/matrix interfacial debonding, was considered responsible for the scattering of sound waves.

Moving beyond the simple visual examination to the assessment of damage based on environmental and mechanical causes, each C-scan image was analyzed to obtain the mean graylevel values. As shown by the data in Table 4-5, the MG for the post-test C-scans was lower than that of the pre-test, as was also observed for the creep samples. Again, this indicates a greater attenuation in the transmitted sound waves, bolstered by the visual comparison of the pre- and post-test images. Moreover, a similar trend was seen in the data in Tables A-9 through A-17 for the selected areas on each sample. As the selected areas in the post-test images approached the fracture surface, the %CV increased significantly over that of the pre-test images. Figures 5-18 through 5-23 are graphical representations of the pre- and post-test MG and %CV values for selected areas of samples chosen from each environment. Figures 5-18 and 5-19 are the MG and %CV graphs for sample P21-0-11 which was fatigued in air, 50% relative humidity. Figures 5-20 and 5-21 are the MG and %CV graphs for distilled water fatigue sample P21-0-19, and the values

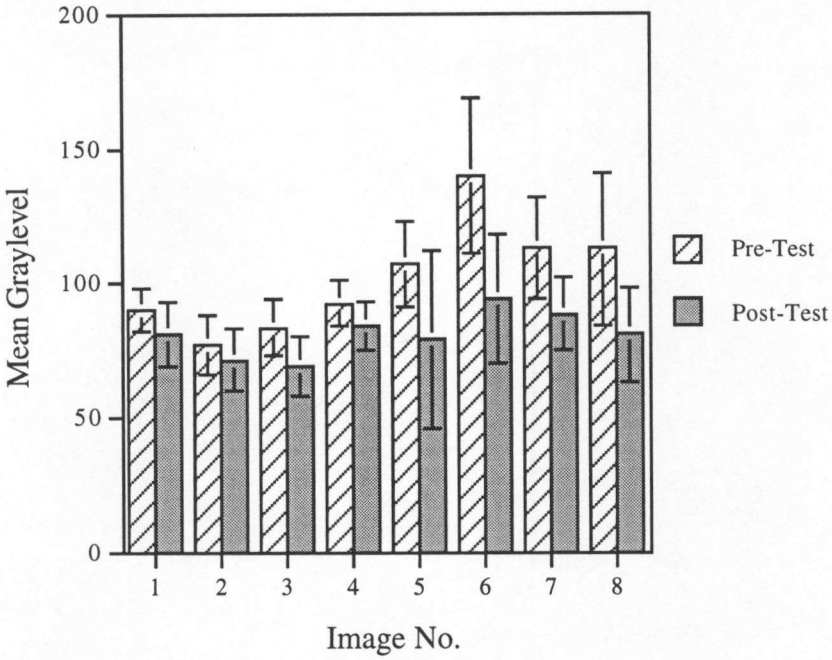


Figure 5-18. C-Scan Mean Graylevel Measurements for Fatigue Sample P21-0-11 (Air, 50% RH) (Post-Test Image #5 Taken Near Fracture)

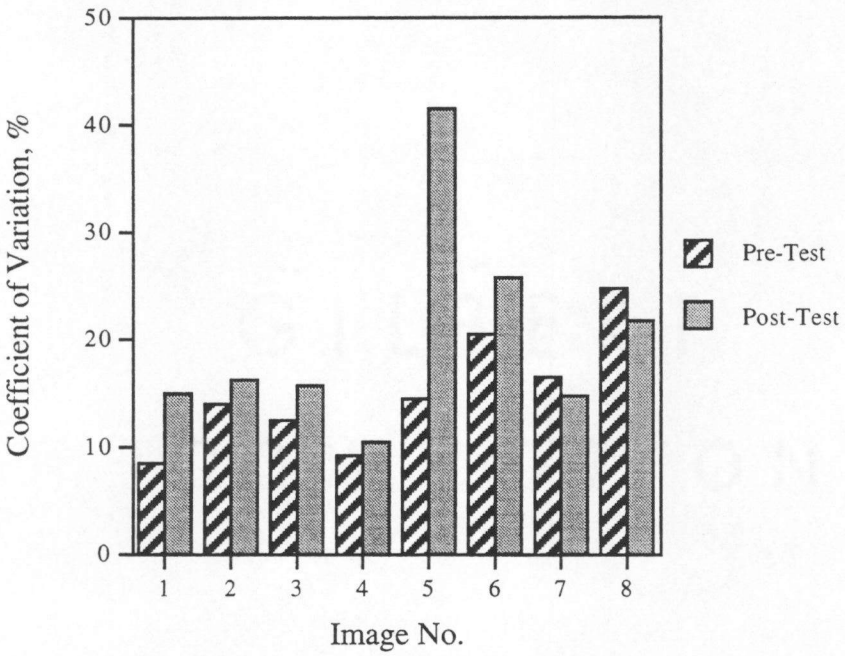


Figure 5-19. C-Scan % Coefficient of Variation for
Fatigue Sample P21-0-11 (Air, 50% RH)
(Post-Test Image #5 Taken Near Fracture)

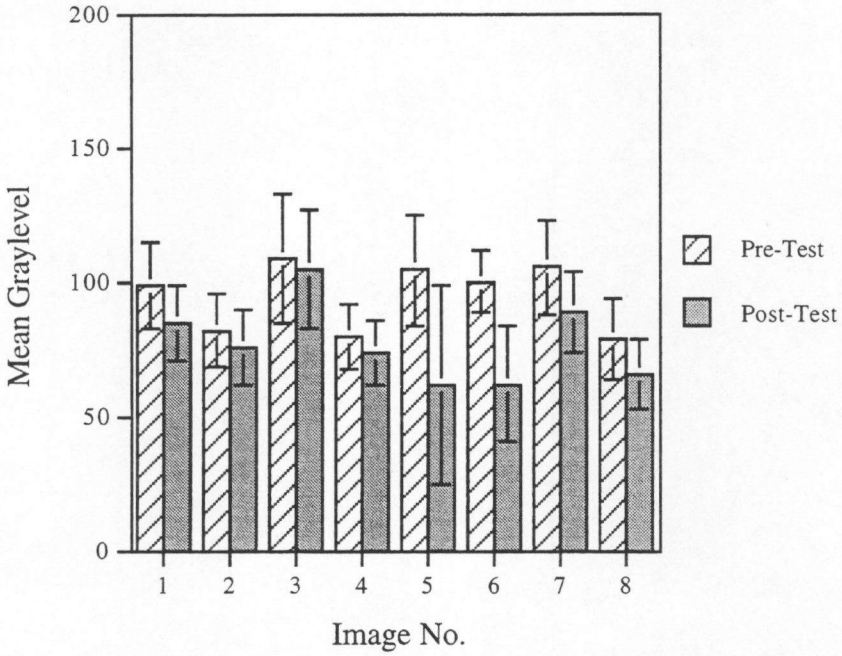


Figure 5-20. C-Scan Mean Graylevel Measurements for Fatigue Sample P21-0-19 (Distilled Water) (Post-Test Image #5 Taken Near Fracture)

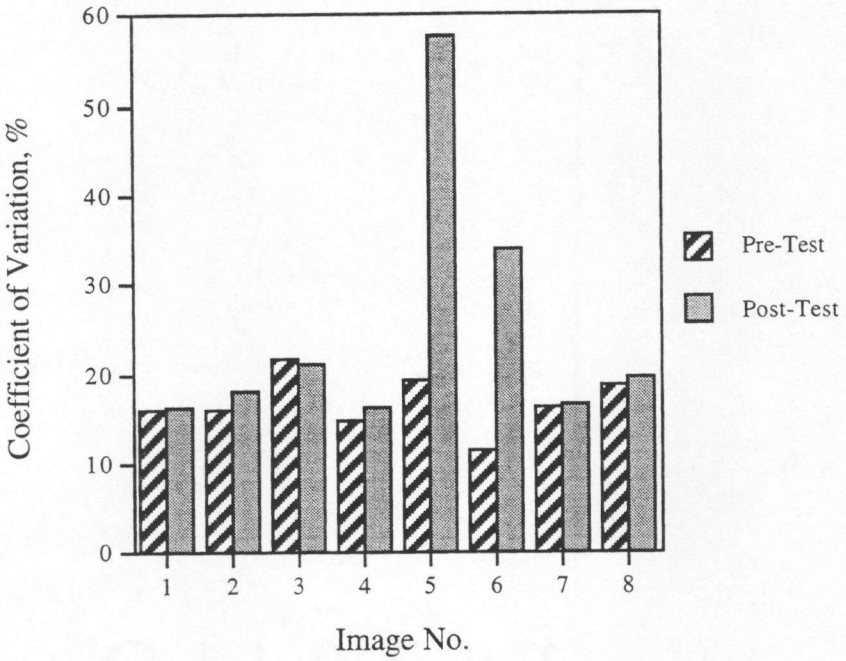


Figure 5-21. C-Scan % Coefficient of Variation for
Fatigue Sample P21-0-19 (Distilled Water)
(Post-Test Image #5 Taken Near Fracture)

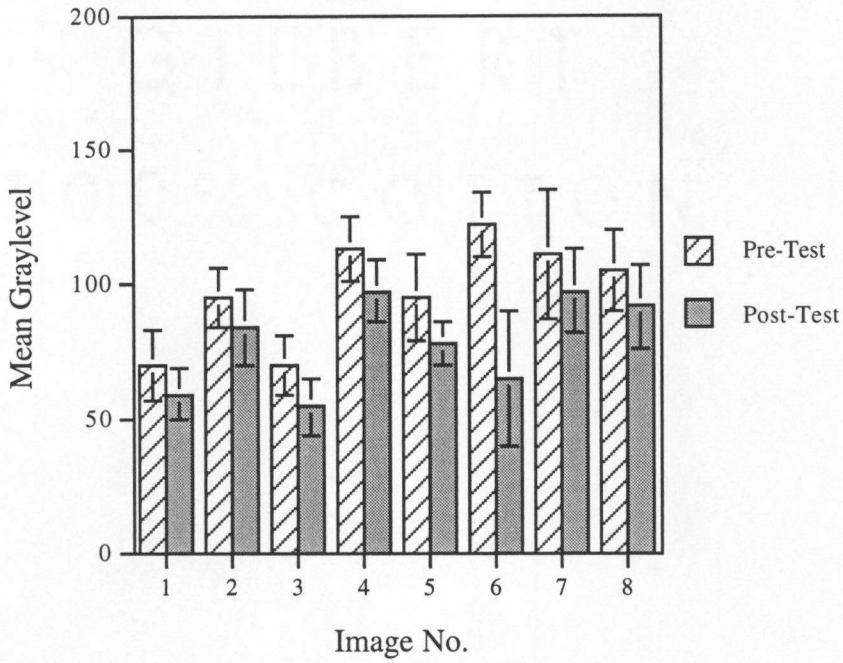


Figure 5-22. C-Scan Mean Graylevel Measurements for Fatigue Sample P21-0-18 (Windshield Washer Fluid) (Post-Test Image #6 Taken Near Fracture)

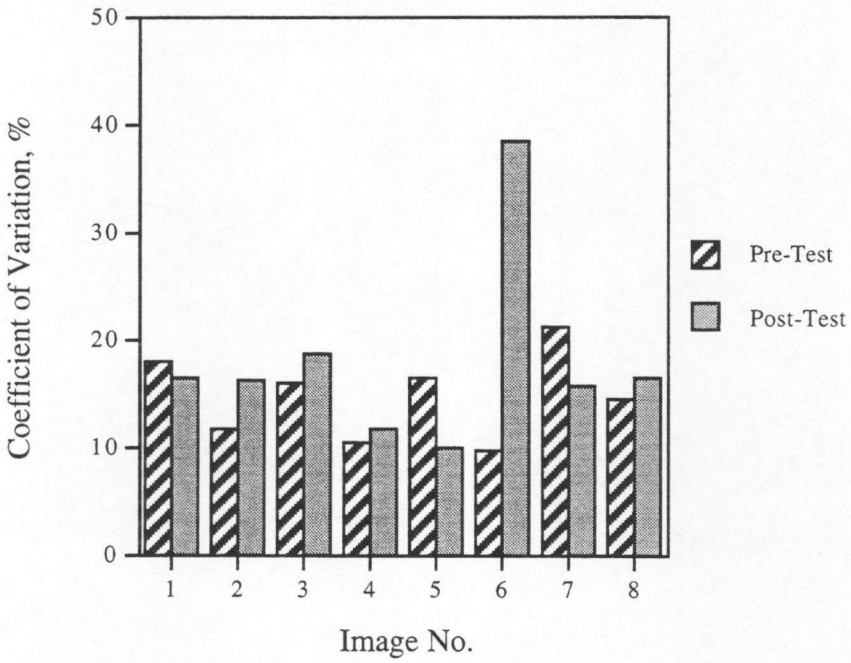


Figure 5-23. C-Scan % Coefficient of Variation for Fatigue Sample P21-0-18 (Windshield Washer Fluid) (Post-Test Image #6 Taken Near Fracture)

for sample P21-0-18, fatigued in windshield washer fluid, are represented in Figures 5-22 and 5-23. These figures portray the trend of the MG and %CV values of the post-test images to be lower and greater, respectively, for the fatigue samples.

Comparison of the average change in MG for the fatigue samples per environments was made. The graphical representation of this comparison appears in Figure 5-24. Upon comparing the different environments, the distilled water samples showed the greatest average change in MG while the windshield washer fluid samples were only slightly greater than the air, 50% relative humidity samples. During fatigue, the repeated extension and compression of the sample allows the ingress of the liquid environments into microcracks by capillary action.(25) This capillary action creates the opportunity for the environments to further diffuse the bulk matrix and attack the fiber/matrix interface. Distilled water does not affect the polyurethane matrix because it cannot plasticize it. However, as interfacial debonding increases with the dynamic loading, the distilled water adversely affects the glass fiber reinforcement by attacking at the interface, causing greater changes in the distilled water samples. Windshield washer fluid affected the matrix only by plasicization and left the glass fibers undisturbed. Since plasticization of the matrix decreases the material's stiffness, the windshield washer fluid samples endured more fatigue without incurring significant change.

5.2.2.2. Light-Transmission Microscopy:

As was also noticed in the creep LTM images, mechanical damage in the form of fiber/matrix interfacial debonding was determined to be responsible for the darkening of certain areas in some of the post-test images. From visual examination of the fatigue LTM images in Figures 4-13 through 4-18, the noticeable distinction of individual fibers was clearly evident in the post-test images. These same areas had previously been transparent

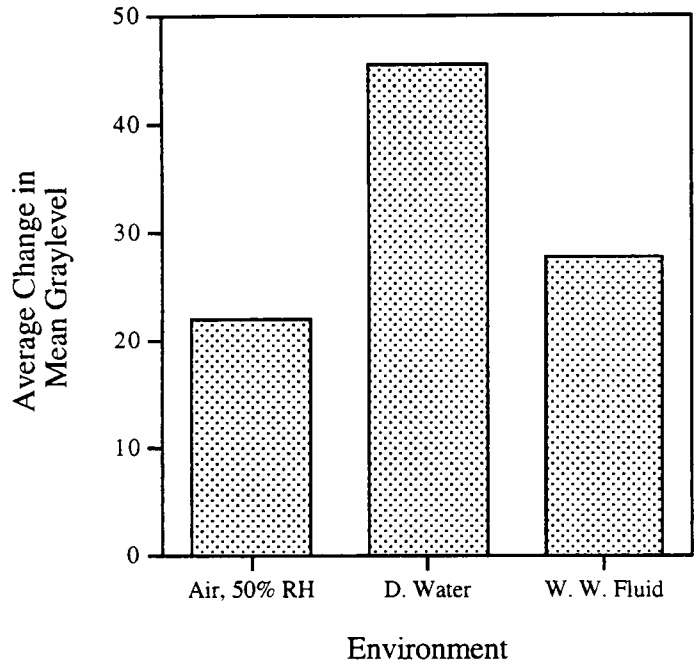


Figure 5-24. Average Change in Mean Graylevel per Environment for Fatigue Samples

in the pre-test images. Increased surface area created by fibers and matrix debonding during fatigue loading increasingly scattered the transmitted light, darkening the post-test image. There seemed to be a greater appearance of individual fibers in some post-test fatigue images over that which was seen in the creep samples, regardless of environment. This was discerned to be the result of the nature of the mechanical testing. Fatigue, being a dynamic loading, appeared to have caused a greater amount of debonding than creep, which is static loading. As seen with the creep LTM images, not all of the post-test images exhibited the trend of appearing darker than the pre-test images. Again, inconsistent illumination and spot analysis were deemed to be the chief causes.

To determine any changes, plots of the mean graylevel and % coefficient of variation for each pre- and post-test images were made. Again, some of the MG plots supported the observed trend in the darkening of the post-test images due to increased attenuation of transmitted light. However, as seen with the creep LTM images, the inhomogeneity of the composite caused some plots to show no changes. Figures 5-25 through 5-30 are selected plots of the MG and %CV versus the position of the pre- and post-test images along the centerline down the gage length of each sample. Figures 5-25 and 5-26 are the MG and %CV plots for P21-0-11, tested in air and 50% relative humidity, showing no significant change in MG. As previously explained, the inhomogeneity of the composite material was determined to be reason for this. Figures 5-27 and 5-28, the MG and %CV plots for P21-0-26 tested in distilled water, demonstrated small changes over the entire sample but as in the case of sample P21-0-11 not to any significant degree. Figures 5-29 and 5-30 are the MG and %CV plots for P21-0-17, which was tested in windshield washer fluid. It showed similar changes to the sample tested in distilled water, but the changes were still considered relatively small. The %CV trend for P21-0-17, which fractured in the ninth LTM image, does show a greater tendency to increase as the images approach the fracture surface. As stated earlier, after the applied load was removed, microcracks and interfacial debonds did not remain open. LTM examination was only able to detect those cracks or debonds that remained open after loading. Hence, only small changes were seen. Additionally, the inhomogeneous nature of the CSM composite and inconsistent illumination meant that some plots may have shown small changes but others did not.

5.2.2.3. Scanning Electron Microscopy:

Visual comparison of the SEM images of the fatigue samples for each of the

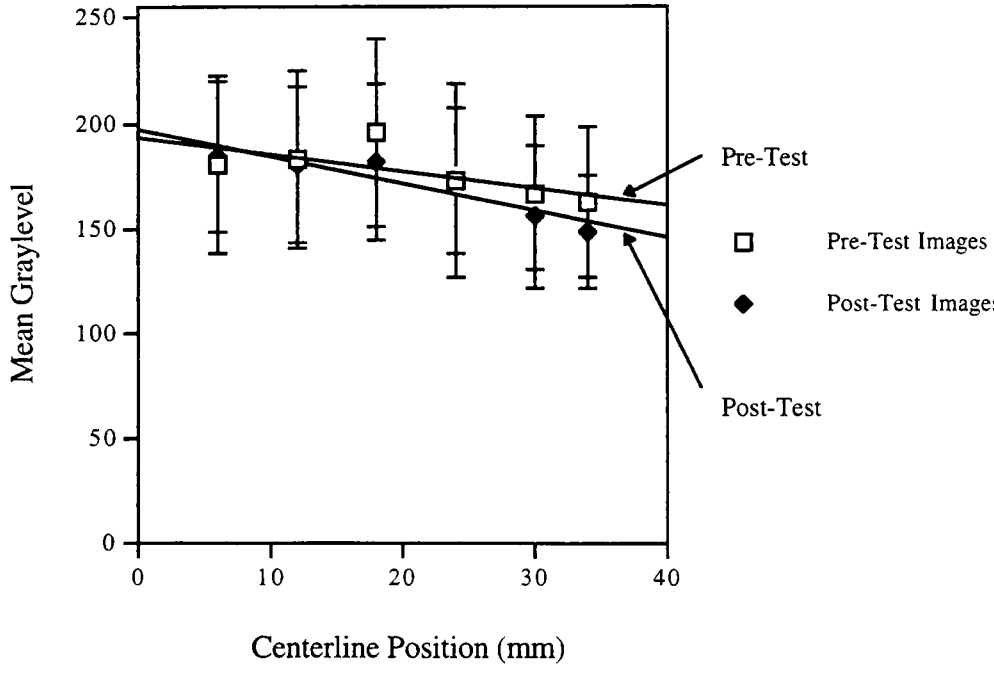


Figure 5-25. LTM Mean Graylevel vs. Centerline Position
for Fatigue Sample P21-0-11 (Air, 50% RH)
(Fractured 3.6 cm From Reference Point)

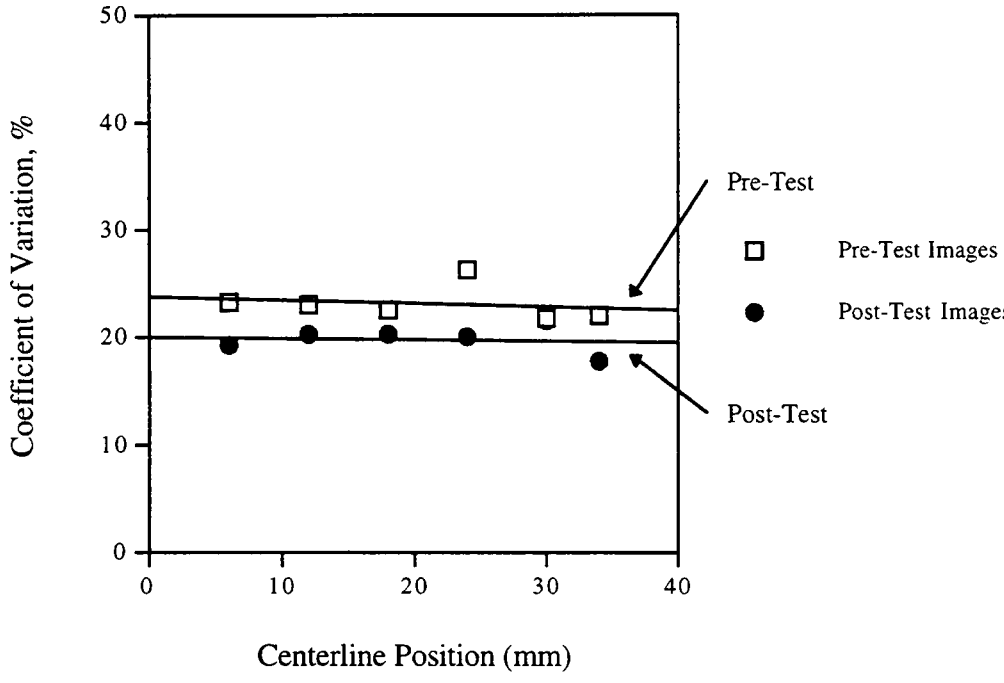


Figure 5-26. LTM % Coefficient of Variation vs. Centerline Position for Fatigue Sample P21-0-11 (Air, 50% RH) (Fractured 3.6 cm From Reference Point)

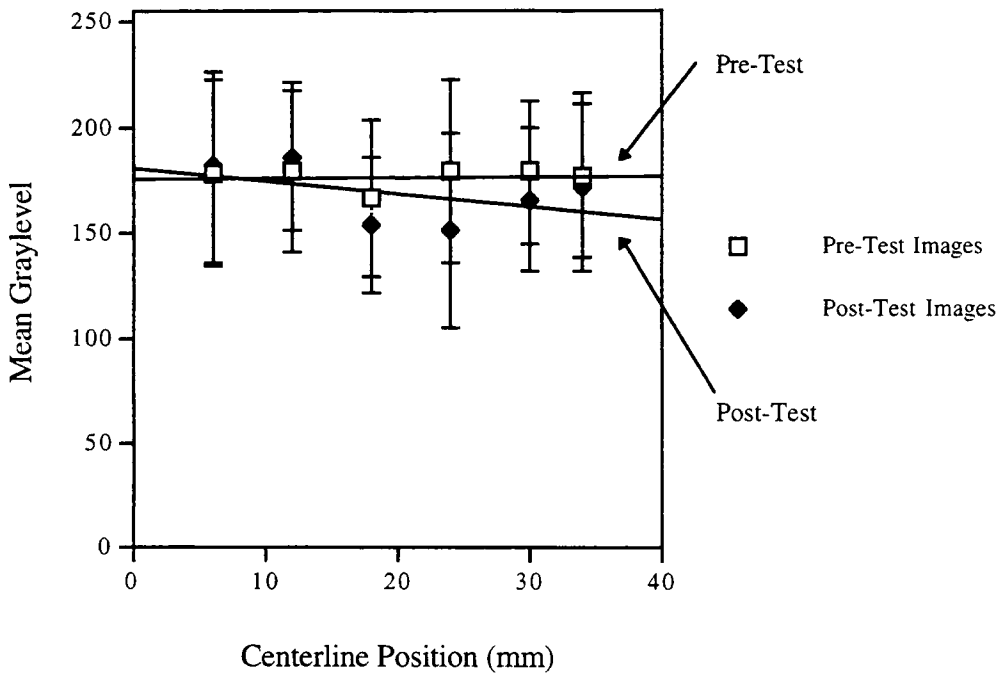


Figure 5-27. LTM Mean Graylevel vs. Centerline Position
for Fatigue Sample P21-0-26 (Distilled Water)
(Fractured 4.2 cm From Reference Point)

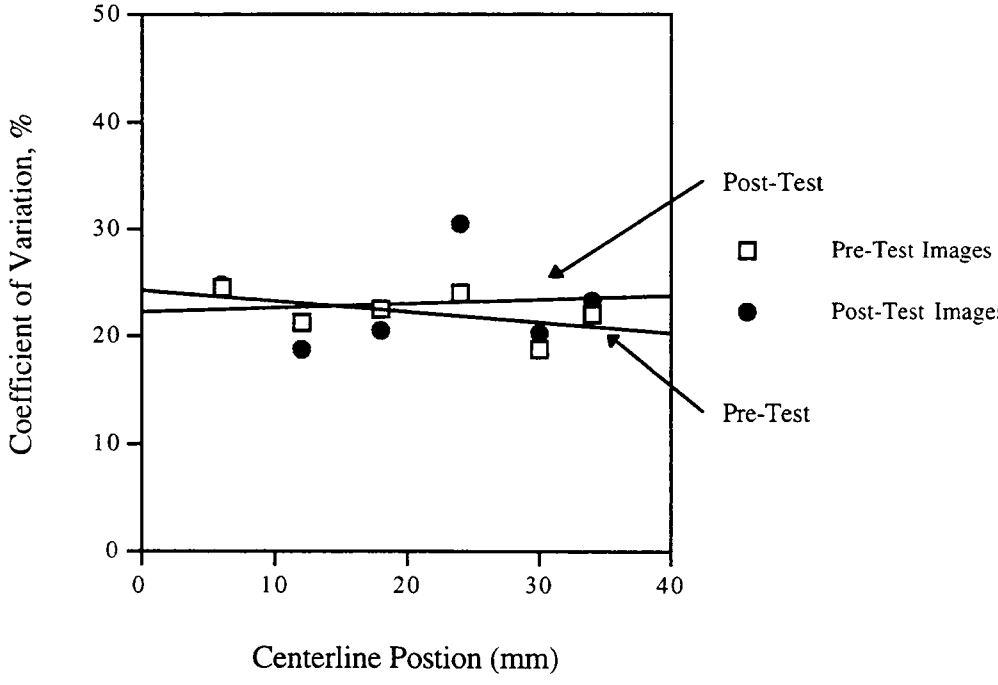


Figure 5-28. LTM % Coefficient of Variation vs. Centerline Position for Fatigue Sample P21-0-26 (Distilled Water) (Fractured 4.2 cm From Reference Point)

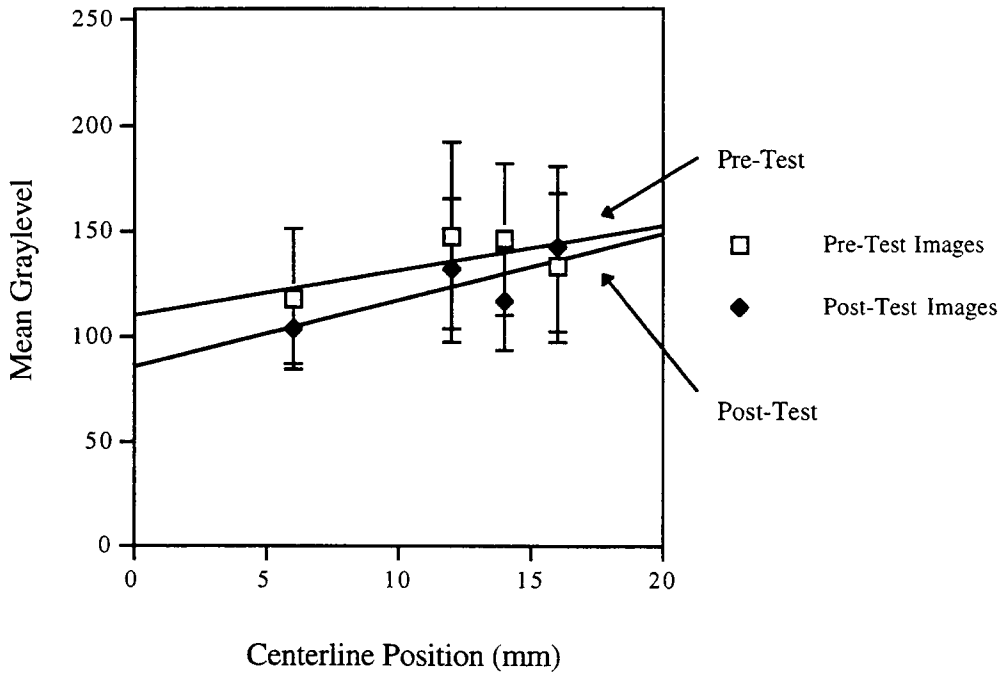


Figure 5-29. LTM Mean Graylevel vs. Centerline Position
for Fatigue Sample P21-0-17 (Windshield Washer Fluid)
(Fractured 1.7 cm From Reference Point)

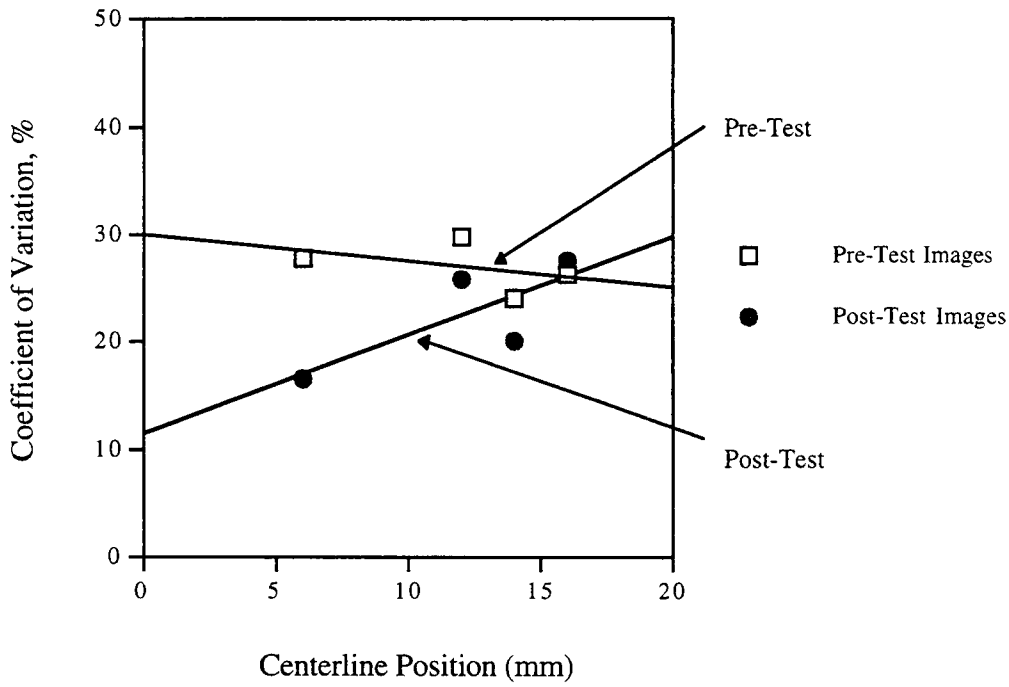


Figure 5-30. LTM % Coefficient of Variation vs. Centerline Position for Fatigue Sample P21-0-17 (Windshield Washer Fluid) (Fractured 1.7 cm From Reference Point)

environments showed trends similar to those seen in the creep samples. As shown in Figures 4-28 and 4-29, those samples that were fatigued in air, 50% relative humidity displayed the attributes expected from brittle fracture, namely river patterns and brittle fracture bands. There also appeared to be relatively good adhesion between the fibers and the matrix across the fracture surfaces. As was the case with creep, the fatigue samples that were exposed to distilled water showed a greater occurrence of river patterns and brittle fracture bands than the windshield washer fluid samples, shown in Figures 4-30 through 4-37. Fiber/matrix interfacial debonding as a result of the exposure to the distilled water was obvious as the fibers appeared clean, as seen in Figure 4-33. The windshield washer fluid samples also showed some brittle fracture characteristics but, as expected, with less frequency due to the plasticization of the matrix by the windshield washer fluid. Matrix debris was shown to be still clinging to the fibers on the fracture surfaces of the windshield washer fluid samples. Again, because windshield washer fluid does not attack the interface, the presence of matrix debris on the fibers testifies to good fiber/matrix interfacial adhesion.

A mechanism for the failure of the CSM composite material under mechanical loading has been proposed and is shown in Figure 5-31.(14) The regions represent the fiber orientation with regard to the loading direction, not unlike that shown in Figure 2-1. Region A represents the fibers that are parallel to the load axis, Region B shows fibers that lie perpendicular to the load axis, and Region C displays those fibers that are oriented roughly 45° with respect to the load axis. As was described previously in Section 2.1, the mechanical properties of a composite depend on the fiber orientation, as does the failure of the composite. The proposed mechanism of failure suggests that the initiation of fracture under tensile loading occurs in one of four ways. A crack may be initiated in the matrix by

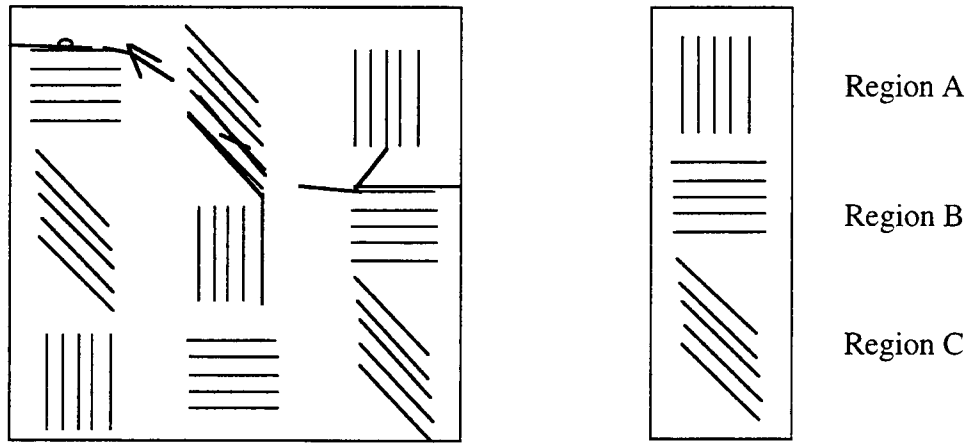


Figure 5-31. Schematic of Proposed Mechanism of Failure for the CSM Composite (14)

surface and bulk defects, fiber/matrix debonding, fiber/fiber debonding, or by fiber breakage. Under uniaxial tensile loading, the initial crack propagates until it comes in contact with a fiber/matrix interface, which it will follow until fracture is complete.(14) From examination of Figures 4-38 through 4-41, it was clear that the propagation of failure in the CSM composite samples followed this proposed mechanism of failure.

VI. CONCLUSIONS

In this study, samples of a continuous swirl glass mat (CSM) polyurethane composite were creep and fatigue tested in different environments, and the damage sustained was assessed using nondestructive test methods. The samples were creep or fatigue tested in air, 50% relative humidity, distilled water, or windshield washer fluid and then examined by C-scan ultrasonics, Light-Transmission Microscopy (LTM), and Scanning Electron Microscopy (SEM). Comparisons were made of the mechanical properties for both creep and fatigue samples. Likewise, the pre- and post-test results of C-scan ultrasonic and LTM images and the SEM images of the fracture surfaces per environment were also compared. Based on the results obtained from this research, the following conclusions were reached.

1. Comparison of the average creep strain per environment for the creep samples revealed that the windshield washer fluid had the greatest effect. A study of the solubility parameters of the liquid environments supported this conclusion by showing that the windshield washer fluid was expected to plasticize the matrix, increasing its flexibility.

2. Comparison of the average cycles-to-failure per environment for the fatigue samples showed that the distilled water significantly decreased the fatigue life of the CSM composite. Since distilled water is known to attack E-glass fiber reinforcements, this reduction in fatigue life was determined to be the result of damage inflicted at the fiber/matrix interface.

3. Visual examination and mean graylevel measurements of pre- and post-test C-scan ultrasonic images for both creep and fatigue samples showed that the post-test images appeared darker than the pre-test images, implying a greater attenuation of transmitted sound waves due to increased scatter. The increase in scatter was determined to be the result of damage within the samples caused by microcracking of the matrix and/or fiber/matrix interfacial debonding. The MG and % coefficient of variation of selected areas on the pre- and post-test C-scans showed the tendency to decrease and increase, respectively, as the area approached the fracture surface. Comparison of the average change in MG per environment revealed for creep samples that, due to plasticization of the matrix, the windshield washer fluid samples were able to creep for a longer period before sustaining damage, mostly in the bulk matrix. In the case of fatigue, however, distilled water showed a larger amount of damage, resulting from the water's attack on the E-glass fibers at the interface.

4. Visual examination of pre- and post-test LTM images for both creep and fatigue specimens showed that regardless of environment, darkened areas in the post-test images could be identified as damage, mostly in the form of fiber/matrix interfacial debonding. This was evident by the distinct outline of individual fibers in the post-test images that were formerly translucent in the pre-test images. Mean graylevel and % coefficient of variations measurements of these same images demonstrated that there were some changes incurred in the samples during testing but not to any significant degree. This was due in large part to the fact that illumination was not kept

constant. Also that this technique was a spot analysis of an inhomgeneous material was determined to be a possible cause.

5. Examination of the fracture surfaces of the creep and fatigue samples, using SEM, showed that the distilled water samples displayed more brittle fracture characteristics than the windshield washer fluid samples, regardless of the means of mechanical testing. The increased flexibility in the windshield washer fluid samples, brought on by plasticization of the polyurethane matrix, was postulated to be the cause. The air, 50% relative humidity samples displayed typical brittle fracture features but not to any extraordinary degree. Additionally, the distilled water samples showed clean fibers on the fracture surface, indicative of interfacial attack on the E-glass reinforcement. By comparison, the windshield washer fluid and air, 50% relative humidity samples showed good fiber/matrix interfacial bonding, as fibers were seen with matrix still clinging to them after failure.

6. Examination of SEM images of a randomly selected sample of the CSM composite clearly demonstrated the proposed mechanism of failure.

VII. RECOMMENDATIONS

Based on the results presented in this thesis, future research should include:

1. The technique of LTM should be modified to allow continuous scanning of the composite samples. Additionally, more sophisticated lenses should be employed to allow greater depth-of-focus within the composite.

2. The use of Infrared Thermography as another method nondestructive evaluation should be considered as a means of pinpointing thermal activity, associated with damage, during mechanical testing. This may allow the isolating of specific areas in which to search for damage.

3. Fourier Transform Infrared Spectroscopy (FT-IR) should be employed to determine any changes in the matrix as the result of environmental exposure.

LIST OF REFERENCES

LIST OF REFERENCES

1. Kau, C. A. Hiltner, E. Baer and L. Huber. *J. Reinforced Plastics and Composites,* 8:18 (1989).

2. Nakamura, M., T. Chiba and I. Matsumure. *Polyurethanes World Congress 1991*, (Sept. 24-26, 1991).

3. Wharfield, R. D. *Polyurethanes World Congress 1991*, (Sept. 24-26, 1991).

4. Karger-Kocsis, J. and T. Czigany. *J. Materials Science*, 28:2440 (1993).

5. Corum, J. M. "Durability of Lightweight Composite Structures for Automotive Applications: Annual Progress Report for Period Ending September 30, 1995", Oak Ridge National Laboratory (Mar. 1996).

6. Young, R. J. and P. A. Lovell. Introduction to Polymers, 2nd ed., Chapman Hall, 413, 416 (1991).

7. Tonyali, K., C. E. Rogers, and H. R. Brown. *Polymer*, v. 28, 1472-1477 (Aug. 1987).

8. Schwartz, M. M. Composite Materials Handbook, McGraw-Hill, 2.35, 1.10-15, 2.29 (1984).

9. Karger-Kocsis, J. and Zs. Fejes-Kozma. *Mechanics of Composite Materials*, v. 30, no. 1, 8-13 (1994).

10. Karger-Kocsis, J. *Journal of Applied Polymer Science*, v. 45, 1595-1609 (1992).

11. Fejes-Kozma, Zs. and J. Karger-Kocsis. *Journal of Reinforced Plastics and Composites*, v. 13, 823-834 (1994).

12. Czigany, T. and J. Karger-Kocsis. *Polymer & Polymer Composites*, v. 1, no. 5, 329-339 (1993).

13. Karger-Kocsis, J. *Journal of Materials Science Letters*, v. 13, 1422-1425 (1994).

14. Corum, J. M. "Durability of Lightweight Composite Structures for Automotive Applications: Annual Progress Report for Period Ending September 30, 1996", Oak Ridge National Laboratory, 1-30, 1-31 (Jan. 1997).

15. Engel, L., H. Klingele, G. W. Ehrenstein, and H. Schaper. An Atlas of Polymer Damage, Wolfe Publishing, 114, 190, 226, 193, 230, 177, 188 (1981).

16. Moiseev, Y. V. and G. E. Zaikov, Chemical Resistance of Polymers in Aggressive Media, Consultants Bureau, 281-282, 284-287, 300-301, 308, 320-321 (1987).

17. Anders, O. U. *SAMPE Technical Conference*, v. 23, 1084-1087 (Oct. 21-24, 1991).

18. Huang, X. and R. R. Bresee. *INDA J. Nonwovens Research*, v. 5, no. 1-3; v. 6, no. 4 (1993, 1994).

19. Bradley, G. F., Jr. "Electron Beam Charging of Polymers in a Scanning Electron Microscope" Master's Thesis, The University of Tennessee, Knoxville, TN, 12 (1992).

20. Goldstein, J. I., et al. Scanning Electron Microscopy and X-Ray Microanalysis, Plenum Press, 91 (1992).

21. Personal Correspondence with Dr. W. A. Simpson, Jr., Oak Ridge National Laboratory, 1997.

21. Personal Correspondence with Dr. J. M. Corum, Oak Ridge National Laboratory, 1997.

22. Personal Correspondence with Dr. H. E. McCoy, Jr., Oak Ridge National Laboratory, 1997.

23. Barton, A. F. M. CRC Handbook of Solubility Parameters and Other Cohesion Parameters, CRC Press, 254-257 (1991).

24. Engineered Materials Handbook, Vol. 1 Composites, ASM International, 45-48 (1987).

25. Smith, L. V. and Y. J. Weitsman. "Sea Water Effects on the Fatigue Response of Polymeric Composites" in *Progress in Durability Analysis of Composite Systems*, Proceedings of the International Conference DuraCoSys 95, Belgium (July 1995).

26. Berry, J. P. "Brittle Behavior of Polymeric Solids" in Fracture Processes in Polymeric Solids, B. Rosen, ed., Wiley & Sons, 215, 196 (1964).

27. Joy, D. C., Lecture Notes on Specimen Charging from ZOO 511, 1-2n (1996).

28. Wolock, I. and S. B. Newman. "Fracture Topography" in Fracture Behavior in Polymeric Solids, B. Rosen, ed.,Wiley & Sons, 241 (1964).

APPENDIX

APPENDIX

A-1. Creep C-Scan Ultrasonic Data:

Table A-1. C-Scan Data for P21-0-3 (Air, 50% RH)

Image No.	Pre-Test MG	Post-Test MG	Pre-Test Std. Dev.	Post-Test Std. Dev.	Pre-Test CV, %	Post-Test CV, %
1*	47.88	45.50	13.80	17.13	28.82	37.65
2	48.21	44.75	10.65	10.68	22.09	23.87
3	68.39	55.45	13.72	12.85	20.06	23.17
4	71.78	64.94	18.47	12.83	25.73	19.76
5	83.68	80.68	10.74	12.55	12.83	15.56
6	93.14	86.31	13.44	17.89	14.43	20.73
7	105.50	83.72	13.84	11.02	13.12	13.16
8	104.63	86.62	20.22	12.79	19.33	14.77

* No fracture.

Table A-2. C-Scan Data for P21-0-27 (Air, 50% RH)

Image No.	Pre-Test MG	Post-Test MG	Pre-Test Std. Dev.	Post-Test Std. Dev.	Pre-Test CV, %	Post-Test CV, %
1*	179.26	122.23	25.17	29.71	14.04	24.31
2	191.14	132.63	24.98	19.73	13.07	14.88
3	209.57	161.13	14.75	17.25	7.04	10.71
4	197.36	148.38	32.44	34.58	16.44	23.31
5	206.33	156.35	14.48	17.90	7.02	11.45
6	190.65	149.90	20.77	19.30	10.89	12.88
7	207.94	160.71	24.30	23.49	11.69	14.62
8	197.64	148.17	20.08	16.50	10.16	11.14

* No fracture.

Table A-3. C-Scan Data for P21-0-5 (Distilled Water)

Image No.	Pre-Test MG	Post-Test MG	Pre-Test Std. Dev.	Post-Test Std. Dev.	Pre-Test CV, %	Post-Test CV, %
1*	53.98	48.74	12.41	14.19	22.99	29.11
2	85.59	69.86	12.60	11.84	14.72	16.95
3	93.15	73.37	13.63	10.19	14.63	13.89
4	79.13	63.53	14.94	10.28	18.88	16.18
5	85.47	72.43	14.39	11.56	16.84	15.96
6	110.62	86.32	16.36	17.44	14.79	20.20
7	114.18	15.25	22.64	11.93	19.83	15.41
8	104.77	72.46	15.25	10.40	14.56	14.35

* Post-test image taken near fracture.

Table A-4. C-Scan Data for P21-0-10 (Distilled Water)

Image No.	Pre-Test MG	Post-Test MG	Pre-Test Std. Dev.	Post-Test Std. Dev.	Pre-Test CV, %	Post-Test CV, %
1*	84.89	73.66	15.83	19.18	18.65	26.04
2	93.26	78.11	14.60	10.97	15.66	14.04
3	114.54	96.93	14.67	14.32	12.81	14.77
4	121.90	119.07	25.62	25.38	21.02	21.32
5	118.76	102.25	24.78	24.13	20.87	23.60
6	138.64	118.43	26.57	22.54	19.16	19.03
7	132.04	103.40	21.56	18.04	16.33	17.45
8	131.73	110.52	16.62	17.29	12.62	15.64

* Post-test image taken near fracture.

Table A-5. C-Scan Data for P21-0-22 (Distilled Water)

Image No.	Pre-Test MG	Post-Test MG	Pre-Test Std. Dev.	Post-Test Std. Dev.	Pre-Test CV, %	Post-Test CV, %
1	86.89	71.04	14.32	15.29	16.48	21.52
2	98.38	82.57	23.54	17.58	23.93	21.29
3	80.92	63.15	11.39	14.00	14.08	22.17
4*	90.18	61.41	17.92	22.17	19.87	36.10
5	88.89	74.23	13.36	11.78	15.03	15.87
6	83.25	64.92	16.63	13.76	19.98	21.20
7	66.74	58.05	16.10	16.55	24.12	28.51
8	90.00	84.13	19.88	18.06	22.09	21.47

* Post-test image taken near fracture.

Table A-6. C-Scan Data for P21-0-7 (Windshield Washer Fluid)

Image No.	Pre-Test MG	Post-Test MG	Pre-Test Std. Dev.	Post-Test Std. Dev.	Pre-Test CV, %	Post-Test CV, %
1	78.02	61.50	17.93	13.63	22.98	22.16
2*	70.59	68.47	12.04	18.87	17.06	27.56
3	92.32	73.78	21.46	16.90	23.25	22.91
4	107.95	72.42	13.87	11.32	12.85	15.63
5	108.74	72.15	19.07	13.30	17.54	18.43
6	95.98	53.59	12.11	13.15	12.62	24.53
7	129.69	73.34	17.07	12.39	13.16	16.89
8	140.10	82.84	22.48	20.48	16.05	24.72

* Post-test image taken near fracture.

Table A-7. C-Scan Data for P21-0-8 (Windshield Washer Fluid)

Image No.	Pre-Test MG	Post-Test MG	Pre-Test Std. Dev.	Post-Test Std. Dev.	Pre-Test CV, %	Post-Test CV, %
1	99.54	87.36	18.77	19.41	18.86	22.22
2*	114.84	65.93	13.68	23.19	11.91	35.17
3	105.13	72.80	16.06	17.96	15.28	24.67
4	100.37	72.28	18.15	11.49	18.08	15.90
5	106.77	83.22	15.26	14.89	14.29	17.89
6	144.65	99.69	30.63	22.96	21.18	23.03
7	129.74	97.68	23.15	20.29	17.84	20.77
8	146.16	96.02	18.05	14.58	12.35	15.18

* Post-test image taken near fracture.

Table A-8. C-Scan Data for P21-0-9 (Windshield Washer Fluid)

Image No.	Pre-Test MG	Post-Test MG	Pre-Test Std. Dev.	Post-Test Std. Dev.	Pre-Test CV, %	Post-Test CV, %
1*	89.81	71.90	18.22	12.78	20.29	17.77
2	99.03	67.46	15.26	13.31	15.41	19.73
3	96.69	73.77	18.12	14.28	18.74	19.36
4	104.84	86.27	16.89	12.69	16.11	14.71
5	133.57	96.90	23.35	13.25	17.48	13.67
6	143.42	95.30	29.96	18.28	20.89	19.18
7	110.91	80.96	20.13	15.32	18.14	18.92
8	134.45	87.20	26.08	16.20	19.40	18.58

* Post-test image taken near fracture.

A-2. Fatigue C-Scan Ultrasonic Data:

Table A-9. C-Scan Data for P21-0-11 (Air, 50% RH)

Image No.	Pre-Test MG	Post-Test MG	Pre-Test Std. Dev.	Post-Test Std. Dev.	Pre-Test CV, %	Post-Test CV, %
1	90.25	81.58	7.83	12.26	8.68	15.03
2	77.91	71.87	10.95	11.77	14.05	16.38
3	83.57	69.23	10.52	10.95	12.59	15.82
4	92.79	84.30	8.75	9.02	9.43	10.70
5*	107.30	79.54	15.75	33.06	14.68	41.56
6	140.66	94.40	28.90	24.34	20.55	25.78
7	113.34	88.92	18.95	13.28	16.72	14.93
8	113.10	81.02	28.23	17.65	24.96	21.78

* Post-test image taken near fracture.

Table A-10. C-Scan Data for P21-0-12 (Air, 50% RH)

Image No.	Pre-Test MG	Post-Test MG	Pre-Test Std. Dev.	Post-Test Std. Dev.	Pre-Test CV, %	Post-Test CV, %
1	75.40	69.66	11.99	10.53	15.90	15.12
2	72.75	63.61	15.11	15.31	20.77	24.07
3	76.95	64.21	15.32	10.91	19.91	16.99
4	68.94	59.76	14.78	10.78	21.44	18.04
5*	94.87	76.45	18.22	22.77	19.21	29.78
6	120.02	82.96	19.20	13.21	16.00	15.92
7	101.37	82.34	18.89	16.19	18.63	19.66
8	131.89	97.45	20.32	14.61	15.41	14.99

* Post-test image taken near fracture.

Table A-11. C-Scan Data for P21-0-21 (Air, 50% RH)

Image No.	Pre-Test MG	Post-Test MG	Pre-Test Std. Dev.	Post-Test Std. Dev.	Pre-Test CV, %	Post-Test CV, %
1	49.44	35.46	20.10	11.74	40.66	33.12
2	59.95	53.24	14.66	12.88	24.45	24.19
3	62.28	57.50	14.55	12.56	23.36	21.84
4	62.02	56.00	16.57	19.35	26.72	34.55
5	53.56	45.48	14.85	11.85	27.73	26.06
6*	57.00	58.09	15.40	41.98	27.02	72.27
7	51.20	49.71	13.91	19.44	27.17	39.11
8	64.25	44.75	16.00	12.53	24.90	28.00

* Post-test image taken near fracture.

Table A-12. C-Scan Data for P21-0-19 (Distilled Water)

Image No.	Pre-Test MG	Post-Test MG	Pre-Test Std. Dev.	Post-Test Std. Dev.	Pre-Test CV, %	Post-Test CV, %
1	99.02	85.04	16.00	13.97	16.16	16.43
2	82.82	76.77	13.27	13.94	16.02	18.16
3	109.34	105.47	23.76	22.41	21.73	21.25
4	80.61	74.34	12.06	12.25	14.96	16.48
5*	105.46	62.42	37.17	11.80	19.45	57.70
6	100.95	62.74	21.31	17.34	33.97	16.36
7	106.01	89.29	17.34	14.94	16.36	16.73
8	79.64	66.20	14.81	13.08	18.60	19.76

* Post-test image taken near fracture.

Table A-13. C-Scan Data for P21-0-25 (Distilled Water)

Image No.	Pre-Test MG	Post-Test MG	Pre-Test Std. Dev.	Post-Test Std. Dev.	Pre-Test CV, %	Post-Test CV, %
1	157.25	116.60	25.27	16.13	16.07	13.83
2	144.40	103.22	28.46	19.07	19.71	18.48
3	157.14	118.08	33.64	19.69	21.41	16.68
4	118.51	86.96	27.64	21.84	23.32	25.11
5	154.58	115.50	19.68	16.09	12.73	13.93
6	152.22	106.16	26.12	17.61	17.16	16.59
7*	176.14	93.57	24.19	35.45	13.73	37.89
8	180.16	140.59	28.66	17.92	15.91	12.75

* Post-test image taken near fracture.

Table A-14. C-Scan Data for P21-0-26 (Distilled Water)

Image No.	Pre-Test MG	Post-Test MG	Pre-Test Std. Dev.	Post-Test Std. Dev.	Pre-Test CV, %	Post-Test CV, %
1	207.18	165.47	23.06	22.36	11.13	13.51
2	210.83	162.93	23.12	18.31	10.97	11.24
3	201.38	157.01	23.97	23.10	11.90	14.71
4	199.56	155.62	29.22	26.58	14.64	17.08
5*	196.91	52.05	17.57	19.73	8.92	37.91
6	196.85	128.17	19.65	20.08	10.03	15.67
7	196.55	142.58	20.85	19.27	10.61	13.52
8	198.80	165.34	30.51	23.19	15.35	14.03

* Post-test image taken near fracture.

Table A-15. C-Scan Data for P21-0-16 (Windshield Washer Fluid)

Image No.	Pre-Test MG	Post-Test MG	Pre-Test Std. Dev.	Post-Test Std. Dev.	Pre-Test CV, %	Post-Test CV, %
1	86.36	74.85	13.15	21.04	15.23	28.11
2	101.59	75.68	18.67	10.80	18.38	14.27
3	92.61	78.16	19.97	12.80	21.56	16.38
4	116.67	96.13	19.18	33.88	16.44	35.24
5*	87.66	34.61	18.63	19.01	21.25	54.93
6	102.39	77.73	19.65	21.74	19.19	27.97
7	109.10	87.21	15.21	15.63	13.94	17.92
8	118.38	99.91	22.76	21.58	19.23	21.60

* Post-test image taken near fracture.

Table A-16. C-Scan Data for P21-0-17 (Windshield Washer Fluid)

Image No.	Pre-Test MG	Post-Test MG	Pre-Test Std. Dev.	Post-Test Std. Dev.	Pre-Test CV, %	Post-Test CV, %
1	86.71	58.43	18.21	19.23	21.00	32.91
2	90.84	62.00	16.10	16.17	17.72	26.08
3	100.90	118.21	12.53	24.15	12.42	20.43
4	110.13	132.30	12.61	16.65	11.45	12.59
5	97.04	119.92	12.36	29.08	12.74	24.25
6	115.39	111.55	16.26	22.01	14.09	19.73
7*	121.24	48.14	30.38	28.37	25.06	58.93
8	105.85	85.30	15.39	20.71	14.54	24.28

* Post-test image taken near fracture.

Table A-17. C-Scan Data for P21-0-18 (Windshield Washer Fluid)

Image No.	Pre-Test MG	Post-Test MG	Pre-Test Std. Dev.	Post-Test Std. Dev.	Pre-Test CV, %	Post-Test CV, %
1	70.31	59.89	12.81	9.89	18.22	16.51
2	95.52	84.27	11.32	13.75	11.85	16.32
3	70.57	55.45	11.30	10.52	16.01	18.97
4	113.55	97.85	12.08	11.71	10.64	11.97
5	95.30	78.88	15.80	7.93	16.58	10.05
6*	122.32	65.58	12.15	25.40	9.93	38.73
7	111.51	97.80	23.72	15.44	21.27	15.79
8	105.61	92.02	15.37	15.19	14.55	16.51

* Post-test image taken near fracture.

A-3. Creep LTM Data:

Table A-18. LTM Data for P21-0-3 (Air, 50% RH)

Image No.	Pre-Test MG	Post-Test MG	Pre-Test Std. Dev.	Post-Test Std. Dev.	Pre-Test CV, %	Post-Test CV, %
1	97.85	105.54	39.80	41.67	40.67	39.48
4	128.10	149.44	33.12	32.15	25.85	21.51
7	124.08	139.99	36.77	36.12	29.63	25.80
10	101.64	121.45	21.50	20.74	21.15	17.08
13	104.27	118.10	25.78	25.20	24.72	21.34
16	108.30	121.03	24.08	23.34	22.23	19.28
18*	87.97	99.82	18.66	22.13	21.21	22.17

* No fracture.

Table A-19. LTM Data for P21-0-27 (Air, 50% RH)

Image No.	Pre-Test MG	Post-Test MG	Pre-Test Std. Dev.	Post-Test Std. Dev.	Pre-Test CV, %	Post-Test CV, %
1	179.60	178.72	53.46	49.20	29.77	27.53
4	203.68	198.61	36.06	31.86	17.70	16.04
7	208.73	209.18	43.80	35.87	20.98	17.15
10	177.42	175.79	38.84	31.86	33.08	18.12
13	198.87	201.14	42.41	32.50	21.33	16.16
16	188.96	195.51	39.50	34.37	20.90	17.58
18*	210.49	214.47	34.12	30.68	16.21	14.31

* No fracture.

Table A-20. LTM Data for P21-0-5 (Distilled Water)

Image No.	Pre-Test MG	Post-Test MG	Pre-Test Std. Dev.	Post-Test Std. Dev.	Pre-Test CV, %	Post-Test CV, %
1	129.82	114.92	48.47	43.94	37.64	38.24
4	144.60	122.01	31.56	23.87	21.83	19.56
7	126.51	117.17	31.80	26.29	25.14	22.44
10	132.35	123.52	29.45	20.96	22.25	16.97
13	127.79	122.31	24.14	27.47	18.89	22.46
16	119.94	116.74	26.23	22.59	21.87	19.35
18*	121.10	117.98	25.61	25.67	21.15	21.76

* Fractured 9.8 cm from Reference Point.

Table A-21. LTM Data for P21-0-10 (Distilled Water)

Image No.	Pre-Test MG	Post-Test MG	Pre-Test Std. Dev.	Post-Test Std. Dev.	Pre-Test CV, %	Post-Test CV, %
1	106.59	99.22	39.55	37.25	37.10	37.54
4	162.36	147.11	34.10	24.74	21.00	16.82
7	169.55	158.81	42.51	37.01	25.07	23.30
10	153.08	140.57	35.54	30.17	23.30	23.22
13	180.19	157.83	46.64	37.12	25.88	23.52
16	160.74	148.20	34.32	26.89	21.35	18.14
18*	147.26	132.14	35.48	26.38	24.09	19.96

* Fractured 10.1 cm from Reference Point.

Table A-22. LTM Data for P21-0-22 (Distilled Water)

Image No.	Pre-Test MG	Post-Test MG	Pre-Test Std. Dev.	Post-Test Std. Dev.	Pre-Test CV, %	Post-Test CV, %
1	93.75	91.10	28.49	26.35	30.39	28.92
4	115.51	102.37	24.36	22.81	21.09	22.28
7	102.23	97.27	22.53	19.14	22.04	19.68
10	107.04	98.25	21.54	18.52	20.12	18.85
13	92.88	90.39	15.90	17.69	17.12	19.57
16	92.25	89.57	21.02	21.56	22.79	24.07
18*	91.55	85.77	16.07	15.20	17.55	17.72

* Fractured 5.0 cm from Reference Point.

Table A-23. LTM Data for P21-0-7 (Windshield Washer Fluid)

Image No.	Pre-Test MG	Post-Test MG	Pre-Test Std. Dev.	Post-Test Std. Dev.	Pre-Test CV, %	Post-Test CV, %
1	122.01	104.24	56.02	49.67	45.91	47.65
4	153.13	109.78	40.38	28.53	26.37	25.99
7	157.88	124.07	37.34	31.30	23.65	25.23
10	129.83	105.63	32.76	29.87	25.23	28.28
13	163.08	128.81	40.68	36.58	24.94	28.40
16	134.15	105.90	33.01	25.78	24.61	24.34
18*	113.69	87.43	25.80	18.60	22.69	21.27

* Fractured 10.8 cm from Reference Point.

Table A-24. LTM Data for P21-0-8 (Windshield Washer Fluid)

Image No.	Pre-Test MG	Post-Test MG	Pre-Test Std. Dev.	Post-Test Std. Dev.	Pre-Test CV, %	Post-Test CV, %
1	119.41	130.14	54.77	25.76	45.87	19.79
4	189.35	167.76	50.63	50.28	26.74	29.97
7	163.97	149.52	44.94	35.53	27.41	23.76
10	168.25	142.02	39.78	31.16	23.64	21.94
13	146.16	129.03	38.31	32.31	26.21	25.04
16	146.58	132.09	37.87	29.06	25.84	22.00
18*	135.98	123.11	33.52	24.64	24.65	20.01

* Fractured 7.7 cm from Reference Point.

Table A-25. LTM Data for P21-0-9 (Windshield Washer Fluid)

Image No.	Pre-Test MG	Post-Test MG	Pre-Test Std. Dev.	Post-Test Std. Dev.	Pre-Test CV, %	Post-Test CV, %
1*	171.32	177.94	67.39	54.16	39.34	30.44
4	180.66	167.45	44.32	40.02	24.53	23.90
7	171.87	165.54	38.58	35.66	22.45	21.54
10	161.94	147.98	41.08	34.55	25.37	23.35
13	174.06	155.53	49.81	43.84	28.62	28.19
16	164.41	160.41	42.11	41.98	25.61	26.17
18	143.38	148.37	34.86	27.85	24.31	18.77

* Fractured 0.8 cm from Reference Point in the tab.

A-4. Fatigue LTM Data:

Table A-26. LTM Data for P21-0-11 (Air, 50% RH)

Image No.	Pre-Test MG	Post-Test MG	Pre-Test Std. Dev.	Post-Test Std. Dev.	Pre-Test CV, %	Post-Test CV, %
1	151.68	132.17	38.92	33.65	25.66	25.46
4	180.61	184.09	42.20	35.70	23.37	19.39
7	182.42	180.12	42.14	36.62	23.10	20.33
10	195.76	181.69	44.47	37.07	22.72	20.40
13	172.82	172.29	45.57	34.56	26.37	20.06
16	166.79	155.93	36.56	33.87	21.92	21.72
18*	162.15	148.33	35.75	26.54	22.05	17.89

* Fractured 3.6 cm from Reference Point.

Table A-27. LTM Data for P21-0-12 (Air, 50% RH)

Image No.	Pre-Test MG	Post-Test MG	Pre-Test Std. Dev.	Post-Test Std. Dev.	Pre-Test CV, %	Post-Test CV, %
1	170.36	172.56	51.46	40.71	30.21	23.59
4	193.55	196.18	41.91	35.89	21.65	18.29
7	187.39	188.24	45.21	38.15	24.13	20.27
10	167.82	176.56	40.04	33.23	23.86	18.82
13	197.55	183.16	41.60	30.98	21.06	16.91
16	186.35	194.64	38.78	33.45	20.81	17.19
17	175.94	170.51	40.55	36.17	23.05	21.21
18*	153.27	101.13	36.20	27.68	23.62	27.37

* Fractured 3.5 cm from Reference Point.

Table A-28. LTM Data for P21-0-21 (Air, 50% RH)

Image No.	Pre-Test MG	Post-Test MG	Pre-Test Std. Dev.	Post-Test Std. Dev.	Pre-Test CV, %	Post-Test CV, %
1	77.86	89.36	26.37	27.91	33.87	31.23
4	98.22	112.48	26.95	24.61	27.44	21.88
7	76.58	86.67	17.35	16.04	22.66	18.51
10	74.42	87.47	16.47	15.13	22.13	17.30
13	71.14	86.71	17.24	14.89	24.23	17.17
15	82.46	88.83	17.14	17.27	20.79	19.44
16*	64.33	158.93	14.22	55.02	22.10	34.62

* Fractured 3.2 cm from Reference Point.

Table A-29. LTM Data for P21-0-19 (Distilled Water)

Image No.	Pre-Test MG	Post-Test MG	Pre-Test Std. Dev.	Post-Test Std. Dev.	Pre-Test CV, %	Post-Test CV, %
1	106.55	125.97	34.72	35.73	32.59	28.36
4	135.33	147.95	41.55	40.60	30.70	27.44
7	133.26	95.48	31.98	25.18	24.00	26.37
10	122.96	146.23	30.73	34.93	24.99	23.89
13	108.78	143.89	22.18	29.68	20.39	20.63
16	118.96	147.76	29.16	36.04	24.51	24.39
17	116.22	130.01	24.97	30.40	21.49	23.38
18*	113.57	161.14	25.08	42.83	22.08	26.58

* Fractured 4.1 cm from Reference Point.

Table A-30. LTM Data for P21-0-25 (Distilled Water)

Image No.	Pre-Test MG	Post-Test MG	Pre-Test Std. Dev.	Post-Test Std. Dev.	Pre-Test CV, %	Post-Test CV, %
1	131.29	148.02	54.46	51.23	41.48	34.61
4	160.69	128.04	41.09	40.89	25.57	31.94
7	140.85	162.34	30.43	39.77	21.60	24.50
8*	147.25	134.75	41.91	46.47	28.46	34.49

* Fractured 1.4 cm from Reference Point.

Table A-31. LTM Data for P21-0-26 (Distilled Water)

Image No.	Pre-Test MG	Post-Test MG	Pre-Test Std. Dev.	Post-Test Std. Dev.	Pre-Test CV, %	Post-Test CV, %
1	162.78	168.00	47.81	44.37	29.37	26.41
4	178.00	181.30	43.99	45.01	24.71	24.83
7	179.08	185.89	38.24	34.93	21.35	18.79
10	166.43	153.89	37.54	31.56	22.56	20.51
13	179.60	150.76	43.47	46.05	24.20	30.55
16	178.72	165.52	33.84	33.79	18.93	20.41
18*	176.96	171.47	39.23	39.88	22.17	23.26

* Fractured 4.2 cm from Reference Point.

Table A-32. LTM Data for P21-0-16 (Windshield Washer Fluid)

Image No.	Pre-Test MG	Post-Test MG	Pre-Test Std. Dev.	Post-Test Std. Dev.	Pre-Test CV, %	Post-Test CV, %
1	124.08	79.83	41.60	18.83	33.37	23.59
4	178.08	108.87	53.35	27.43	29.96	25.20
7	154.95	100.45	42.10	19.36	27.17	19.27
10	140.91	88.46	41.28	19.84	29.30	22.43
13	107.92	70.29	21.62	12.57	20.03	17.88
16	132.06	119.32	38.08	28.20	28.84	23.63
18*	130.91	98.22	27.34	19.95	20.88	20.31

* Fractured 4.1 cm from Reference Point.

Table A-33. LTM Data for P21-0-17 (Windshield Washer Fluid)

Image No.	Pre-Test MG	Post-Test MG	Pre-Test Std. Dev.	Post-Test Std. Dev.	Pre-Test CV, %	Post-Test CV, %
1	145.79	116.56	49.63	42.04	34.04	36.07
4	117.76	104.05	32.83	17.25	27.88	16.58
7	147.26	131.32	43.99	34.04	29.87	25.52
8	145.94	116.84	35.20	23.49	24.12	20.10
9*	133.09	141.76	34.95	39.07	26.26	27.56

* Fractured 1.7 cm from Reference Point.

Table A-34. LTM Data for P21-0-18 (Windshield Washer Fluid)

Image No.	Pre-Test MG	Post-Test MG	Pre-Test Std. Dev.	Post-Test Std. Dev.	Pre-Test CV, %	Post-Test CV, %
1	159.65	161.27	52.00	53.45	32.57	33.14
4	119.47	131.11	26.32	22.70	22.03	17.31
7	147.42	155.02	38.46	34.74	26.09	22.41
10	132.39	136.41	36.94	27.15	27.90	19.90
12	140.57	118.32	30.37	29.41	21.60	24.86
13*	139.11	139.86	33.47	48.01	24.06	34.33

* Fractured 2.4 cm from Reference Point.

VITA

Helen M. Herring was born in Hampton, Virginia on March 22, 1965. She attended several schools throughout the southeast United States before graduating from high school at Bob Jones High in Madison, Alabama in 1983. She received a Bachelor of Science degree in Physics in 1988 and a Bachelor of Science degree in Nondestructive Testing Technology in 1989 both from Athens State College, Athens, Alabama. During her undergraduate years, she worked for Trimet, Inc., a consulting engineering firm, as a laboratory technician. After receiving her undergraduate degrees, she held a materials engineering research position with Boeing Defense and Space Group on the International Space Station Project, working specifically on the multi-layer insulation blankets for the space station. Additionally, she worked as a laboratory research assistant for AC Engineering in direct cooperation with NASA/Marshall Space Flight Center on an environmental evaluation and control project for manned space flight systems. She continued her higher education at the University of Tennessee in Knoxville, where she will receive her Master of Science degree in Polymer Engineering in December 1997.

Ms. Herring will be pursuing her Doctor of Philosophy degree in Materials Engineering Science at Virginia Polytechnic Institute and State University in Blacksburg, Virginia, beginning in the Fall of 1997.